Little Buoys, Big Ocean: Observations of Wave-Driven Transport of Buoyant Objects in the Nearshore and Marginal Ice Zone

EJ Rainville

A dissertation
submitted in partial fulfillment of the
requirements for the degree of

Doctor of Philosophy

University of Washington

2025

Reading Committee:

Jim Thomson, Chair

Melissa Moulton, Chair

Morteza Derakhti

Christie Hegermiller

Spicer Bak

Kate Brodie

Program Authorized to Offer Degree:
Civil and Environmental Engineering

University of Washington

Abstract

Little Buoys, Big Ocean: Observations of Wave-Driven Transport of Buoyant Objects in the Nearshore and Marginal Ice Zone

EJ Rainville

Co-Chairs of the Supervisory Committee:
Jim Thomson
Civil and Environmental Engineering

Melissa Moulton
Civil and Environmental Engineering

A variety of objects drift on the ocean surface, including plastics, sea ice, search and rescue targets, oil, and marine organisms. Accurately predicting their trajectories is essential for both scientific and operational applications. The processes that drive the transport of these objects, particularly on shorter time and space scales, are not fully understood. This work addresses this problem, particularly investigating the wave-driven transport mechanisms in the nearshore and marginal ice zone. These regions are dynamically complex, and wave transformation is a dominant feature of both regions. This work primarily uses in situ observations to investigate buoyant object transport. The observations are from two large field experiments: the US Coastal Research Program funded During Nearshore Events Experiment (DUNEX) and NASA's Salinity and Stratification at the Sea Ice Edge (SASSIE) campaign. The following work consists of the development and nearshore deployments of a small-scale free-drifting wave buoys called microSWIFTS, observations of surfing transport from the microSWIFTs, and observations of transport driven by wind and waves in the Arctic marginal ice zone.

The microSWIFT is a small buoy equipped with a GPS module to measure the buoy's position and horizontal velocities and an Inertial Measurement Unit (IMU) to directly measure the buoy's rotation rates, accelerations, and magnetic heading. Measurements were collected over a 27-day field experiment (DUNEX) in October 2021 at the US Army Corps of Engineers Field Research Facility in Duck, NC. The microSWIFTs were deployed as a series of coherent arrays, meaning they all sampled simultaneously with a common time reference, leading to a rich spatial and temporal dataset during each deployment. Measurements spanned offshore significant wave heights ranging from 0.5 to 3 meters and peak wave periods ranging from 5 to 15 seconds over the entire experiment.

Observations of surfing transport are made using the data collected from the microSWIFTs as part of DUNEX. Surfing events are observed in the drift trajectories of the buoys as 'jumps' in the time series of cross-shore position. There are 3,172 surfing events observed, with a median jump amplitude of 8.3 meters and a median duration of 2.5 seconds. The buoy's trajectories are simulated using three models of increasing physics complexity: 'Wind-Only," 'Wind and Waves," and 'Wind, Waves, and Surfing." The surfing process is represented using a probabilistic parameterization. The accuracy of the simulations is significantly improved when surfing is included.

Sea ice in the marginal ice zone is generally considered to be in "free-drift" and acts like a drifter following the wind, waves, and currents. The marginal ice zone is the dynamic region of sea ice between 15% - 80% sea ice area coverage. A dominant feature of the marginal ice zone is the attenuation of waves propagating from the open ocean, making this region analogous to the surf zone. SWIFT drifters were deployed in the marginal ice zone, and their drift speeds were measured. A combination of wave radiation stress gradient-driven currents, direct windage on the drifters, and Ekman transport accounts for their observed drift speeds. These results suggest that wave-driven transport mechanisms cause a significant portion of the observed drift at the outer edges of the ice pack. Wave-driven transport in the marginal ice zone may play an important role in shaping the future evolution of the sea ice edge, as earlier melting and later refreezing allow larger waves to interact with the ice edge.

TABLE OF CONTENTS

LIST OF FIGURES

LIST OF TABLES

ACKNOWLEDGMENTS

Thoughts and Thank Yous

What a ride! These past five years have been the most fun and intellectually challenging that I have experienced yet. I have learned that, like life, a Ph.D. is a team sport. I am so thankful for the team that I have had along the way. I couldn't have asked for better advisors, colleagues, friends, and family.

Jim, thank you for all that you have done to help me through this process. I wouldn't be here today without you. I have learned so much from you and improved as an engineer, scientist, writer, and person. As you know, one of my favorite questions has been "what is your life philosophy?" and you answered with "do the work." This is one of the most fitting answers I have gotten yet. A Ph.D. is very much an endurance event, and it took me a long time to learn (and still learning) to just show up each day and do the work. Some days go easier than others, but regardless, you show up and get after it. In addition, I learned lots of other crucial lessons from your common phrases. "One is none," "credit is a renewable resource," "the best rescue is a self rescue," "nothing parties like a rental," "never park a university vehicle in front of a liquor store," amongst many others. Jokes aside, I am beyond fortunate to have learned so much from such a good mentor and friend. Thank you for always being in my corner and helping me to grow and improve.

Melissa, thank you for always being the voice of excitement and always bringing a new perspective. You once told me your life philosophy was "keep it weird." I love this one. I have seen this in the new and interesting perspectives you can bring to a conversation, which is an amazing skill and has led to the dissertation you see here today. Shortly after the DUNEX experiment, we worked on determining individual wave heights directly from the microSWIFT measurements. This wasn't working very well, and one of the main reasons was that the drifters would start to surf. For a long time, I focused on trying to filter this "noise" out of the dataset until you suggested that maybe that noise is a signal we could be interested in instead. That shift in perspective led to this dissertation and made me realize how important looking at a problem a certain way is. Thank you for all the help along the way, the fun conversations, the times that you have helped me understand more, the visits to Colorado, and so much more.

Morteza, thank you for always bringing great questions. Very often, we would think of a topic and decide on an explanation for a certain problem to which you would ask "why?" This would usually cause us to dig deeper, leading to a much better understanding of the given problem. Thank you for all your guidance and enthusiasm along the way.

Thank you very much to the rest of my committee members, Christie, Spicer, Kate, Michelle, and Chris. I appreciate your support and encouragement. Thank you to Alex de Klerk and Joe Talbert for their technical support and fun conversations during Monday meetings and field work.

Thank you to Jake Davis for spending countless hours in the Puddle (an endearing name for our shared office), talking science with me. You made this process extremely fun, and I am glad to have a great friend like you. An additional thank you to the larger Environmental Fluid Mechanics group and all the lovely members.

A huge thank you to my family for all their support. I couldn't have done it without you all. I appreciate all the questions and words of encouragement—they really helped.

Finally, a special thank you to my fiancée Anna. The amount you have heard me talk about drifting objects and the number of times I have asked you to check out my new graph is outrageous. But you are always psyched to, and I am beyond thankful for you. I am certain you know more about this material at this point than I do. Thank you for all the support. Love you.

This is by no means an exhaustive list of all the people to thank; there are many others.

There would be no dissertation without money. The US Coastal Research Program and the National Aeronautics and Space Administration supported this work, making it possible. I am very thankful for their financial support to make this happen.

Preparing this dissertation has given me a good perspective on the bigger picture of the state-of-the-art of oceanic drift, and given me a chance to look out over the field. I like to think of this feeling with the analogy of the "Eye of Sauron days". Somedays, you get to be the Eye of Sauron at the top of Barad-dûr, looking out over the field and understanding where your work fits in the bigger picture. Other days, you're just an orc slashing through integrals and debugging code with no vision of the bigger picture. On other days, you are Frodo and Sam making their way to Mordor, one step at a time. The aggregation of these effects makes this a very special process. While this is a silly analogy, it is fun and it is good to make meaning out of the magic of the mundane [*Arthur*, 2023]. I am thankful for the process.

Chapter 1

INTRODUCTION

1.1 Background and Motivation

1.1.1 Short-Term Forecasting of Drifting Objects

Many objects drifting on the surface of the ocean are of interest to understand where they will go. These objects include plastics, sea ice, search and rescue targets, oil, and organisms. It is important to understand where ocean-bound plastics will be transported to launch pollution mitigation efforts effectively to reduce plastic pollution and clean existing ocean-bound plastic [*Van Sebille et al.*, 2020]. It is also important to understand where sea ice will be moving to understand how the ecosystem will be affected [*Post et al.*, 2013] and how shipping lanes will change in the future [*Ho*, 2010]. Short-term (O(hours-days)) high-resolution forecasts need to be accurate for search and rescue operations, where incorrect predictions can lead to fatalities [*Breivik et al.*, 2013]. Organisms such as Sargassum are transported across the oceans, washing up on beaches across the Caribbean, West Africa, China, etc., where they can cause direct impacts on ecosystems and economies [*Van Tussenbroek et al.*, 2017; *Olguin-Maciel et al.*, 2022; *Smetacek and Zingone*, 2013]. Each object will obey similar physical laws and move with a combination of the ocean's wind, waves, and currents.

Producing an accurate long-term forecast of drift in the ocean may be paradoxically less challenging than making a short-term forecast [*Christensen et al.*, 2018]. This comment is about drift due to inertial oscillations (discussed in more detail in Chapter 5), which for short drift time scales have large amplitudes and make short-term predictions challenging, while in long-range forecasts can be averaged out. Long-range forecasts can be beneficial but less helpful in an operational forecasting context [*Schiller et al.*, 2018]. Operational forecasts may be used in search-and-rescue operations, oil spill cleanup, plastic spill cleanup, and ice in shipping lanes. Recent review articles have called for an improved understanding of the effects of waves on drifting objects [*Christensen et al.*, 2018; *Dumont*, 2022] and to investigate smaller-scale regions with higher resolution models to better understand how local processes can affect the transport of objects [*NOAA*, 2016].

The same dynamics govern transport on the ocean's surface regardless of the object. Transport will be defined here as the movement of drifting objects by their environment. A combination of currents, wind, and wave-driven transport drives the transport of buoyant objects in the ocean.

1.2 Theoretical Framework

1.2.1 Forces on Floating Objects

Objects floating on the ocean's surface move with a combination of the winds, currents, and waves. Observations and colloquial knowledge suggest that most floating objects in the ocean drift at approximately 2% - 4% of the wind speed relative to the water speed [*Wagner et al.*, 2022]. A recent study by *Wagner et al.* [2022] suggests a framework to explain this wind drift percentage based on a simplified momentum balance on a floating object. A schematic of the forces on the drifting object is shown in Figure 1.1. The momentum balance on the object simplifies to a balance between the skin and form drag on both the air and water sides of the object. The simplified, one-dimensional momentum balance from this analysis is the following,

$$m\frac{dv}{dt} = F_w + F_a + \mathcal{F} \tag{1.1}$$

Here, the subscript w stands for water, the subscript a stands for air, and $\mathcal{F}$ is any other force acting on the floating object. *Wagner et al.* [2022] then makes the following assumptions:

- Steady Drift, i.e. $m\frac{dv}{dt} = 0$

- Neglect other forces on the drifting object, i.e. $\mathcal{F} = 0$
- Drag forces on the floating object can be modeled as quadratic drag laws, i.e.

  $F_w = \frac{1}{2}(C_w^F A_w^V + C_w^S A_w^H)\rho_w(v_w - v)^2$ and $F_a = \frac{1}{2}(C_a^F A_a^V + C_a^S A_a^H)\rho_a(v_a - v)^2$
- The wind speed is much greater than the speed of the drifting object, i.e, $v_a >> v$
- The wind speed is much greater than the speed of the water, i.e. $v_a >> v_w$

Using these assumptions and solving for the object's speed, the one-dimensional momentum balance becomes equation 1.2.

$$\vec{v} = \vec{v}_w + \epsilon\vec{v}_a \tag{1.2}$$

$$\epsilon = \sqrt{\frac{\rho_a}{\rho_w}}\sqrt{\frac{bC_a^F + lC_a^S}{dC_w^F + lC_w^S}} \tag{1.3}$$

The parameter ϵ (Equation 2.1) is the wind sensitivity and typically has values between 2% and 5%. Here, the parameters C_a^F and C_w^F are form drag coefficients in the air and water, the parameters C_a^S and C_w^S are the skin drag coefficients in air and water, and the parameters b, l, d are geometric parameters fully described in *Wagner et al.* [2022]. This analysis will act as a simple model that will be further investigated and modified to better describe the transport of drifting objects under additional dynamics. The main takeaway from this analysis is that drifting objects move primarily with the currents (mean currents and Stokes drift) and a small percentage of the wind, which agrees with the typical assumption for modeling drift trajectories [*Christensen et al.*, 2018]. This model is almost identical to the leeway drift method described in *Breivik et al.* [2011]. While this model is similar to the leeway model, a distinction must be made here. The leeway is defined as the "motion of the object induced by wind (10 m reference height) and waves relative to the ambient current (between 0.3 and 1.0 m depth)." This differs from the wind sensitivity factor, which is specifically for accounting for the wind slip of the object, where the effects of waves will be separated out in most of the following analysis.

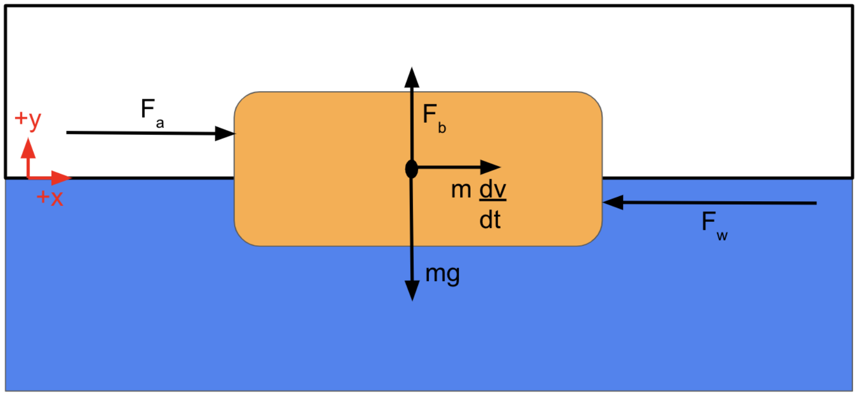

Figure 1.1: Schematic of forces on a drifting object in the ocean (Schematic is a graphical representation of analysis in *Wagner et al.* [2022]). Note that the opposing drag forces from the water and air are shown opposing for simplicity in the analysis. Still, this opposition is generally due to a difference in the speed of the air and water rather than the directions of the flows being in opposition.

1.2.2 Wave-Driven Transport

For clarity, wave-driven transport will be defined as transport due to Stokes drift, radiation stress gradients, transient rip currents, and surfing, amongst others. Each of these transport mechanisms is directly due to surface gravity wave processes; thus, the associated transport is wave-driven. Traditionally, wave-driven transport has been considered negligible compared to transport driven by currents and wind. However, there are regimes where wave-driven transport can be significant, such as in the surf zone [*Moulton et al.*, 2023b] and marginal ice zone [*Thomson et al.*, 2021; *Dumont*, 2022].

This work will focus on surfing transport and radiation stress gradient-driven transport. Surfing transport is where drifting buoyant objects are trapped on the face of a breaking wave and travel with the propagating broken wave, similar to a surfer moving with a wave [*Pizzo*, 2017a]. Radiation stress is the “excess flow of momentum due to the presence of waves [*Longuet-Higgins and STEWARTt*, 1964].” When surface waves break or attenuate, there is a gradient in the excess momentum flux. This gradient exerts a force on the water, which can drive an Eulerian current [*Thornton and Guza*, 1986]. This transport mechanism occurs where waves are breaking or attenuating, for example, in the surf and marginal ice zones. Radiation stress is a tensor quantity and therefore has multiple directions in which it can act. In the surf zone, radiation stress gradients drive set-up on the beach and along shore currents, while in the marginal ice zone, they drive ice compaction and along ice currents.

Both surfing and radiation stress gradient-driven transport processes are highly localized and are important on spatial scales generally smaller than those modeled in global transport models. Both processes also lack observations that can help to improve understanding of the processes [*Christensen et al.*, 2018]. This dissertation will address this need by improving the knowledge of two wave-driven transport mechanisms important in local regions, specifically the surf zone and the marginal ice zone.

1.2.3 Transport in the Surf Zone and Surfing Transport

The surf zone is the region of the ocean between the coast and where surface gravity waves start to break [*Lentz and Fewings*, 2012]. The surf zone is a hydrodynamically complex environment dominated by forcing from surface gravity waves [*Battjes*, 1988]. In the surf zone, waves shoal and break, which transfers energy and momentum into mean currents and turbulence [*Battjes*, 1988]. Typically, surface wave processes are responsible for transport through the mechanisms of Stokes drift, undertow, generation of rip currents, and generation of alongshore currents and set-up due to radiation stress gradients [*Moulton et al.*, 2023b].

Recent studies have investigated another mechanism for transport, surfing transport [*Eeltink et al.*, 2023]. Surfing transport occurs when waves break, and a drifting object is caught on the face of the broken wave, eventually forming a bore, and travels in the direction the bore propagates. The object travels with the bore until it “falls off” or the wave stops breaking. An important distinction is made here between surfing objects and water parcels. An “object” in the following work will specifically refer to any solid that is floating on the surface of the ocean. Enhanced transport of water parcels at the surface in breaking waves has been observed in numerical studies [*Deike et al.*, 2017b; *Pizzo et al.*, 2019]. It has been corroborated by laboratory experiments [*Eeltink et al.*, 2023]. Numerical studies have seen that when waves start to break, additional drift is observed at the breakpoint and that even one weakly breaking wave can induce drift that is twice that of the mean Stokes drift [*Deike et al.*, 2017b]. Field and laboratory experiments have shown that wave breaking can enhance the drift of a water parcel by approximately 30% compared to drift from Stokes drift only [*Pizzo et al.*, 2019; *Eeltink et al.*, 2023]. The numerical and laboratory studies also observed that surfing transport increases with increasing significant wave height and wave steepness [*Deike et al.*, 2017b; *Eeltink et al.*, 2023; *Pizzo et al.*, 2019]. Surfing transport has been successfully modeled using a stochastic jump-diffusion process model [*Eeltink et al.*, 2023]. Surfing events manifest as "jumps" in the position time series of the floating object, where the object moves significantly faster.

1.2.4 Transport in the Marginal Ice Zone

The marginal ice zone (MIZ) is defined as the edge of the sea ice pack where the ice concentration is less than 80% and greater than 15% [*Dumont*, 2022]. The marginal ice zone is a notoriously challenging zone to model accurately due to the complicated ocean-atmosphere-ice interactions that occur here and the lack of observations [*Dumont*, 2022]. Sea ice is said to be in "free-drift" when the ratio of ice speed to wind speed is greater than 2% or if the ice concentration is less than 85% [*Brenner et al.*, 2021]. The sea ice in the MIZ generally meets this criterion and, therefore, is in free drift. When ice is in "free-drift," it obeys the same force balance in Equation 1.2.

Sea ice is expected to drift at approximately $2\% - 4\%$ of the wind speed [*Steele et al.*, 1989]. Observations in the Bering Sea MIZ saw that ice drifts at approximately 3.2% of the wind speed [*Overland et al.*, 1984], which agrees with the "membrane" asymptote of wind sensitivity (3%) given in the *Wagner et al.* [2022] analysis. However, *Lund et al.* [2018] found that sea ice drift speed can be weakly correlated with wind speed, and instead, the ocean currents contribute heavily to the observed drift.

Waves propagating into the sea ice pack are attenuated. The attenuation is generally due to energy dissipation from turbulence being generated from flow against the bottom of the ice [*Thomson*, 2022]. Wave energy can also be lost to wave-induced ice floe collisions [*Herman*, 2018]. Waves carry energy and momentum with them as they propagate. As the waves are attenuated, a gradient in momentum flux is set up, also known as a radiation stress gradient [*Longuet-Higgins and STEWARTt*, 1964]. If the waves are oblique to the ice edge, the radiation stress gradients can be decomposed into a cross-ice component that can cause the ice to compact and an along-ice component that is expected to drive transport along the ice edge, analogous to surf zone setup and alongshore currents [*Thomson et al.*, 2021]. Observations of along ice drift are accurately described using a force balance between quadratic drag due to ice-ocean stresses and the radiation stress gradients (Equation 1.4) [*Thomson et al.*, 2021].

$$V(x) = H_o e^{-\alpha x} \sqrt{\frac{\alpha cos(\theta) sin(\theta)}{8C_D}} \tag{1.4}$$

H_0 is the open ocean significant wave height, x is the cross-ice distance, θ is the incident wave angle relative to the ice edge, α is a wave attenuation rate, and C_D is a drag coefficient for the ice. Numerical studies have shown that the presence of waves can enhance sea ice drift speeds by approximately 25% compared to wind-only drift [*Perrie and Hu*, 1997].

1.3 Overview

1.3.1 Objectives

The overall goal of this research is to advance our understanding of the wave-driven transport of buoyant objects in the surf zone and marginal ice zone by addressing the following objectives:

- **Objective 1**: Develop free-drifting buoys and create a dataset of measurements of nearshore surface kinematics and drift trajectories.

- **Objective 2**: Quantify the surface transport in the nearshore due to surfing for buoyant objects and assess the relative importance of surfing transport compared with wind and current-driven transport.

- **Objective 3**: Investigate the relationship of wave attenuation in ice and along-ice-edge surface transport. Assess the importance of radiation-stress-gradient-driven transport compared with wind-driven transport.

1.3.2 Outline

The remainder of this dissertation will address these objectives in the following chapters, outlined below:

- **Chapter 2** addresses Objective 1 and describes the development of the microSWIFT drifter and the creation of the DUNEX drifter dataset. This work was published in *Earth System Science Data* and is reproduced from the following citation. Additionally, the dataset collected in this project is published and publicly available in the second citation below.

  - Rainville, E., J. Thomson, M. Moulton, and M. Derakhti, Measurements of nearshore ocean-surface kinematics through coherent arrays of free-drifting buoys, Earth System Science Data, 15 (11), 5135–5151, doi:10.5194/essd-15 5135-2023, 2023a
  - Rainville, E., J. Thomson, M. Moulton, and M. Derakhti, Measurements of nearshore waves through coherent arrays of free-drifting wave buoys (uw drifters), `doi:doi:10.5061/dryad.hx3ffbgk0,2023b.`

- **Chapter 3** addresses Objective 2, characterizes the effect of surfing transport in the surf zone, and a stochastic model is developed to simulate surfing transport in a simple trajectory model. This chapter has been submitted to *Journal of Geophysical Research: Oceans* and is reproduced here following a first round of favorable reviews:

  - Rainville, E. J., Thomson, J., Moulton, M., Derakhti, M. (2025). Surfing Transport of Buoyant Objects Observed in the Nearshore. Authorea Preprints.

- **Chapter 4** also addresses Objective 2 by implementing the stochastic parameterization developed in Chapter 3 into the open source drift model OpenDrift. This work was submitted as a conference proceeding to the *Coastal Dynamics 2025* conference and has been reproduced from that work here:

  - Rainville, E. J., Thomson, J., Moulton, M., Derakhti, M., Hope, G., Dagestad, K., Breivik, O. (2025). Operational Modeling of Surfing Transport for Buoyant Objects in OpenDrift, Coastal Dynamics 2025 Conference Proceeding.

- **Chapter 5** addresses Objective 3 and finds that wave-driven transport is a dominant transport term near the ice edge. The along-ice transport in the marginal ice zone can be explained well by the summation of transport models, while cross-ice transport cannot be explained well. This work is in preparation for submission to a journal following the submission of the dissertation.

- **Chapter 6** summarizes the work completed in this dissertation. The conclusions also provide a discussion on the remaining open questions and possible applications of the research conducted in this dissertation.

Chapter 2

MEASUREMENTS OF NEARSHORE OCEAN-SURFACE KINEMATICS THROUGH COHERENT ARRAYS OF FREE-DRIFTING BUOYS

2.1 Introduction

The ocean covers most of the surface of the Earth, and in 2002 about 41% of the people on Earth lived within 100 km of the coast; we expect this population has continued growing [*Boehm et al.*, 2017; *Martínez et al.*, 2007]. We expect sea levels to rise and storm frequency and intensity to increase due to climate change, making coastlines more susceptible to flooding, infrastructure damage, and loss of life [*Intergovernmental Panel on Climate Change*, 2021]. Under moderate greenhouse gas emission forcing scenarios, we predict approximately $990 billion in damages to US coastlines between now and the year 2100 due to storm surge and sea level rise [*Neumann et al.*, 2015]. Wave forcing is a significant component of the total storm surge that causes flooding in low-lying coastal areas [*Bertin*, 2016]. As surface gravity waves propagate towards the shore, they also transport energy and momentum, which drives nearshore circulation and scalar transport [*Svendsen*, 2005]. Understanding these processes is essential for proper coastal management. Coastal managers use operational-scale forecast models that predict nearshore wave transformation, circulation, and transport but do not resolve individual waves and instead use a spectral representation of the waves in models such as SWAN (Simulating Waves Nearshore, [*Booij et al.*, 1996]) and WWIII (Wave Watch III, [*Tolman*, 1999]). Other wave models are wave-resolving, such as NHWAVE [*Derakhti et al.*, 2016; *Ma et al.*, 2012] and FUNWAVE [*Kirby et al.*, 1998; *Shi et al.*, 2012], but are computationally expensive and therefore are not used operationally. Since the operational models do not resolve individual waves, they do not resolve individual wave processes, such as wave breaking. Therefore, to represent these processes in the operational models, we must parameterize them. A dataset with both wave-resolved and wave-averaged measurements is useful to investigate the wave-averaged model parameterizations for individual wave processes, especially breaking.

Fixed sensors, such as acoustic waves and currents (AWAC) meters and bottom-mounted pressure gauges, are commonly used to measure ocean surface waves. The data products produced from these types of instruments include the energy density spectra from which bulk wave parameters such as significant wave height and mean wave period are computed at a specific location [*Birch et al.*, 2004]. These fixed sensors generally have robust statistics since they measure continuously in the same location. Remote sensing methods, such as stereo video techniques and thermal infrared imaging, among many others, are also used to measure the waves in the nearshore with reasonable accuracy [*Benetazzo*, 2006; *Carini et al.*, 2015]. While it can be challenging to deploy many fixed sensors and remote sensing systems, many field campaigns have been successful using these methods in the nearshore region [*Guérin et al.*, 2018; *Pezerat et al.*, 2022; *Lavaud et al.*, 2022; *Carini et al.*, 2015; *Elgar et al.*, 2001]. As a complement to the fixed sensors and remote sensing methods, wave buoys are another option for obtaining direct measurements of the surface kinematics in various sea states. Wave buoys can be either free-drifting or moored. Moored buoys are effectively Eulerian wave measurements, with some movement due to the scope of the mooring, while free-drifting wave buoys are closer to Lagrangian measurements but move as a result of the wind, currents, wave-induced drift (Stokes drift), and surfing on broken waves. Free-drifting buoys are essential for understanding how buoyant objects move in the nearshore [*Spydell et al.*, 2007; *Schmidt et al.*, 2003]. Free-drifting buoys tend to move through the surf zone very quickly; prior studies have reported buoys reaching approximately 50 $cm\, s^{-1}$ as a mean drift velocity. The velocities can be even larger in the presence of breaking waves and bores [*Schmidt et al.*, 2003; *Deike et al.*, 2017a].

Early wave buoys used measurements of heave, pitch, and roll to compute the scalar and directional energy spectra [*Kuik et al.*, 1988]. The next generation of wave buoys, including the SWIFT (Surface Wave Instrumentation Floats with Tracking) buoy, focused on using GPS velocity-based processing methods [*Thomson*, 2012b]. The GPS methods have facilitated smaller-scale and more cost-effective wave buoys with comparable accuracy to fixed platforms [*Herbers et al.*, 2012]. The GPS methods can be limited to measuring deep-water waves when using horizontal velocities and assuming circular wave orbits [*Thomson et al.*, 2018]. GPS-based drifters have also been used to investigate surf-zone dispersion and circulation patterns [*Schmidt et al.*, 2003, 2005; *Spydell et al.*, 2007].

There are now many small, GPS-based wave buoys in common usage. SWIFT buoys have been used to measure turbulence [*Thomson*, 2012b; *Thomson et al.*, 2016], wave-ice interactions [*Voermans et al.*, 2019] and wave-current interactions [*Zippel and Thomson*, 2017]. SWIFTs have also been used to quantify the breaking severity of individual waves [*Brown et al.*, 2019]. The company *SOFAR ocean* has since developed the Spotter buoy that uses a GPS-based wave measurement [*Raghukumar et al.*, 2019]. Many Spotter buoys are deployed worldwide to create a global network of wave measurements that can be assimilated into a global wave model and thus assist industries reliant on accurate forecasts of waves.

While buoys have inherent challenges in measuring nearshore waves, including distortion of surface elevation from accelerometer measurements [*Magnusson et al.*, 1999] and inability to resolve second-order non-linearity [*Forristall*, 2000], they are one of the few tools that can be used to obtain direct measurements of the kinematics of the surface. Buoys also provide the most direct observation of buoyant objects in the nearshore region. In the following sections, we discuss the deployment of microSWIFTs as part of the During Nearshore Events Experiment (DUNEX) (Section 2.2.1), the development of the version 1 microSWIFT wave buoy (Section 2.2.2), the creation of a large dataset including raw and post-processed measurements (Section 2.3), and the utility of that dataset for studying nearshore wave processes (Section 2.4).

2.2 Data Collection - During Nearshore Event Experiment (DUNEX)

This project is part of a larger collaborative effort called DUNEX (During Nearshore Event Experiment) that is funded through the US Coastal Research Program (USCRP, `https://uscoastalresearch.org`). The overall goal of DUNEX is to use rapid-response or other event-focused measurements and models to improve understanding of coastal impacts during storm events. Historically, it has been difficult to make measurements during such events. As a part of DUNEX, a 27-day field experiment was held from October 3-30, 2021. During the field experiment, we measured the motion of small-scale, free-drifting microSWIFT buoys in the inner shelf and surf zone. The microSWIFTs move with the free surface, thus providing measurements of surface kinematics. The following subsections will describe the data collection from DUNEX, including the field experiment, microSWIFT development, and data processing.

2.2.1 Field Experiment Site and Conditions - US Army Corps of Engineers Field Research Facility (FRF)

The experiment was conducted at the US Army Corps of Engineers (US-ACE) Field Research Facility (FRF) in Duck, North Carolina, USA (Figure 2.1). This site has a long history of being the focus of coastal dynamics experiments and is a relatively well-understood sandy beach environment [*Elgar et al.*, 1997; *Gallagher et al.*, 1998; *Feddersen et al.*, 1998; *Elgar et al.*, 2001; *Raubenheimer et al.*, 1996a]. The FRF maintains long-term observations via fixed in situ instrumentation, regular bathymetric surveys, remote sensing cameras, and LiDAR measurements. The FRF has an established local Cartesian coordinate system with the mean shoreline position located at approximately $x = 100$ meters, increasing offshore, and the location of the pier in the middle of the study site at approximately $y = 500$ meters, increasing northward (Figure 2.1, panel (b)). The bathymetry typically includes a large shore-perpendicular channel at approximately 500 meters in the alongshore direction underneath the pier due to scour. During the October 2021 study time period, a long shore-parallel sandbar at approximately 200 meters in the cross-shore direction was present (Figure 2.1, panel (c)). Previous studies suggest the bathymetry at this field site changes on timescales of hours to days [*Ruessink et al.*, 2001].

A cross-shore transect of instruments (near $y = 900$ meters) is deployed and maintained by the FRF and includes several sensors in and near the surf zone that are relevant to this study (locations shown in Figure 2.1, panel (b)). The FRF completes all data processing for these instruments, and the data products produced are publicly available (data available at `https://frfdataportal.erdc.dren.mil/`). This sensor array includes a Nortek Acoustic Waves and Currents (AWAC) sensor in 4.5 meters mean water depth, another AWAC in 6 meters mean depth, and an array of pressure gauges in 8 meters depth used to estimate wave-directional spectra (Figure 2.1, Panel (b)). The data from these sensors are processed by the FRF staff to produce estimates of the bulk parameters of significant wave height, mean wave period, and mean wave direction for the duration of the field experiment (Figure 2.2) along with many other wave and current data products. During the experiment, significant wave heights ranged from 0.5 to 3 meters, mean wave periods from 5 to 15 seconds, and mean wave directions from 20 to 120 degrees relative to true North (where the cross-shore normal direction is 71.8 degrees clockwise of true North).

2.2.2 microSWIFT Buoy Development and Deployments

The microSWIFT buoys are named after their predecessor, the SWIFT buoy [*Thomson*, 2012b]. The version described herein is version 1; the Thomson et al (CEJ, in revision) for a description of other versions. The electronics and sensors of the microSWIFT are housed inside a Nalgene-brand water bottle with a length of 21 cm and a diameter of 9 cm (Figure 2.3). The Nalgene water bottle has a standard lid, and an O-ring was added to the mouth of the bottle to reduce water intrusions. The bottle sits on its side in the water, giving a keel of 4.5 cm and a sail of 4.5 cm. The overall microSWIFT has a mass of 0.7 kg. It is powered by two rechargeable lithium-iron D-cell batteries and has an approximate lifespan of 48 hours under the current operating configuration. The instruments on board

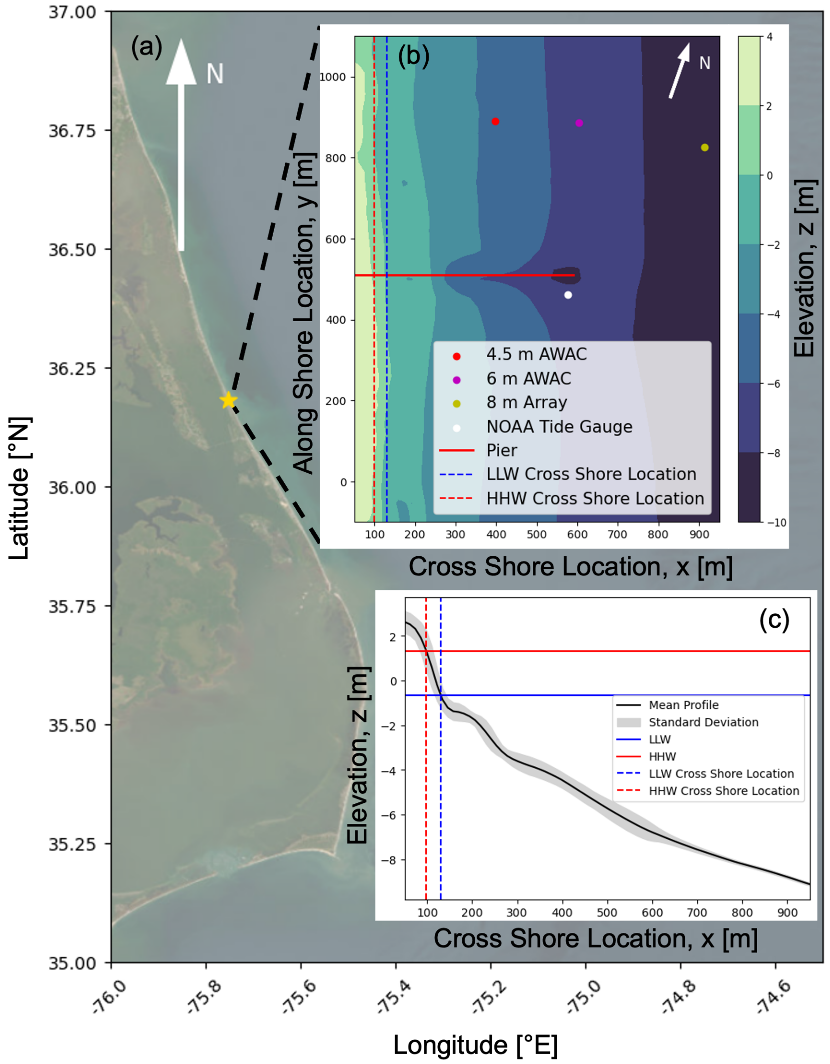

Figure 2.1: (a) Aerial imagery of the Outer Banks of North Carolina, US, where the gold star is the location of the US Army Corps of Engineers - Field Research Facility (FRF) (© Source: Esri, Maxar, Earthstar Geographics, and the GIS User Community). Panel (b) shows the bathymetry contours at the field site from October 21st, 2021, relative to the NAVD88 datum and locations of fixed instrumentation (Data provided by USACE, Field Research Facility, `https://frfdataportal.erdc.dren.mil/`). Panel (c) shows the average cross-shore profile of the bathymetry with one standard deviation above and below the average. The higher high water (HHW) and lower low water(LLW) levels measured during the experiment are also shown.

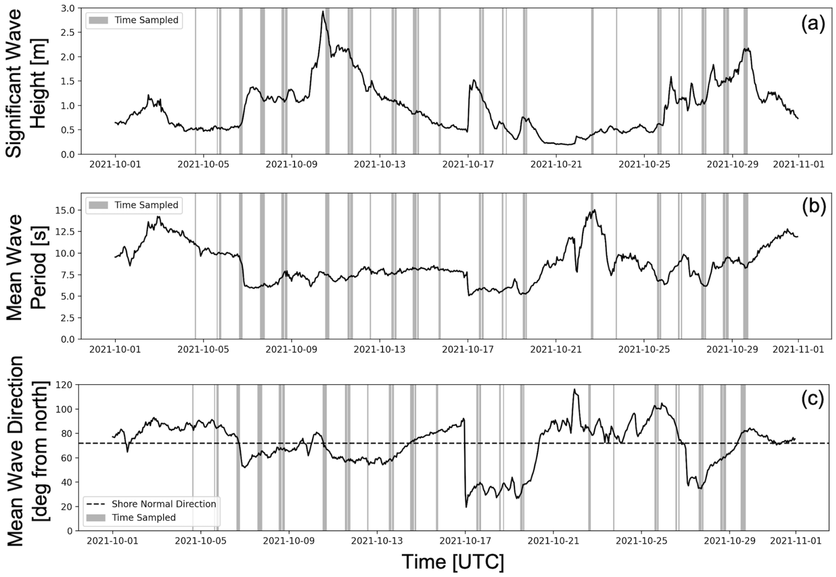

Figure 2.2: Conditions sampled during the main DUNEX experiment from the Field Research Facility 8 m array. Time series of the (a) significant wave height and (b) mean wave period, and (c) mean wave direction (Data provided by USACE, Field Research Facility, `https://frfdataportal.erdc.dren.mil/`). The gray patches show the times that we deployed microSWIFT arrays.

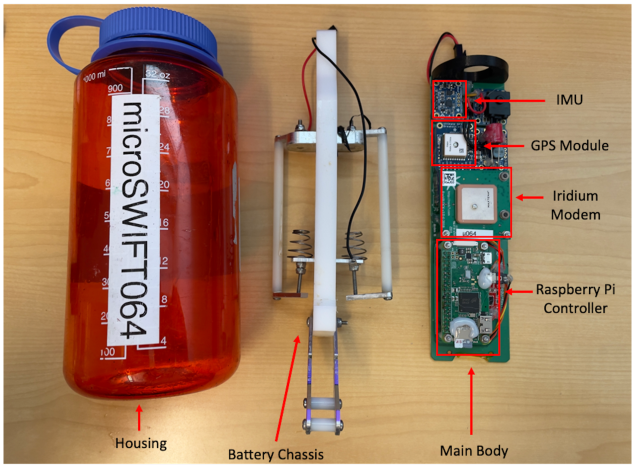

Figure 2.3: Layout of microSWIFT hardware components with the Nalgene water bottle housing on the far left, battery chassis in the middle, and electronics on the far right. The individual chipsets include a Raspberry Pi Zero as the main processor, a GPS module, an inertial measurement unit(IMU) that contains accelerometers, gyroscopes, and magnetometers, and an Iridium modem.

the microSWIFT are a GPS module and Inertial Measurement Unit (IMU). A Raspberry Pi Zero, a small microprocessor with a Raspian Linux operating system, controls the entire system. The microSWIFT also has an Iridium modem (RockBLOCK 9603) onboard that sends processed data from the microSWIFT to a shore-side server. The Raspberry Pi Zero also has an SD card where all raw data is stored and downloaded from when the buoys are recovered. Each component of the microSWIFT is soldered directly onto a custom circuit board (Figure 2.3). This is version 1 of the microSWIFT.

All software for the microSWIFT is written in the Python computing language and is published on a public Github repository for open source access (`https://github.com/SASlabgroup/microSWIFT`). The flow of onboard software is shown in Figure 2.4. The microSWIFT is controlled by one primary function named *microSWIFT.py* that controls all other functions. When the microSWIFT boots up, a service script named *microSWIFT.service*

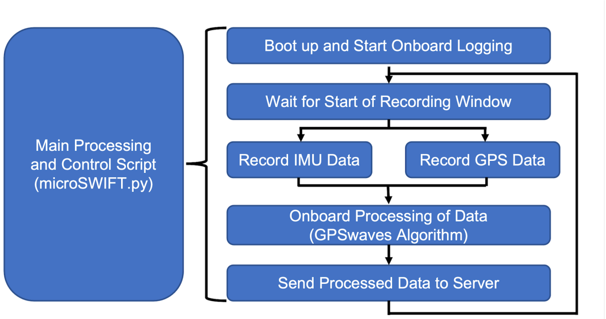

Figure 2.4: Flow of operations for software onboard the microSWIFT wave buoys.

runs and starts the main *microSWIFT.py* control function. As *microSWIFT.py* starts, it creates a log file where all functions onboard the microSWIFT are logged so the user can see if any errors are occurring or the instrument is working correctly. The microSWIFT central control is split into two windows, the record and process/send windows, with user-defined lengths based on universal coordinated time (UTC). Within the record window, the microSWIFT concurrently records GPS and IMU data and writes the data directly to a file. The microSWIFT enters the process/send window when the record window ends. Here, the microSWIFT reads in all of the recorded GPS velocities and uses the algorithm *GPSwaves* described in *Thomson* [2012b] and *Thomson et al.* [2018] to compute an estimate of the wave energy scalar spectrum, bulk parameters, last known location, and the average north-south and east-west velocities over the length of the last record window. These processed values are then packaged into a binary message sent through the Iridium modem to a shore-side server where the data can be parsed and used. The *GPSwaves* algorithm is very effective for deep water waves; however, it uses an assumption of circular wave orbital velocities to estimate the scalar energy spectrum. The elliptical orbits of shoaling waves in shallow water violate this assumption. The nonlinearity of shallow water waves and breaking waves further complicates the usage of GPS horizontal velocities to infer wave elevations. For nearshore applications, we developed a new processing method described in Section 2.3.

As the microSWIFT drifts, the IMU and GPS sensors measure the motion of the bottle.

Sensor	Chipset	Sensitivity	Range	Average Noise Variance
3-axis Linear Accelerometer	FXOS8700CQ	0.244 $mg\ LSB^{-1}$ 0.488 $mg\ LSB^{-1}$	$\pm 2g$ / $\pm 4g$	0.00004 $m\ s^{-2}$
3-axis Magnetometer	FXOS8700CQ	0.1 $\mu T\ LSB^{-1}$	± 1200 μT	2 μT
3-axis Gyroscope	FXAS21002C	15.625 $mdps\ LSB^{-1}$	± 500 dps	0.045 dps

Table 2.1: Inertial Measurement Unit sensor specifications for accelerometer, gyroscope, and magnetometer onboard each microSWIFT. Note that the dynamic range of the accelerometer was adjusted from 2g to 4g part-way through the field experiment on Mission 53 on October 23rd, 2021.

The IMU measures accelerations, rotation rates, and magnetic heading in three orthogonal spatial dimensions at a rate of 12 Hz in the reference frame of the buoy. The chipsets, sensitivities, and ranges of the accelerometer, gyroscope, and magnetometer are shown in Table 2.1. The GPS receiver is an MT3339 chipset that samples at a rate of 4 Hz and measures latitude, longitude, and horizontal velocities in the Earth reference frame. These measurements provide a comprehensive picture of how and where each microSWIFT moves in response to waves and surface currents.

Each microSWIFT provides detailed information about a single point in space and time. However, when deployed in large numbers as coherent arrays, the microSWIFTs can be processed together to improve measurements in certain areas or explore spatial variability. The deployed coherent arrays ranged in size from two to fifty microSWIFTs. The microSWIFTs were deployed by throwing them from the pier, paddling them out on surfboards, dropping them from a helicopter, or providing them to local lifeguards who dropped them off a jetski. The microSWIFTs were retrieved when they eventually washed up on the beach or were chased down using surfboards, jet skis, and boats. To track the buoys in live time, we deployed 'shepherd' buoys which had the same hull and ballast as the microSWIFTs but had a live tracking GPS in them to track the current movement of the buoys as they drifted. Over the course of the experiment, 2,187 buoys were deployed, including the shepherd buoys, and only one was lost. We refer to each deployed array as a "mission." Drift tracks (location of each microSWIFT over the time of a mission) from the microSWIFTs on two example missions are shown in Figure 2.5. After data cleaning, the dataset consists of 67 missions spanning 27 days. The shoreline and surf zone edge estimates are added to panels (a) and (b) in Figure 2.5 to add context to the microSWIFT deployment. The shoreline and surf zone edge are both estimated using along shore averaged bathymetry (measured on October 21st, 2021 described in Figure 2.1) in combination with the mean water level from the NOAA tide gauge (location shown in Figure 2.1, panel (b)). For each mission, the mean water level during the deployment is added to the along shore bathymetry profile to give a cross shore depth profile during the mission. The shoreline is then estimated as the cross shore location where the depth during the mission equals zero on the along shore averaged profile. Waves are expected to begin breaking when the ratio of wave height H_s to water depth d,

$$\gamma_s = \frac{H_s}{d}, \tag{2.1}$$

reaches a certain threshold. Using this definition of γ_s, the variable H_s represents the offshore significant wave height, here measured from the 8 m-pressure gauge array (location in Figure 2.1, panel (c)), and the variable d represents the water depth during the mission. Values of γ_s from the Duck, NC field site have been observed to be between 0.4 and 0.8 [*Sallenger Jr and Holman*, 1985]. Further studies have shown that within the inner surf zone at the Duck, NC field site γ_s can reach as low as approximately 0.275 and as high as 0.375 at depths greater than 0.8 meters [*Raubenheimer et al.*, 1996a]. Smaller values of γ_s drive the breaking

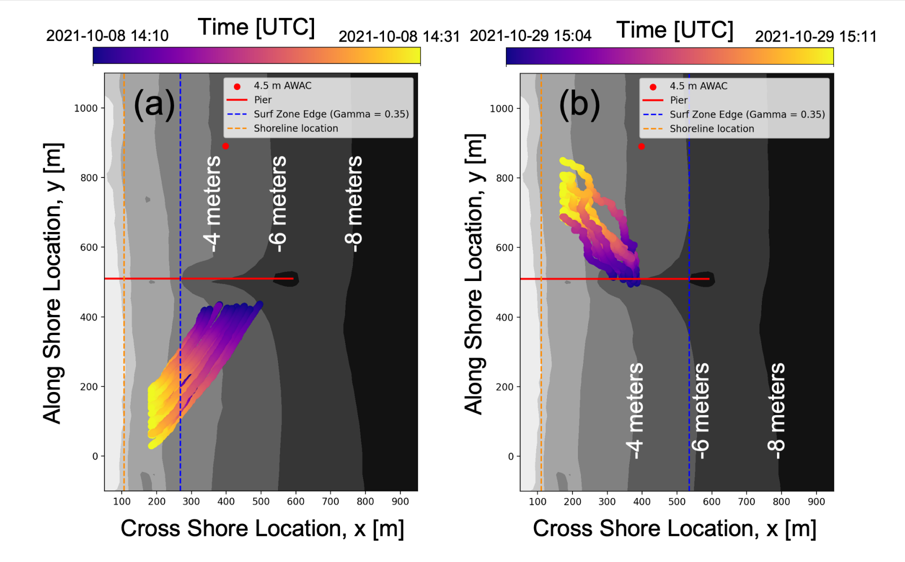

Figure 2.5: Example drift tracks(location of microSWIFTs over time) of microSWIFT arrays during a mission plotted over of the bathymetry digital elevation model shown in Figure 2.1 Panel (b). Panel (a) shows the drift tracks from mission 16, which has 19 microSWIFTs deployed, and Panel (b) shows the drift tracks from mission 79, which has 13 microSWIFTs deployed. Approximate shoreline and surf zone edges are shown for each mission.

depth to deeper water, and larger values drive the breaking depth to shallower waters. From these observed values, we chose $\gamma_s = 0.35$ to provide a representative estimate of the surf zone edge location. These estimates are shown in both panels of Figure 2.5, and the same estimation method is used to add context to the analysis later on. The choice of $\gamma_s = 0.35$ is a traditionally low value but is used as a conservative estimate to include the outer surf zone where intermittent breaking is prevalent.

2.3 Data Levels and Data Processing

We separate three levels of data as follows:

- Level 0: Text files of raw data from the GPS and IMU from each microSWIFT, organized by the mission number
- Level 1: GPS and IMU measurements stored in a netCDF file, data have been cleaned and interpolated onto the same time datum for each mission
- Level 2: IMU accelerations that have been corrected to the Earth frame of reference, with velocities and positions computed from these corrected accelerations

First, we download the Level 0 raw measurements from the microSWIFTs, organize them into folders for each mission, then read the data from the text files. We then create a single time array with the mission's manually recorded start and end times. The start time is when all the microSWIFTs entered the water, and the end time is when all the microSWIFTs are out of the water. The time step in this time array matches the IMU sample rate of 12 Hz. We then match the IMU measurements to this time array and linearly interpolate the GPS data to match the time array. Any gaps in the IMU measurements are filled with linear interpolation. Gaps in GPS measurements occur due to the buoys being overtopped or plunged underwater. These gaps are filled using linear interpolation but are generally minor. *Schmidt et al.* [2003] used similar GPS-based drifters and found 95% data return rates seaward of the surf zone and 75% data return rates within the surf zone but found linear interpolation was an appropriate method to fill the data gaps, so this methodology is followed.

2.3.1 Data Cleaning and Level 1 Data

We then clean these data using a combination of automated and manual methods. First, we create a spatial threshold to remove data points while a microSWIFT is on the beach. We create this threshold using a digital elevation model of the bathymetry at the FRF from October 21st, 2021 (elevation is relative to NAVD88) (Figure 2.1, Panel (b)) and the mean water level during each mission measured by a NOAA tide gauge (Location in Figure 2.1, Panel (b)). The mean water level is added to the bathymetry measurements to find the depth at each surveyed point during each mission. We find the furthest offshore dry point as the furthest offshore positive value. We then add a buffer of two additional meters to the furthest offshore dry point and set this location as the spatial threshold for that mission. We replaced any points that cross this beach threshold on the beach side with "NaN" values in the dataset. While there were changes in the bathymetry during the experiment, we are only using this survey to define an approximate location of the beach extent to do a bulk data cleaning and add some approximate context for these data. Further detailed analyses of other bathymetry surveys will be completed in future studies using this dataset. After this automated cleaning method, we manually inspected each data channel for any spurious points that were replaced with "NaN" values.

The recorded start and end times of the mission were also manually adjusted to reflect the times the microSWIFTs were actually in the water. Large spikes in acceleration at the beginning of a deployment tend to represent times when the start time was recorded too early and was adjusted to remove these spikes. Similarly, the microSWIFTs were sometimes picked up in the middle of the mission, e.g., during jetski-based deployments, and those times were manually removed as well. All data cleaning, including start and end time adjustment and individual point cleaning, is noted in Appendix B in *Rainville* [2022], and the cleaning notes are stored in the metadata of each netCDF and in the GitHub repository that contains all processing code (`https://github.com/SASlabgroup/DUNEXMainExp`). The IMU data is then despiked using a piecewise cubic Hermite interpolating polynomial (PCHIP) function, a shape-preserving interpolation scheme used to reduce overshoot oscillations and maintain continuity [*Karim et al.*, 2014]. Points with a value greater than four scaled median absolute deviations from the median are considered outliers and replaced using the PCHIP method. The cleaned and despiked dataset is considered the Level 1 data.

2.3.2 Level 2 Data

We use the gyroscope and magnetometer measurements to correct the accelerations from the body reference frame to the Earth reference frame using a 9 degrees-of-freedom indirect Kalman filter for IMU sensor fusion that is prepackaged in the MATLAB navigation toolbox (MATLAB Navigation Toolbox 2022b, https://www.mathworks.com/help/nav/multisensor-positioning.html). A schematic representation and an example corrected signal are shown, respectively, in Panels (a) and (b) of Figure 2.6. The corrections to the acceleration are generally minor (see changes between uncorrected and corrected vertical acceleration in Figure 2.6, Panel (b)) but have a significant impact on the integrated signals and eventually computed energy spectra and bulk wave parameters. We then use a first-order Butterworth band-pass filter to remove low ($f < 0.05$ Hz) and high ($f > 0.5$ Hz) frequency noise outside of the gravity wave band from the signals. We then integrate the filtered acceleration signals via a time domain cumulative trapezoid method to velocities. The velocities are filtered again with the same filter to eliminate any spurious integration errors, then integrated to estimate positions, and finally filtered one last time to eliminate integration errors. The corrected and filtered accelerations, velocities, and positions are the Level 2 data.

2.3.3 Spectral Exploration of microSWIFT Data

We assume that the main control of nearshore wave evolution is the local bathymetry, and therefore measurements in similar depths at the same time should be comparable in a spectral and statistical framework [*Gomes et al.*, 2016]. Spatial variability in the bathymetry can also lead to areas of convergence and divergence of wave energy through refraction, causing spatial variability of wave properties. These spatial differences can also be exaggerated through the blocking of obliquely incident waves by the pier leading to reduced wave energy in the ‘shadow’ as much as 50% reduced at 200 meters down-wave of the pier [*Elgar et al.*, 2001]. We also expect measurements outside the surf zone to be more reliable for estimating wave properties since they are exposed to fewer breaking waves. Breaking waves tend to manifest

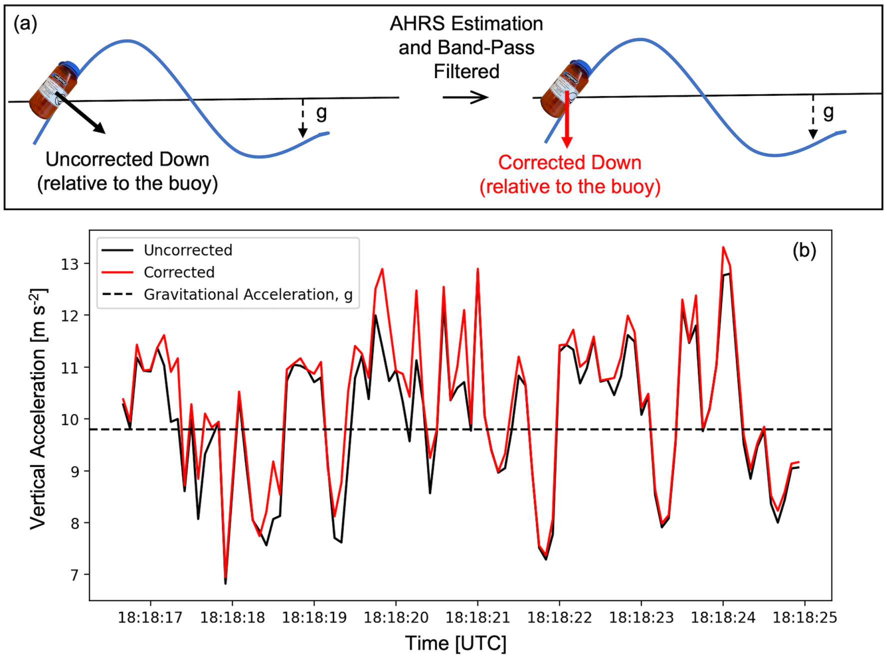

Figure 2.6: Panel (a) shows a schematic representation of the acceleration corrections from the body reference frame of the microSWIFT to the Earth reference frame through the use of the attitude and heading reference system (AHRS) estimation and band-pass filtering. Panel (b) shows an example portion of a signal to see how the vertical acceleration is corrected.

as short bursts of high frequency and amplitude accelerations [*Sinclair*, 2014; *Brown et al.*, 2019; *Feddersen et al.*, 2023]. Integrating these acceleration bursts can lead to spuriously large or nonphysical sea surface elevations; therefore, we expect the best agreement of wave measurements when the buoys are outside the surf zone or in the outer surf zone where breaking is more intermittent.

The 4.5-meter AWAC is currently at a bottom elevation of -4.8 meters relative to NAVD88 due to changes in the bathymetry since the instrument was initially deployed and named. In prior studies, AWAC sensors have been validated for use in the nearshore environment [*Pedersen et al.*, 2007]. Known limitations of the AWAC include excess noise at high frequencies and reduced response at low frequencies. To compute an energy spectral density estimate from an individual microSWIFT that we can compare to the 4.5-meter AWAC, we use data when an individual microSWIFT was at a location that corresponded to a bottom elevation between -4.3 and -5.3 (± 0.5 meters around the current elevation of the AWAC) meters based on the local bathymetry measurements in Figure 2.1, Panel (b). As an example, mission 18 has four microSWIFTs that were between these depths for almost ten consecutive minutes as they drifted through the surf zone (Figure 2.7, Panels (a) and (b)).

The microSWIFT spectra are computed using Welch's method, with five-minute (3600 sample) Hanning windows and 50% overlap between adjacent windows. The energy in each of the five adjacent frequencies is band-averaged to improve the statistical robustness of each estimate. The equivalent degrees of freedom for each microSWIFT spectrum is 28. This is based on the ten-minute time series (7200 samples at a 12 Hz sampling rate) used for each spectral estimate with three five-minute windows (50% overlap). Each window contributes 2 degrees-of-freedom and band-averaging the five adjacent frequencies increases the effective degrees of freedom by a factor of five. Due to the 50% overlap of the Hanning windows, the equivalent degrees of freedom are reduced to 92% of the maximum degrees of freedom [*Nuttall and Carter*, 1980]. Therefore, the equivalent degrees-of-freedom for the microSWIFT spectra is 28 (3 windows * 2 degrees-of-freedom * 5 frequency bands * 0.92 = 28). The AWAC measurements consist of a 34-minute record with a sample rate of 2 Hz,

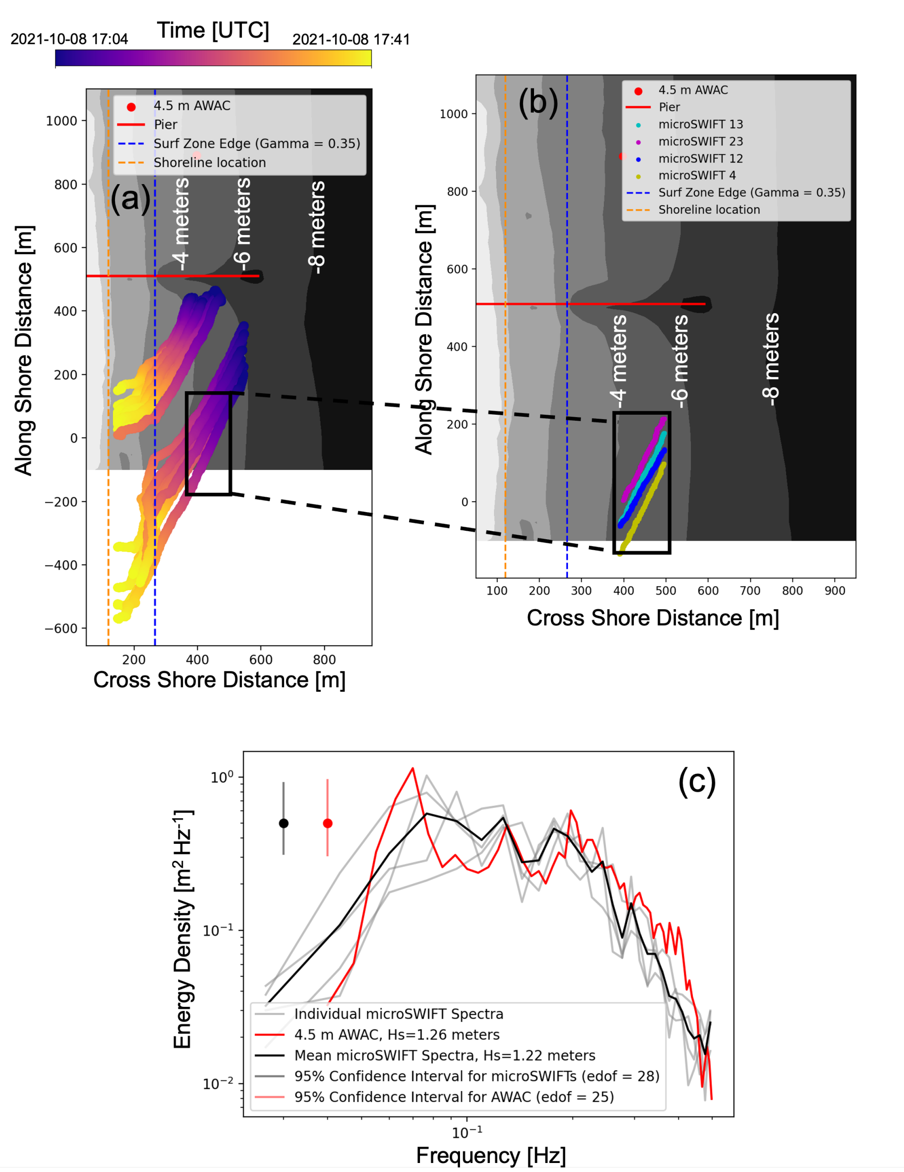

Figure 2.7: Comparisons of Panel (a) shows the drift tracks of the microSWIFTs from mission 18 plotted over the surveyed bathymetry DEM. Panel (b) shows a subset of the drift tracks where the bathymetry along each track is between -4.3 and -5.3 meters, and each microSWIFT is a different color. Panel (c) shows the spectra computed from a subset of the sea surface elevation time series for each microSWIFT. Significant wave heights are computed by numerically integrating the AWAC and averaged microSWIFT spectra.

and spectra are computed with 13 50%-overlapping windows (512 points per window) and no band-averaging, leading to approximately 25 degrees-of-freedom, comparable to that of the microSWIFTs [*Christou et al.*, 2011]. The staff of the Field Research Facility process the AWAC data following the methods described by *Earle et al.* [1999]. These spectral characteristics result in a frequency resolution of 0.016 Hz. Note, however, only the data products processed by the FRF are used in this study, and no processing of the raw AWAC data is done in this study. Each of the spectra computed from the microSWIFTs compares well with the spectra, and the averaged spectra also compare well with that reported from the 4.5 m AWAC (Figure 2.7, Panel (c)). The qualitative agreement of each microSWIFT spectra and the AWAC suggests that the measurements are useful for further investigating wave properties with the buoys. Future use of these data may investigate the estimation of directional spectra and directional moments, but they are not investigated in this study.

2.3.4 Zero-Crossing Exploration of microSWIFT Data

Since the buoys drift quickly through the surf zone, it is not always reasonable to compute spectra from each buoy since the buoys enter areas with active breaking, and as they move through different depths, the signal is not necessarily stationary. In this case, we use the arrays of microSWIFTs coherently to estimate the significant wave height. The measurements from each buoy are combined using a zero-crossing algorithm, which identifies individual wave realizations along the drift track of each microSWIFT (Example processing of data using the zero-crossing approach is shown in Figure 2.8). Panel (a) shows the drift tracks of each microSWIFT over time, while Panel (b) shows that each track is a different microSWIFT; each track is now a different color. Using the zero-crossing algorithm on each sea surface elevation time series, we define an individual wave realization as the data between two consecutive upward zero-crossings in elevation (Figure 2.8, panel (d)). The height of each wave realization, from crest to trough, and the average location of the wave realization are also defined by this method. Since the microSWIFTs are spatially distributed in the nearshore and sampling simultaneously, some microSWIFTs will measure the same wave as it propagates past multiple buoys. We treat this like a physical 'sampling with replacement' method similar to Monte Carlo or Bootstrap simulation methods known as re-sampling techniques. These types of re-sampling techniques are used to improve the confidence in a statistical estimate from a finite amount of data [*Thomson and Emery*, 2014]. In this case, the finite data is the short period that the buoys sample an area, but multiple datasets from different microSWIFTs, occasionally containing measurements of the same wave, can help improve confidence in the statistics. The height of each wave realization is then aggregated, and the distribution of wave heights sampled during this mission is shown in Figure 2.8, Panel (e).

The distribution of wave heights follows a Rayleigh distribution as is expected for nearshore surface gravity waves [*Thornton and Guza*, 1983]. The significant wave height is computed from aggregated wave height measurements outside the approximate surf zone. The significant wave height is computed by first computing the root-mean-square of the wave heights and then multiplying by a factor of 1.414 to convert to significant wave height for a Rayleigh distribution [*Dean and Dalrymple*, 1991]. An example of where this measure falls on the Rayleigh distribution is shown as a vertical line on the wave height distribution in Figure 2.8, Panel (e). By applying this processing to each mission in the experiment, we get a total of 116,307 wave realizations across the experiment. Using the locations of the wave realizations, the measured bathymetry, and the water level gauge, we can approximate the depth of each wave realization across the experiment. Most wave realizations were on the south side of the pier between -2 and -6 meters in bottom elevation.

We evaluate this zero-crossing processing method by comparing significant wave height estimates from the microSWIFTs to the 4.5-meter AWAC, 6-meter AWAC, and 8-meter pressure sensor array (6-meter AWAC and 8-meter array estimates have been corrected for expected shoaling using linear wave theory). Like the 4.5-meter AWAC, the 6-meter AWAC has shifted over time and is now at a bottom elevation of -6.83 meters. We first find, for each mission, all wave realizations that are located outside of the approximate surf zone. With this subset of waves, we compute the significant wave height as described previously.

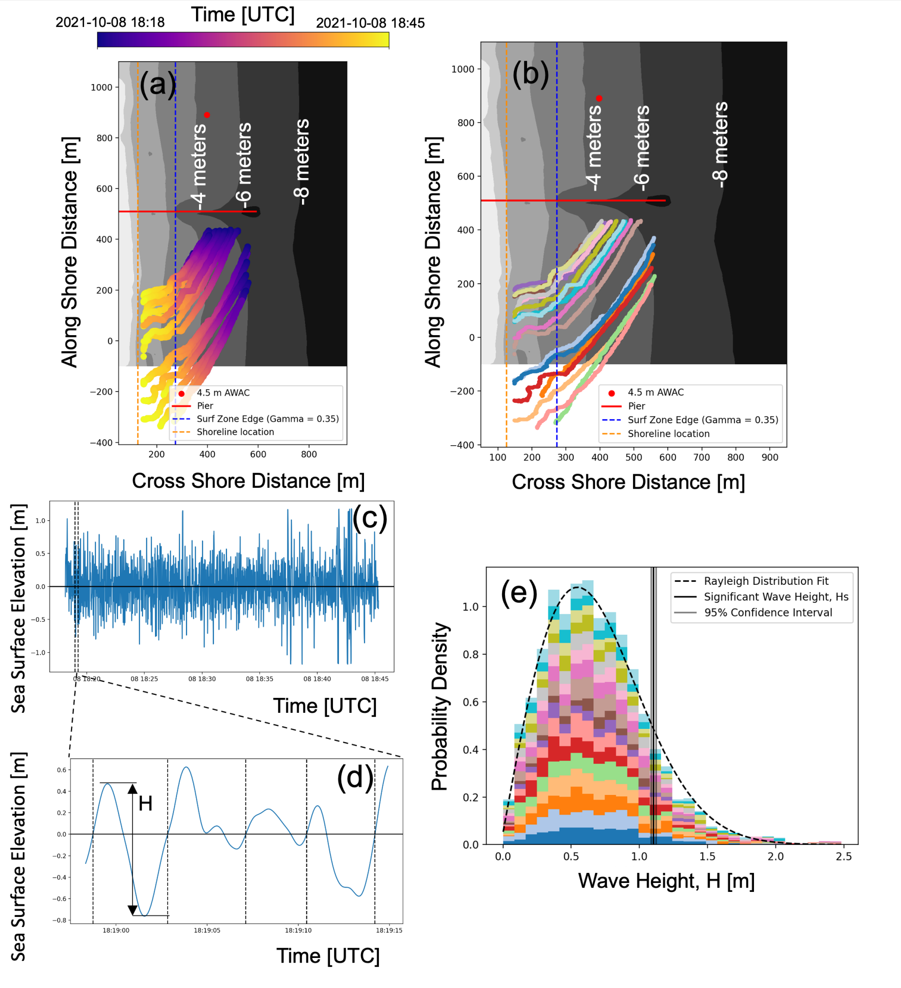

Figure 2.8: Example of steps in processing each mission. Panel (a) shows the drift tracks of the microSWIFTs from mission 19 plotted over the surveyed bathymetry DEM. Panel (b) shows the same drift tracks as Panel (a) but shows each microSWIFT as a different color. Panel (c) shows the time series of computed sea surface elevation, with one time series being highlighted as an example. Panel (d) is a zoomed-in portion of the overall time series showing the locations of zero crossings and how we define the height of an individual wave in a time series. Panel (e) is the probability density of all wave heights, seaward of the approximate surf zone edge, where the colors show the contribution from each microSWIFT with the corresponding color. The probability density distribution fits a Rayleigh distribution. The vertical line shows the computed significant wave height for this distribution and the 95% confidence interval of the estimate.

To calculate a significant wave height from one of these subsets of data, we require at least 30 wave realizations in the distribution. Thus, we do not compute a significant wave height for every mission. We compare the computed significant wave heights to those from the 4.5-meter AWAC, 6-meter AWAC, and 8-meter array (Figure 2.9).

The linear regression between the 4.5 m AWAC and microSWIFT array significant wave heights has a slope of 0.61 and an R^2 value of 0.74, showing a positive correlation between the two significant wave height estimates. This agreement is reasonable given that the microSWIFTs are measuring at a different alongshore location than the AWAC, although in similar water depths. We also expect that the microSWIFT arrays have more variability in their significant wave height estimates since the sampling windows are shorter than the AWAC, potentially over-representing or under-representing the largest and least likely waves in the distribution. Further underestimation could be due to the microSWIFTs being within the 'shadow' of the pier. Being in the pier 'shadow' is defined here as missions when the average location of the microSWIFTs during a mission is within 200 meters of the pier, and waves are coming from the other side of the pier based on the mean wave direction from the 8-meter array (furthest offshore sensor). The significant wave height measurements from the 6-meter AWAC and 8-meter array are also adjusted to be in the same depths using linear wave theory and compared to show agreement between multiple sensors for a more robust comparison. The agreement in significant wave height and scalar energy density spectra supports that the Level 2 data are useful for investigating wave spectra and statistics.

2.4 Data Use

The following section will describe some potential uses for this dataset. The level 1 data in this dataset consists of the cleaned and despiked GPS positions, GPS horizontal velocities, accelerations in the body frame of reference, rotation rates, and the magnetic heading of the buoys. These data channels contain information that can be used to investigate wave breaking motions and the transport of buoyant objects in the nearshore region under various conditions. The location of measurements made by the microSWIFTs during this experiment

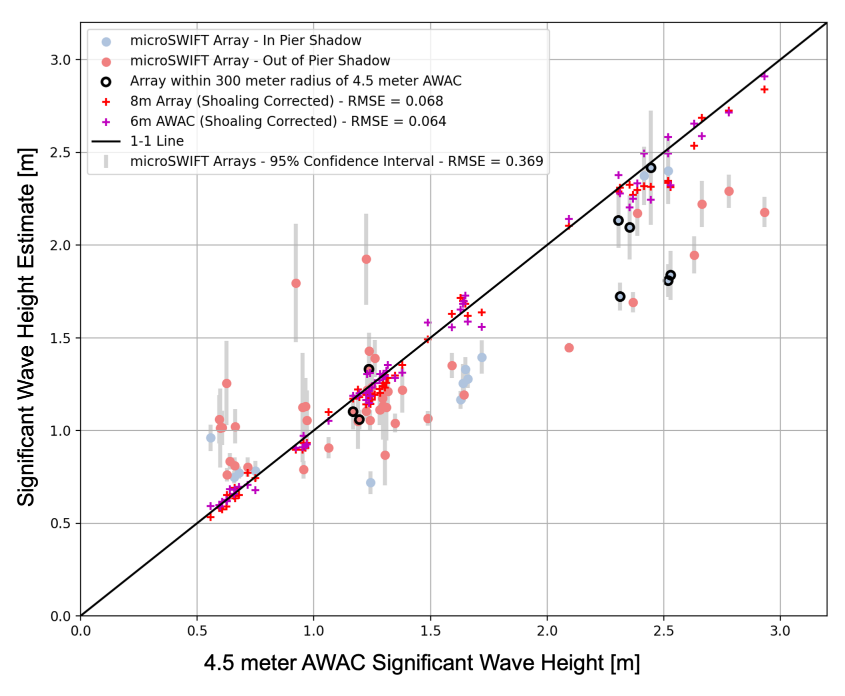

Figure 2.9: Comparison of the estimated significant wave heights from the microSWIFT arrays, 6-meter AWAC, and 8-meter pressure sensor array (6-meter AWAC and 8-meter array have been corrected for shoaling) to the estimates from the 4.5 m AWAC. While the microSWIFT arrays are not in the same water depth as the 4.5 m AWAC, we see that the microSWIFT arrays characterize the size of the waves with good comparison to the 4.5 m AWAC. The gray bars indicate 95% confidence intervals around each of the significant wave height estimates, computed using a bootstrap method from the distributions of wave heights. The colors of the estimates depict if the microSWIFT array is in the 'shadow' of the pier where we expect a reduction in wave energy. For significant wave heights greater than 2 meters, intermittent breaking may be occurring at the 4.5 meter isobath leading to worse agreement between the AWAC and microSWIFT measurements.

is shown in Figure 2.10. The orange dashed line shows the average location of the shoreline during the experiment. The closest-to-shore and furthest-off-shore surf zone edge estimates during the experiment are shown and are based on the smallest and largest offshore significant wave heights during the experiment, respectively. This shows many measurements both outside and inside the surf zone. These measurements can help investigate buoyant particles' cross and along-shore transport under various forcing conditions. The microSWIFTs move with both the waves and the currents. They are buoyant, and thus they also tend to 'surf' on the broken waves. The buoys surfing can enhance the transport of these objects [*Pizzo*, 2017b]. This type of motion affects similar objects transported in the surf zone, such as large algae, e.g., Sargassum, a buoyant seaweed affecting coastlines in the south-eastern US [*Webster and Linton*, 2013]. The mean surface currents, Stokes drift, and rip currents are resolved within transport models for surface-constrained particle motion [*Moulton et al.*, 2023a].

The process of 'surfing' is generally unresolved, and this dataset is well suited to investigate this process. Examples of potential buoy surfing events are shown in Mission 18 (Figure 2.7, panel (a)) and Mission 19 (Figure 2.8, panel (a)), where all buoys have a sudden change in direction to be nearly directly shoreward within the surf zone. This phenomenon is not observed across all missions. For example, this phenomenon does not occur in Mission 16 (Figure 2.5, panel (a)). These data can be used to investigate under what conditions this occurs and how it could be further incorporated into models that predict trajectories of buoyant particles. Applications range from scalar transport of plastics to marine search and rescue operations.

Along with the transport of the microSWIFTs, the GPS sensor records the horizontal (east-west and north-south) velocities, and the IMU records the accelerations and rotation rates of the buoy. These data from multiple buoys deployed in a coherent array can be used to investigate the cross and along-shore spatial variability of surface motion. An example of this type of analysis would be comparing the differences in cross-shore velocity and vertical acceleration measured by a buoy inside and outside the surf zone. Figure 2.11 shows an

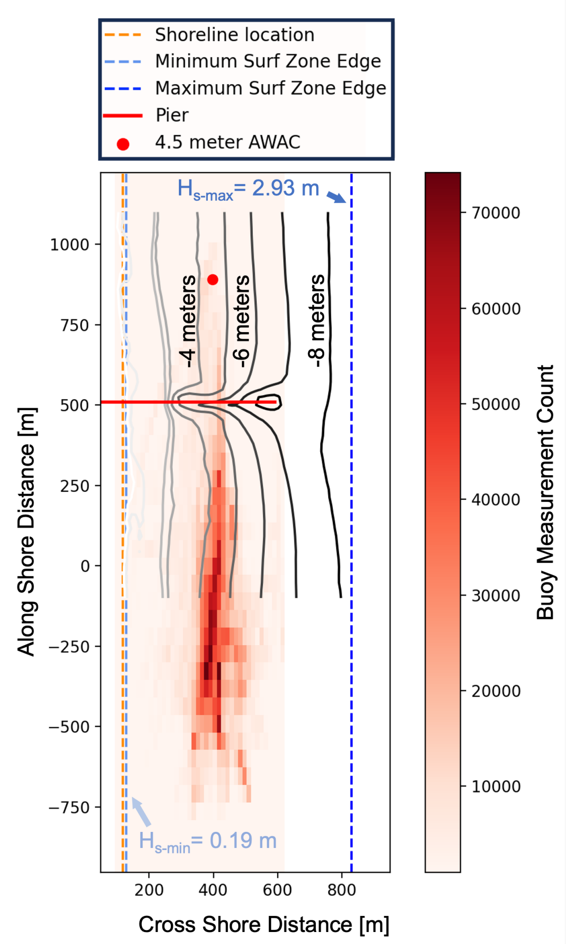

Figure 2.10: Density of Level 1 buoy measurements over the entire experiment from October 3rd to October 30th, 2021, plotted over the bathymetry contours. Most measurements were made on the pier's south side between -2 and -6 meters in bottom elevation. The bin spacing for this histogram is 13.2-meter bins in the cross-shore direction and 54.3-meter bins in the along-shore direction. The average shoreline over the experiment is shown along with the approximate surf zone edges based on the smallest and largest offshore significant wave height during the experiment.

example of this analysis from Mission 19. In this case, the horizontal velocities are projected into the cross-shore direction, and the vertical acceleration (body frame of reference) is used. These data from all deployed buoys are aggregated and binned into inside and outside the surf zone groups based on the mission's approximate surf zone edge. The cross-shore velocities have been smoothed with a running 1-second mean, and outliers (points greater than 4 standard deviations away from the mean) have been removed. The cut-off location for inside and outside the surf zone was also extended to 1.5 times the approximate surf zone edge. This buffer is added to further separate the types of motion inside and outside the surf zone since intermittent breaking is expected in the outer surf zone, even under the conservative choice of $\gamma_s = 0.35$. In this case, the distribution of horizontal velocities widens and becomes less Gaussian in the tails of the distribution inside the surf zone compared to outside, which could indicate the waves are more asymmetric and could also indicate breaking. The distribution of vertical acceleration also becomes less Gaussian inside the surf zone. There is an excess of low acceleration values, consistent with buoys approaching free-fall during active wave breaking [*Brown et al.*, 2019]. Future work will extend this analysis to investigate the along-shore variability of these types of surface motion under different wave conditions.

The accelerations and rotation rates measured onboard the microSWIFTs can also be used to investigate the forces and accelerations experienced within breaking waves or bores. Breaking waves manifest as short bursts of high-intensity accelerations [*Brown et al.*, 2019; *Sinclair*, 2014]. We can then identify and describe breaking events as peaks in high acceleration variance. An example of the processing used to locate breaking events is shown for Mission 19 in Figure 2.12. First, the mean is removed from the vertical acceleration time series from each buoy (single buoy example, Figure 2.12, panel (a)). The demeaned vertical acceleration is then split into five-second (60 data points) windows, and the variance is computed in each window (Figure 2.12, panel (b)). A threshold of 2.5 times the variance of the entire acceleration time series is used to locate the high-intensity acceleration events or breaking events (Figure 2.12, panel (b)). This threshold has been tuned empirically; in

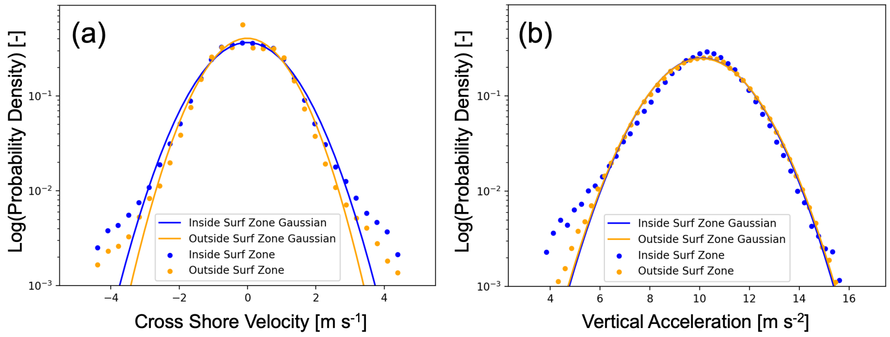

Figure 2.11: Histograms of cross-shore velocity (a) and vertical acceleration (b) from Mission 19. The velocity and acceleration are sorted into inside and outside the surf zone based on the approximate surf zone edge for this mission.

future analysis, it can be verified with images from the tower at the FRF. Using a threshold of 2.5, we find that the majority of breaking events that the microSWIFTs experience are within the surf zone for Mission 19, as expected (Figure 2.12, panel (c)).

If this processing method is extended to the entire dataset, we find that most breaking events are within the approximated surf zone with some intermittent breaking outside the surf zone (Figure 2.13). A total of 3,419 breaking events were detected across the entire dataset. Using the identified breaking events, we can further investigate the statistics of the motion of the buoys during each breaking event, such as the mean and variance of accelerations and velocities during breaking and the spatial patterns of breaking events under different offshore conditions. These estimates of breaking events can be used to answer questions about the spatial variability of the fraction of breaking waves and energy dissipation in breaking waves.

2.5 *Data and Code Availability*

The data from the DUNEX experiment are available at `https://doi.org/10.5061/dryad.hx3ffbgk0` [*Rainville et al.*, 2023b]. The dataset consists of netCDF files for each mission, totaling 67 files after all data processing and cleaning. Each netCDF file contains metadata

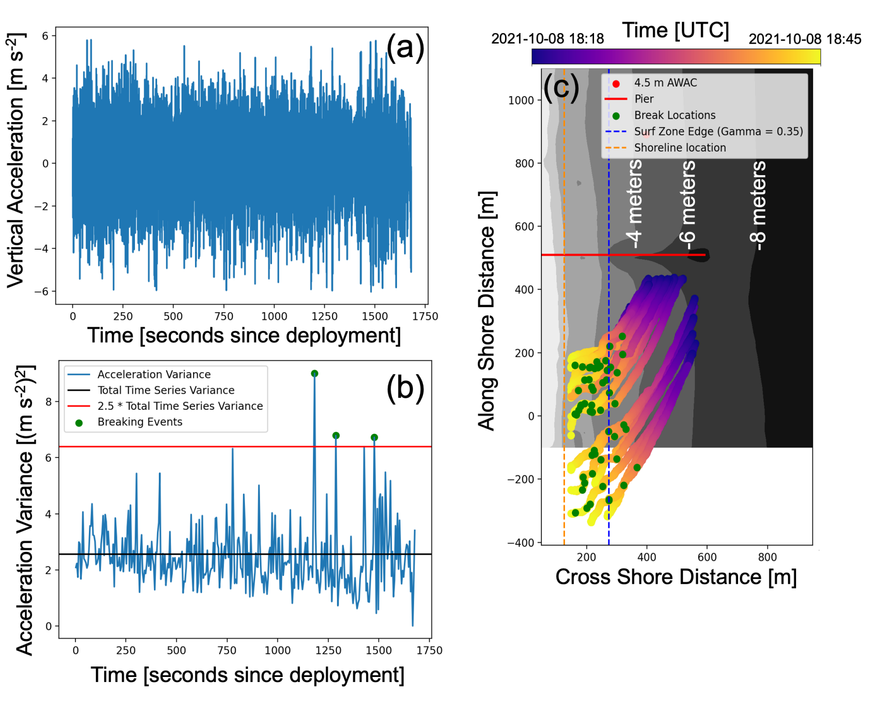

Figure 2.12: Example processing of Mission 19 to locate wave breaking events from high-intensity vertical acceleration peaks. Panel (a) shows an example demeaned vertical acceleration time series. The vertical acceleration time series is split into five-second (60 data point) windows, and variance is computed for each window (b). The variance of the overall vertical acceleration time series and the breaking event threshold (2.5 times the overall vertical acceleration variance) are shown as horizontal lines. The detected breaking events are shown for the example acceleration time series. The spatial location of all detected breaking events is shown along the drift tracks of each microSWIFT for Mission 19 (c).

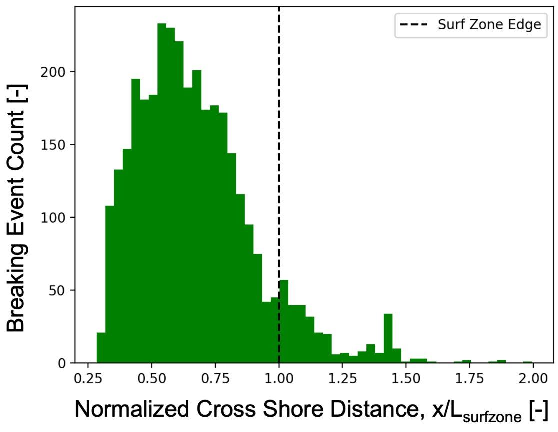

Figure 2.13: Cross-shore variability of detected breaking events across the entire DUNEX experiment. Cross-shore distance is normalized by the approximate surf zone edge of each mission. A total of 3,419 breaking events were detected across the experiment.

on the mission, including the people who worked on the deployments, deployment style, and Level 1 and Level 2 data, along with all associated metadata. The code to process the Level 0 data to Level 1 and 2 data and to build the final dataset is stored in a GitHub repository at `https://github.com/SASlabgroup/DUNEXMainExp`. The code used to analyze the data is also contained in the same repository and can be used as an example code to start future analyses.

2.6 Conclusions

We created a unique dataset of measurements of surface kinematics in the nearshore region by using large, coherent arrays of microSWIFT buoys. The Level 1 data consists of measurements of horizontal velocities and positions in the Earth reference frame, three-axis accelerations, rotation rates, and magnetic heading in the buoys' reference frame. The Level 2 data products consist of three-axis accelerations corrected to the Earth reference frame (NED reference frame) by applying a 9-degrees-of-freedom indirect Kalman filter, followed by band-pass filtering. The other Level 2 data products are vertical velocity and sea surface elevation, computed using the corrected vertical acceleration time series. We evaluated individual microSWIFT buoys by comparing spectral energy density and significant wave height estimates with estimates from nearby fixed acoustic wave and currents sensors and bottom-mounted pressure gauges. We then used a zero crossing algorithm on the sea surface elevation time series from each microSWIFT to extract individual realizations of measured waves in the field. By aggregating the realizations of waves across each microSWIFT on a mission, we estimate the significant wave height and compare that of the nearby acoustic waves and current sensor estimates. The coherent arrays provide high spatial and temporal resolution measurements during each deployment. Over the experiment, we deployed 81 arrays ranging from 2 to 50 microSWIFTs. Post-data cleaning left 67 complete missions across the dataset. These 67 missions resulted in a total of 971 drift tracks. 116,307 wave realizations were measured over the experiment, and 3,419 breaking events were detected. These data will be used to investigate nearshore wave kinematics, transport of buoyant particles, and wave breaking processes in a wave-averaged and wave-by-wave framework.

All authors participated in the data collection, analysis, and writing. Rainville developed the analysis software and prepared the archival dataset. Thomson, Moulton, and Derakhti conceived of the original project and obtained the funding.

The authors declare that they have no conflict of interest.

This work was completed as part of the During Nearshore Event Experiment (DUNEX), which was facilitated by the U.S. Coastal Research Program (USCRP). We thank USCRP for their support of this effort through funding for logistics and coordination (W912HZ-19-2-0045). We would like to thank field engineers Alex de Klerk, Joe Talbert, Emily Iseley, and Nate Clemmet for their efforts in designing, manufacturing, and deploying the microSWIFTs. We also thank Christine Baker, Emma Nuss, Sean McGill, and Jacob Davis for their support in the field. We thank the Town of Duck surf rescue for their help in deploying and retrieving the microSWIFTs throughout the field experiment. We also thank the U.S. Army Engineer Research and Development Center's Field Research Facility for the use of their facility and support staff. We would like to specifically thank Patrick Dickhudt, Mike Forte, Spicer Bak, and many others at the field research facility for all the help they provided in the collection and publication of these data. We thank the reviewers for helping to improve the manuscript and highlight the kinematic measurements.

Chapter 3

SURFING TRANSPORT OF BUOYANT OBJECTS OBSERVED IN THE NEARSHORE

3.1 Introduction

A combination of currents, wind, and waves transports objects on the surface of the ocean, including plastics, search-and-rescue targets, floating organisms, and other marine debris [*Christensen et al.*, 2018]. Surface waves can move these objects through the mechanisms of Stokes drift, wave-driven currents, transient and bathymetric rip currents, and surfing on breaking waves, among others [*Moulton et al.*, 2023b]. The focus of this work is on further understanding of surfing transport and its importance in modifying the trajectory of buoyant objects in the nearshore. Surfing transport will be defined as the process when an object travels near the phase velocity of a wave, similar to a surfer moving with a wave [*Pizzo*, 2017a]. The term object will specifically refer to anything that is not a perfect Lagrangian particle due to its properties, such as size, shape, and buoyancy [*Calvert et al.*, 2021; *DiBenedetto et al.*, 2022].

The effects of wave-breaking-driven transport have been more studied for fluid parcels than for objects. Numerical studies have shown that when deep-water waves start to break, additional transport of fluid particles is observed at the breakpoint, and for a weakly breaking wave within a single wave packet, the breaking-induced transport can be twice that of the mean Stokes drift [*Deike et al.*, 2017b]. Field and laboratory experiments in deep and intermediate water have shown that wave breaking can enhance the average drift by approximately 30% compared to that from Stokes drift alone [*Pizzo et al.*, 2019; *Lenain et al.*, 2019].

In a laboratory setting, objects have been observed to have increased transport due to surfing on breaking waves [*Eeltink et al.*, 2023]. This same study found that including surfing transport as a stochastic process when modeling the 1-D trajectory of buoyant objects improved the accuracy of simulated trajectories for intermediate and deep-water waves in a laboratory scale setting [*Eeltink et al.*, 2023]. While not studied specifically in the surf zone, surfing transport has been noted in surf-zone drifter design techniques, and design considerations to mitigate the effects of surfing are discussed in *Johnson and Pattiaratchi* [2004].

Given that wave breaking is a defining feature of the nearshore, we hypothesize that surfing transport is a significant transport mechanism for buoyant objects in the nearshore and that including it in trajectory models will improve model accuracy. Section 3.2 describes the field measurements and how surfing events are identified in the data, along with characterizing the surfing events, including the location where surfing occurs and the typical size of surfing events. Based on this characterization, a probabilistic surfing transport parameterization is developed and implemented in a simplified trajectory model in Section 3.3. The model results are compared to the true trajectories of drifters, and the model's accuracy is assessed. The impact of this study on beach cleanups, the exchange of plastics and debris between the shore and the open ocean, and how surfing transport can affect different objects is discussed in Section 3.4. Conclusions of this work are then presented in Section 3.5.

3.2 Observations of Surfing Events

3.2.1 Data Collection and Processing

Eeltink et al. [2023] described the motion of surfing transport as a 'jump' where an object rapidly accelerates to near the phase speed of a wave, then decelerates back to an ambient current once it stops surfing. Surfing 'jumps' are observed in the data from microSWIFT drifters (Figure 3.1) deployed in the nearshore as part of the During Nearshore Event Experiment (DUNEX, *Cialone et al.* [2023]; *Rainville et al.* [2023a]).

In October of 2021, free drifting buoys called microSWIFTs (v1), a scaled-down version

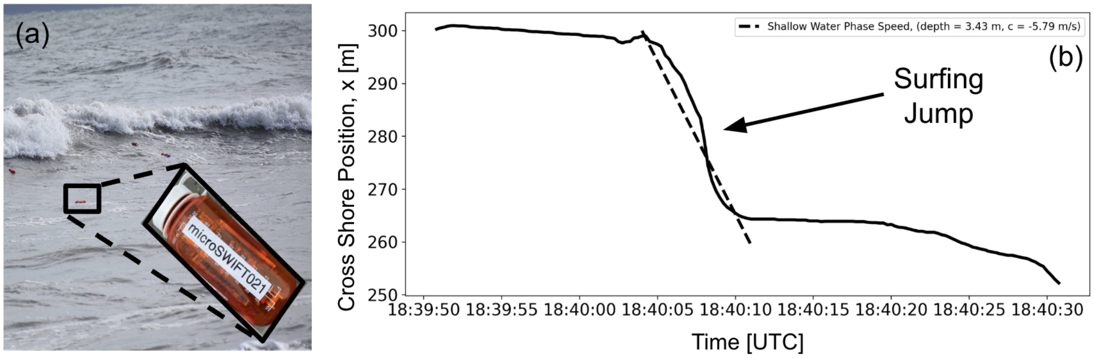

Figure 3.1: (a) Visual observation of microSWIFT buoys about to ‘surf’ on a breaking wave. The v1 microSWIFT buoys are housed in orange Nalgene-brand water bottles. (b) An example of a surfing event is a ‘jump’ in the buoy displacement when the buoy surfs towards the shore. The speed of the jump closely aligns with the linear phase speed of a wave at the appropriate water depth of the jump in this example.

of the Surface Waves Instrumentation Float with Tracking (SWIFT) buoy [*Thomson et al.*, 2023], were deployed in the nearshore to observe the kinematics of the waves as a part of the During Nearshore Events Experiment (DUNEX). The field campaign took place at the US Army Corps of Engineers Field Research Facility (USACE-FRF) in Duck, NC, USA, and a full description of the experiment, microSWIFT design, deployments, and resulting data are in *Rainville et al.* [2023a]. The wave and wind conditions measured while the microSWIFTs were deployed are shown in Table 3.1. Wind measurements are from the end of the FRF pier, and wave measurements are from a pressure gauge array at the 8-meter isobath. The USACE maintains both sets of instruments. Note that the wind and wave directions are both in the nautical direction convention.

Each microSWIFT drifter was equipped with a GNSS receiver that sampled at 4 Hz and an inertial measurement unit (IMU) that sampled at 12 Hz. The inertial measurement unit measures the accelerations, rotation rates, and magnetic heading of the drifters. The

Table 3.1: Wind and wave conditions measured at the USACE-FRF while microSWIFT drifters were deployed.

Parameter	Mean	Range
Wind Speed, u_{wind}	7.5 m/s	1.6 - 13.9 m/s
Wind Direction, θ_{wind}	149.8° CW from North	4.2 - 369.5° CW from North
Significant Wave Height, H_s	1.3 m	0.4 - 2.7 m
Mean Wave Period, T_m	7.8 s	5.3 - 14.5 s
Mean Wave Direction, θ	65.8° CW from North	29.8 - 102.3° CW from North

microSWIFTs were deployed in the nearshore and freely drifted until they reached the beach or were picked up before going offshore. There are 970 distinct drifter deployments after data quality control. These 970 deployments occurred over 66 “missions” where a mission is when multiple drifters are deployed simultaneously under the same wind and wave conditions. The recorded GNSS data was then transformed to a local Cartesian coordinate system with cross and alongshore coordinates, and all dropouts of GPS data (0.04% of all GPS data) were filled with linear interpolations [*Rainville et al.*, 2023a]. During deployments, the microSWIFTs were caught in breaking waves and were observed to surf towards the beach (Figure 3.1).

These surfing events were referred to as “jumps” in *Eeltink et al.* [2023] and will continue to be called that in this work. The jumps are picked out from each drift trajectory and characterized using the following method.

1. The instantaneous cross- and along-shore velocity components are computed as the time derivative of the position time series of each drifter. Instantaneous velocity magnitude is computed from the velocity components.

2. Peaks in the instantaneous velocity magnitude are found using a peak-finding algorithm compared to the linear phase speed, c, at the given location.

3. When a peak is identified that exceeds the linear phase speed (Figure 3.2, Panel (b)), a Gaussian function with an offset (Equation 3.1) is fit to the data in a 71 second (852 points) window surrounding the peak (Figure 3.2, Panel (c)) This window size is derived from the maximum expected surfing duration based on a surf zone width and phase speed estimate.

4. The start and end points of the jump are determined using the "full-width at ten percent of maximum (FWTM)" of the Gaussian function.

During surfing events, the drifters are expected to move at, or greater than, the linear phase speed c. The drifters are surfing on broken waves or bores and in shallow water bore speeds are expected to be aproximately $1.3c$ [*Tissier et al.*, 2011; *Schäffer et al.*, 1993]. For this experiment, the breaking waves are in shallow water. The linear phase speed is then a function of the local depth only and is defined as $c = \sqrt{gd}$ where g is the gravitational acceleration, and d is the local water depth. The linear phase speed, c, is computed along the track using the drifter's measured position, bathymetry, and the local water surface elevation measured by a nearby NOAA water level (tide) gauge. The bathymetry at the site is from surveys conducted at the Field Research Facility using the Lighter Amphibious Resupply Cargo (LARC). The bathymetry is assumed to be alongshore uniform past the northern and southern extents of the measured area. Surfing events are determined as peaks in the instantaneous velocity magnitude of the drifter greater than the linear phase speed. When a peak is found, a Gaussian function with a constant offset is fit to this peak using the function defined in Equation 3.1.

$$f(x) = Ae^{-\frac{(x-\mu)^2}{2\sigma^2}} + B. \tag{3.1}$$

The parameters of the Gaussian are the amplitude (A), the mean (μ), the standard deviation (σ), and a constant offset (B) that represents the background cross-shore drift speed in the fit window. The FWTM is computed as $4.3 * \sigma$ of the fit Gaussian (Figure

3.2, Panel (c)). The start of the jump is defined as half of the FWTM before the velocity peak, and the end of the jump is defined as half of the FWTM after the velocity peak. For a given jump event (J) it can be characterized by the jump amplitude (J_A), which is the distance traveled in the jump, and the jump duration (J_D), the length of time of the jump in seconds (Figure 3.2, Panel (d)). Each jump amplitude consists of a cross and along-shore component, which are denoted as $J_{A,x}$ and $J_{A,y}$, respectively. Additionally, the cross-shore location of a jump (J_x) is defined as the cross-shore position of the drifter at the velocity peak of the jump. The bulk speed of the jumps is then computed as (J_A/J_D). The linear phase speed at the center of the jump (J_c) is also computed from the local depth.

The jump results are explored as both dimensional and normalized (non-dimensional) parameters. The jump duration is normalized by the mean wave period (J_D/T_m), measured by a pressure gauge array at the 8-meter isobath during the deployment (a permanent installation by the USACE-FRF). The jump amplitude is normalized by the wavelength (J_A/λ_0) corresponding to the mean wave period at the 8-meter isobath through the linear dispersion relation. This wavelength (λ_0) is constant during each mission since it is computed at the 8-meter depth where the mean wave period is measured.

3.2.2 Observed Jump Metrics

The jump amplitudes, J_A, vary up to a maximum value of 84.9 meters with a median value of 8.3 meters (Figure 3.3a). The normalized jump amplitude, J_A/λ_0, has a median value of 0.13 (i.e., 13% of a wavelength). The jump duration, J_D, has a maximum value of 42 seconds and a median value of 2.5 seconds (Figure 3.3b). The normalized jump duration, J_D/T_m, has a median value of 0.32, or 32% of a characteristic wave period.

The maximum speed of each jump is near the linear wave phase speed but is generally greater than the linear phase speed (Figure 3.4). The drifters are expected to move with the bores, and in shallow water, bore speeds are expected to be approximately 1.3c [*Tissier et al.*, 2011; *Schäffer et al.*, 1993; *Derakhti et al.*, 2020]. The median value of the normalized maximum jump speed ($J_{s,max}$) is 1.42, which is close to the expected 1.3. The normalized

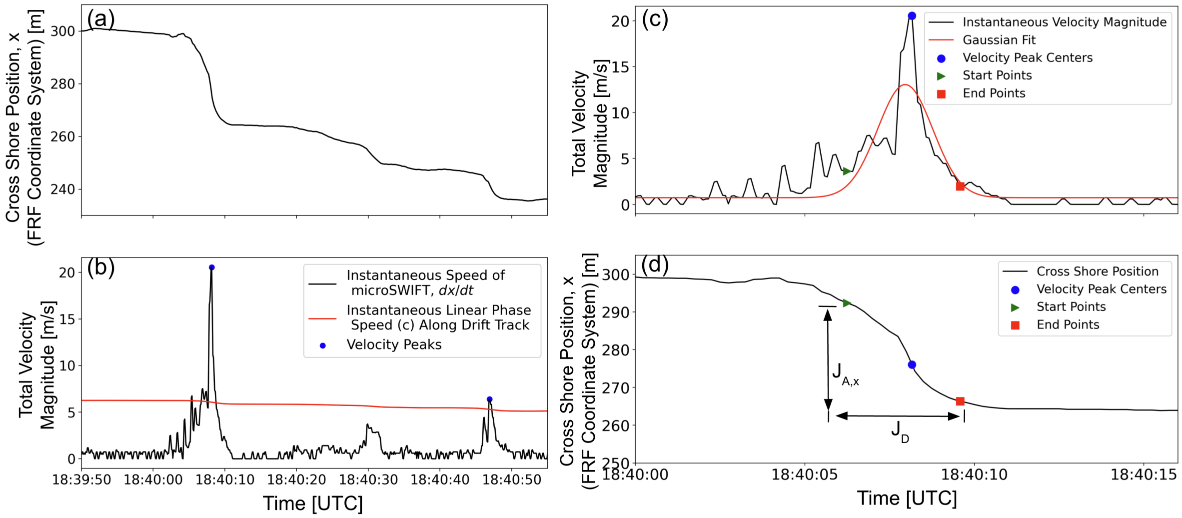

Figure 3.2: Example of processing methods used to extract the jump metrics from the dataset. (a) The cross-shore position of a single microSWIFT drifter and the (b) instantaneous velocity magnitude of the microSWIFT drifter. The linear phase speed is used to pick out the cross-shore velocity peaks. (c) A Gaussian function fit to one of the jumps, the start and end points of the jump are defined at half of the Full Width at Ten Percent Maximum (FWTM) before and after the velocity peak center. (d) The velocity peak, start, and end points with the cross-shore position time series and the resulting cross-shore jump amplitude ($J_{A,x}$) and jump duration (J_D).

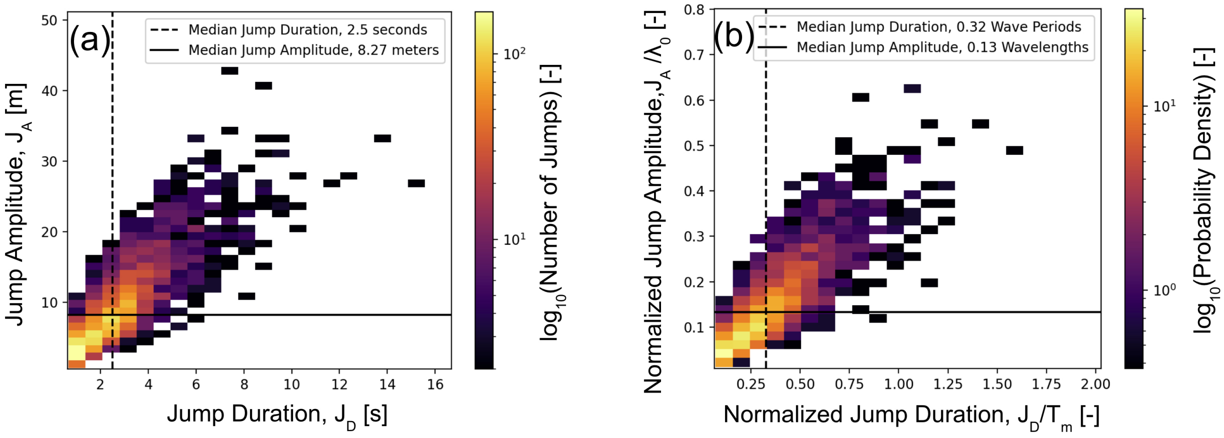

Figure 3.3: Joint Histograms of dimensional (a) and normalized (b) jump amplitudes and durations across all drift trajectories. A total of 3,172 jumps are detected using this choice of speed threshold. Bins with less than two jumps (a) or a probability density of less than 0.25 (b) are omitted.

bulk jump speed ($J_{s,bulk} = \frac{J_A}{J_{DC}}$) is generally slower than the linear phase speed and the expected bore speed. This is most likely due to the acceleration and deceleration periods of the drifters as they start and end surfing events. As a bore interacts with an object, the object will accelerate up to the speed of the bore, travel with the bore, and then stop surfing and decelerate back to the ambient drift speed. These acceleration and deceleration periods of the object will act to bias the bulk speed lower than the speed of the bore the object is surfing on. The median of the normalized bulk jump speed is 0.82, which aligns with the expectation that this value should be biased low compared to the maximum or expected bore speed. Median values are used here to describe the central tendency of the distributions compared to the mean, since both distributions are skewed high (Skewness of $J_{s,max} = 2.3$ and $J_{s,bulk} = 2.6$).

The detected jumps generally occur within the surf zone where wave breaking is the most frequent (Figure 3.5). The offshore edge of the surf zone (X_{sz}) is defined as the cross-shore

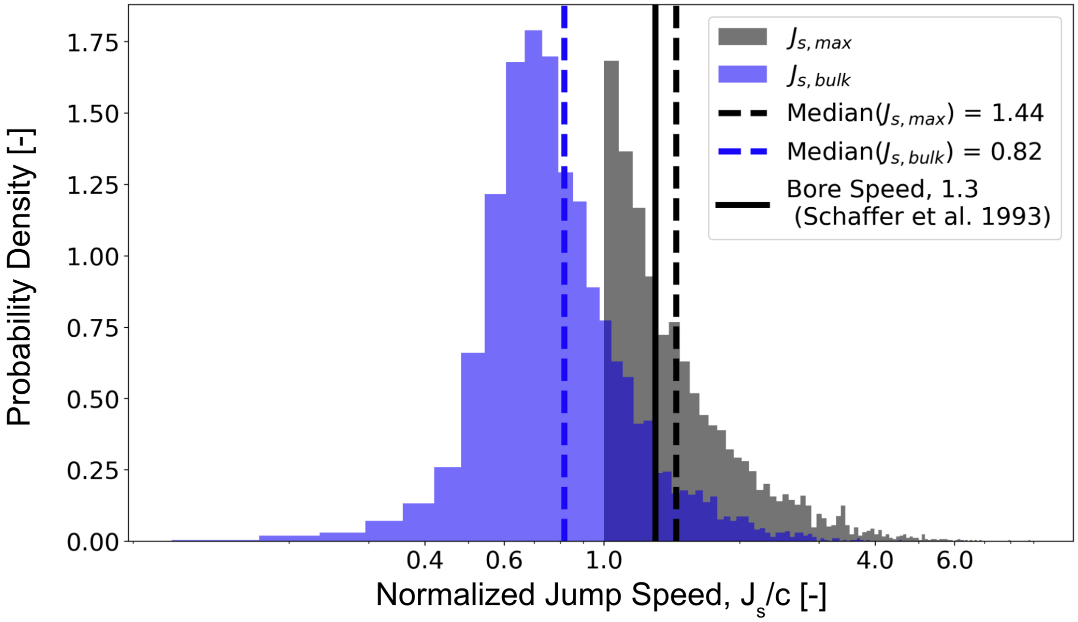

Figure 3.4: Probability density functions for the maximum and bulk jump speeds normalized by the linear phase speed. Median values of both distributions and expected bore speed are shown as vertical lines.

coordinate where $\gamma = \frac{H(x)}{d(x)} = 0.35$. This value is constant for a given mission (set of drifters released simultaneously) but varies between missions as the significant wave height and water depth change. More waves are expected to be breaking in the surf zone than outside, and even more waves are expected to be breaking within the inner surf zone than in the outer surf zone. While waves may be breaking, that does not guarantee that a drifter will surf on the breaking wave; however, the more waves that are breaking and interacting with the drifter, the more likely a drifter is to surf. This dataset does not include much information about the specific waves that the drifters are surfing on, but rather lends itself to a more statistical understanding of the surfing process in the field. Based on the location of detected jump events, a probability of surfing can be estimated for a given cross-shore position, $P\left(surf|\frac{x_i}{X_{sz}} < \frac{J_x}{X_{sz}} \leq \frac{x_{i+1}}{X_{sz}}\right)$ where the index i represents a cross shore distance bin. This probability is computed as the total number of observed jumps in a given cross-shore position bin normalized by the total number of drifters deployed in the same bin (Equation 3.2).

$$P\left(surf|\frac{x_i}{X_{sz}} < \frac{J_x}{X_{sz}} \leq \frac{x_{i+1}}{X_{sz}}\right) = \frac{\text{total jumps measured in bin } i}{\text{total number of drifters deployed in bin } i} \tag{3.2}$$

Since more waves are breaking in the inner surf zone, the probability of surfing should increase towards shore in the surf zone ($x/X_{sz} < 1$) and should decrease asymptotically toward zero offshore ($\lim_{x/X_{sz}\to\infty} P(surf|\frac{x}{X_{sz}}) \to 0$). These expectations align with the data shown in Figure 3.5. Given these expected constraints, a curve can be fit to the data to estimate a continuous representation of the probability of surfing. A sigmoid function (Equation 3.2) has the desired characteristics and can be fit with only two parameters. The two fitting parameters are a horizontal offset, x_0, and a decay rate, k. This function is fit to the data and shown in Figure 3.5.

$$P\left(surf|\frac{x}{X_{sz}}\right) = \frac{1}{1 + e^{\frac{-k}{X_{sz}}(x-x_0)}} \tag{3.3}$$

The largest jump events occur within the inner surf zone (Figure 3.6). Some jumps occur on the outer edge and outside of the surf zone, but these tend to be smaller than

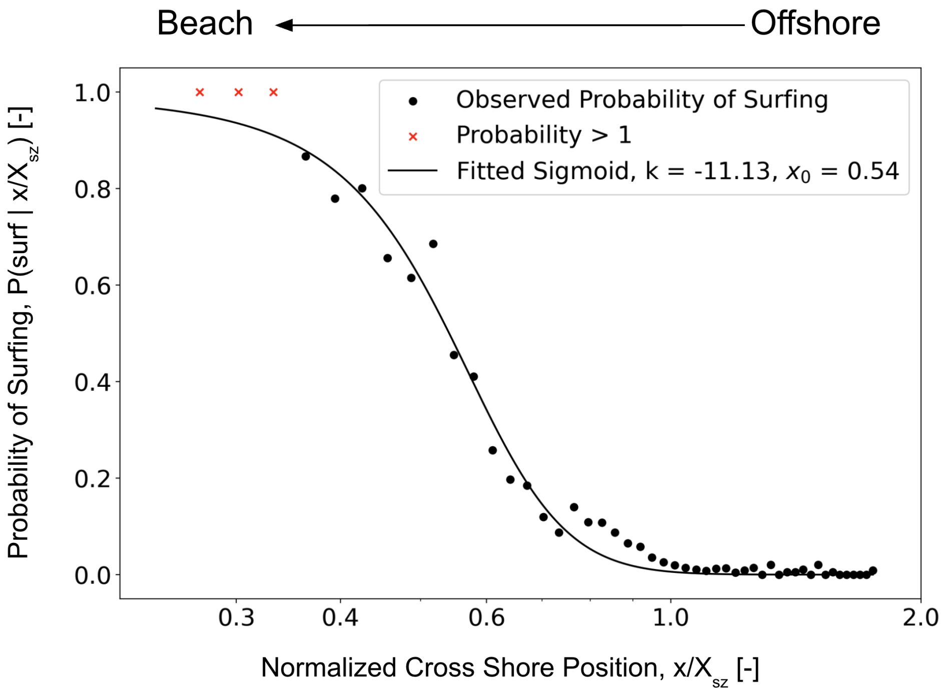

Figure 3.5: Probability of surfing given the cross-shore location of a drifter. A sigmoid function is fit to these data to describe a smooth curve that can be used in trajectory modeling. A value of one on the horizontal axis represents the edge of the surfzone. The markers where probability is greater than one indicate bins where an individual drifters jumped multiple times within the bin. Therefore, the number of jumps in the bin is greater than the number of times it was sampled, and so the value is reduced to a probability of one.

the jumps observed within the inner surf zone. However, this is likely due to a sampling bias, where more drifters are sampled inside the surfzone, and more waves break there. Therefore, it is more likely to observe large jump events in this region that would be larger than the expected value. Larger jumps in the inner surf zone may be due to additional surfing dynamics, such as the stage of bore development when it interacts with the object. However, this cannot be studied given the data collected in this experiment and will be left for future work. Given the data in Figure 3.6, the jump size distributions (both amplitude and duration) do not vary with cross-shore position, and the median value can then describe the overall distribution. The median values are used again because the distributions are skewed high. The combination of these observations of the jump characteristics will be used in the following section to improve the accuracy of modeling the trajectory of these drifters.

3.3 Trajectory Modeling

3.3.1 Surfing Parameterization and Model Setup

Buoyant objects drift with a combination of the wind, waves, and currents depending on the relative strength of each and the properties of the object. *Wagner et al.* [2022] derived a simple model for the motion of a buoyant object from a force balance between quadratic drag laws from the air and ocean sides. We update this model to include a stochastic surfing term as shown in equation 3.4. The components of this model are the Lagrangian ocean velocity ($\vec{u}_{ocean}$), which is composed of the Eulerian currents ($\vec{u}_E$) and Stokes drift ($\vec{u}_S$) ($\vec{u}_{ocean} = \vec{u}_E + \vec{u}_S$) [*Van Den Bremer and Breivik*, 2018], the wind ($\vec{u}_{wind}$), and a stochastic surfing term ($\vec{u}_{surf}$).

$$\vec{u}_{object} = \vec{u}_{ocean} + \epsilon\vec{u}_{wind} + \vec{u}_{surf}, \tag{3.4}$$

The wind speed and direction used in this trajectory model are from measurements taken at the end of the Field Research Facility pier from sensors maintained and operated by the US Army Corps of Engineers. The measurement closest to when a drifter is deployed

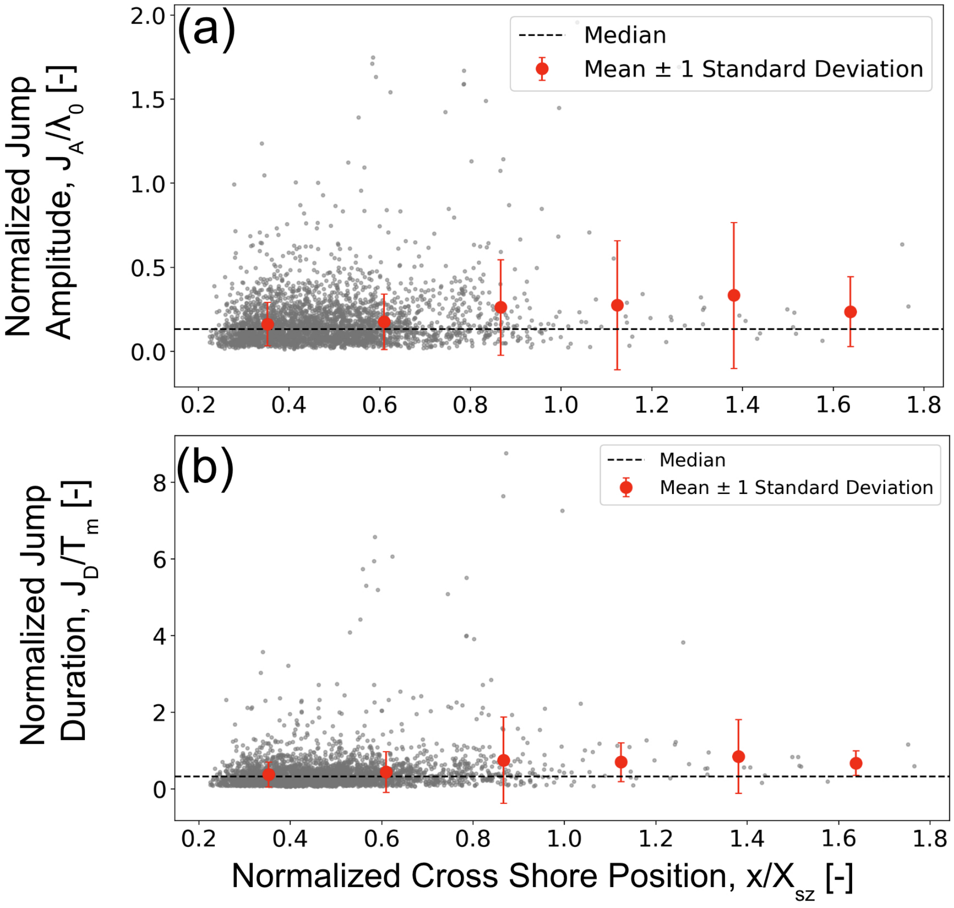

Figure 3.6: Cross shore variation of (a) normalized jump amplitude and (b) normalized jump duration. Observed values are shown as gray points, and values are cross-shore bin averaged with an error bar showing one standard deviation surrounding the mean. The median value across all observations is shown as a horizontal dashed line on both plots.

is used, and the wind is assumed to be uniform over the domain during each trajectory model. The coefficient ϵ is a wind sensitivity factor that combines the drifter's geometry and drag coefficients on the air and waterside. This coefficient accounts for both the transport caused by the direct windage on the object and the wind-driven surface current in the upper few centimeters of the ocean that also acts on the drifters [*Laxague et al.*, 2018]. The v1 microSWIFTs are estimated to have a wind sensitivity factor of approximately 0.03 given their relative density $\rho/\rho_w = 0.68$ and the geometry of the bottle (see analytical estimates of wind sensitivity in Figure 1 of *Wagner et al.* [2022]). This wind sensitivity value is consistent with the empirical rule of thumb that many objects drift at approximately $2\% - 4\%$ of the wind speed and is similar to the version 4 SWIFT buoy (0.01, *Iyer et al.* [2022]) and Sofar's Spotter buoys (0.01, *Houghton et al.* [2021]).

Other studies have combined wind-driven and wave-driven transport and refer to the combined effect as the object's leeway [*Breivik and Allen*, 2008]. These mechanisms are separated here to investigate the relative effects of wind and wave-driven transport following the suggestion in *Christensen et al.* [2018]. The estimates of Eulerian surface currents, Stokes drift, wave refraction, and wave shoaling used in this trajectory model are described in detail in 3.6. The wave measurements, including significant wave height, mean period, and mean direction used to set up this model, are taken from the 8-meter isobath pressure gauge array maintained by the USACE-FRF. The refraction and shoaling of the waves from the 8-meter isobath is estimated using the bathymetry measurements and is described in more detail in 3.6. The effects of wave direction are taken into account in the Stokes drift, alongshore currents estimates, and the surfing jump direction. The role of wave refraction in this model is to adjust the direction of these transport mechanisms. This model does not consider the effects of wave directional spread. The wave parameters are assumed to be constant at the 8-meter isobath for the duration of a mission.

The surfing term, $\vec{u}_{surf}$, is a stochastic term that is included to represent surfing transport. Since wave breaking is a wave-resolved process and individual waves are not resolved in this modeling framework, the process is included probabilistically. The probabilistic process used to represent surfing is described through a flow chart shown in Figure 3.7. The parameterization uses the location of the drifter at the last time step to find the probability of surfing ($P\left(surf|\frac{x}{X_{sz}}\right)$) at that location from the fitted function in Figure 3.5.

A random number generator (RNG) is used to determine if the drifter begins to surf against the probability of surfing value at the given location. If the drifter starts to surf based on the RNG output, it is then moved in the wave direction based on the estimates of wave direction at the given cross-shore location. The drifter is moved at a speed of $0.82c$ to simulate the acceleration and deceleration periods of a jump (based on the values determined in Figure 3.4). The jump duration is randomly sampled from a distribution between $0.026 - 1.33T_m$, which is the range of one standard deviation surrounding the median of the normalized jump duration (based on results in Figure 3.3). The position of each microSWIFT buoy is given by a forward Euler's method integration of equation 3.4. The necessary information to run this model is the drifter's initial position, the wind speed and direction, the offshore wave parameters (significant wave height, mean wave period, and mean wave direction), the water level, and the local bathymetry.

3.3.2 Observed and Modeled microSWIFT Trajectories

The trajectories of each deployed microSWIFT are modeled using the method described in section 3.3.1. Three model versions with increasing complexity are used. The versions are a 'Wind-Only,' 'Wind and Waves,' and 'Wind, Waves, and Surfing.' The 'Wind-Only' model only considers buoy movement due to direct windage on the drifter and the thin upper layer currents driven by the wind, accounted for in the wind sensitivity factor. The 'Wind and Waves' version includes transport driven by windage, wind-driven current in the uppermost layer, the Stokes drift, and an analytic estimate of the along-shore current caused by gradients in the wave radiation stress. The 'Wind, Waves, and Surfing' model includes all of the features above and the surfing parameterization described in Figure 3.7. An example of a true trajectory and the corresponding modeled trajectories is shown in Figure 3.8. In this example and in most cases, the 'Wind, Waves, and Surfing' model performs the best

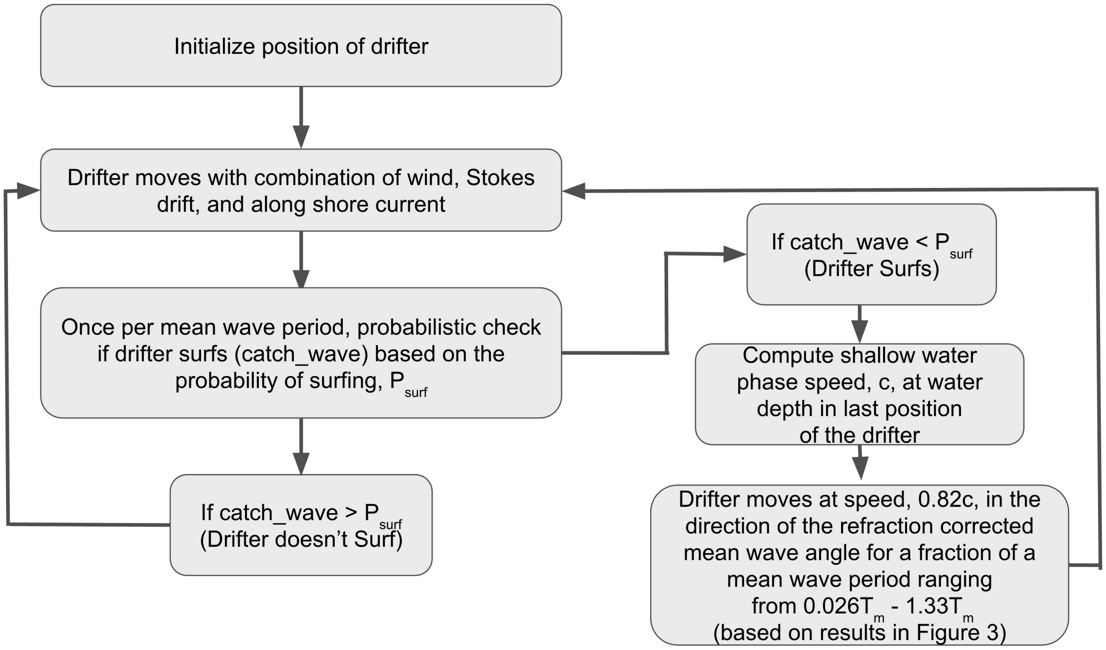

Figure 3.7: Flow chart describing the parameterization used to represent the surfing transport mechanism in the trajectory model. The parameterization is informed by the results for jump sizes from the observations.

Table 3.2: The percent of the total modeled trajectories that reached the same terminal cross-shore position as the observed trajectory of the microSWIFT. This represents the number of modeled trajectories that accurately predicted whether the object beached.

Model Complexity	Percent of Modeled Trajectories Correctly Beached [%]
Wind Only	76
Wind and Waves	84
Wind, Waves, and Surfing	93

in simulating the intermittent surfing behavior of the drifter and its final beaching location. The other models lack sufficient shoreward transport, and thus, those model tracks have a longer time-to-beach, and a larger net alongshore transport occurs before beaching.

Throughout the experiment, most of the deployed microSWIFT buoys beached after deployments. The few that drifted offshore were retrieved by boat or jetski. The subset of drifters that beached after being deployed is used for the following analysis. The skill of each model is first assessed on a binary metric, determining if the modeled trajectory correctly predicts beaching (Table 3.2). As expected, the percentage of beached modeled trajectories increases with increasing inclusion of wave processes (Stokes drift, alongshore currents, and surfing). The results of the percentage of modeled trajectories that correctly beached are shown in Table 3.2. If wind is the only driving force, the modeled trajectories only correctly predict beaching 76% of the time. Including Stokes drift, alongshore currents, and surfing significantly improves this to 93% of the modeled trajectories correctly beaching. These results show that including surfing can substantially improve the accuracy of whether or not the modeled drifters successfully reach the beach.

The modeled trajectories that successfully beach are then further analyzed for accuracy in the alongshore position. The full 'Wind, Waves, and Surfing' model has the smallest errors in alongshore beaching location, $|\Delta y|$ (Figure 3.9), and in time-to-beach, Δt (Figure 3.10). Here, $|\Delta y|$ represents the difference between the modeled and true trajectory beaching

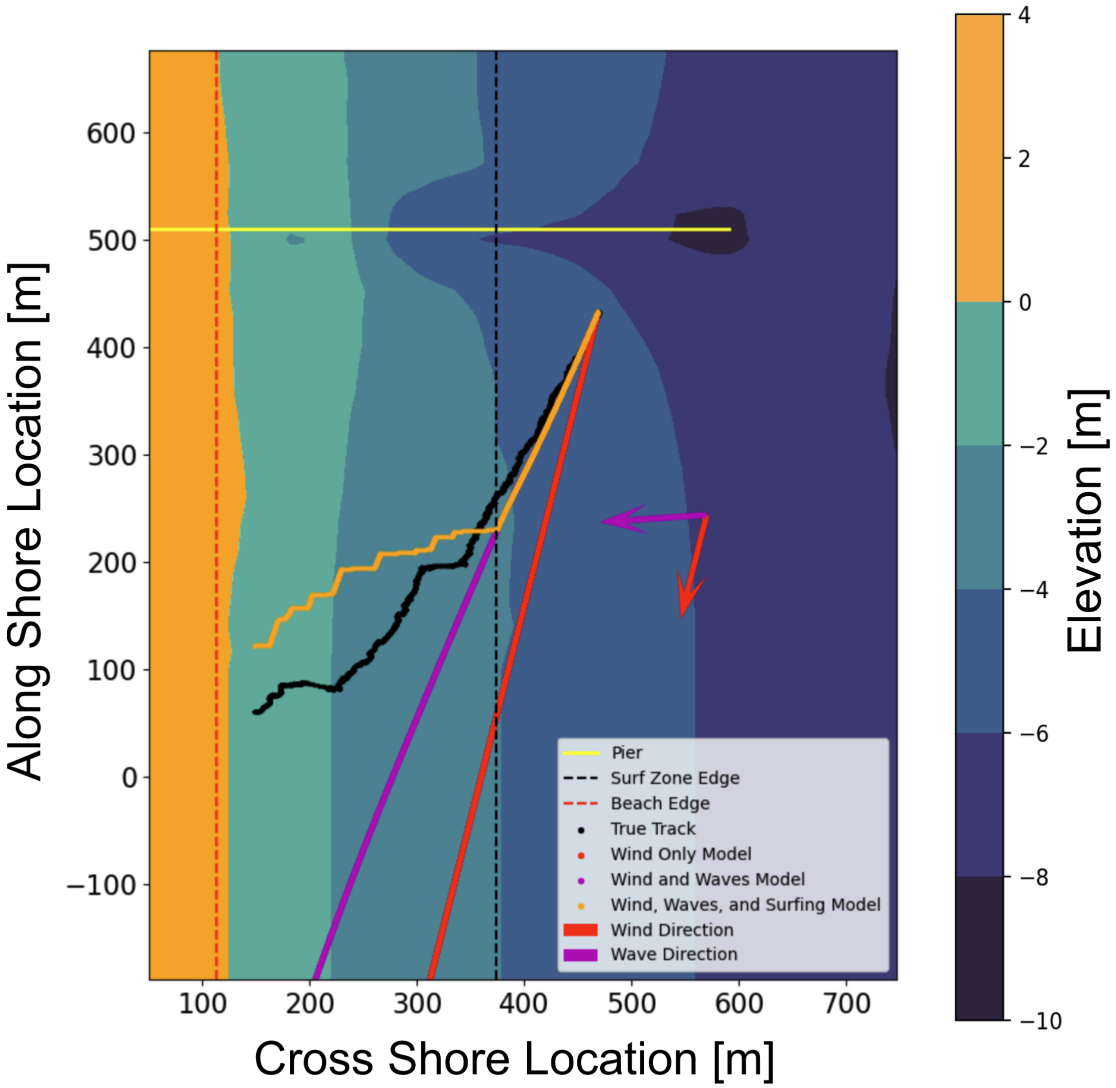

Figure 3.8: Example of a true microSWIFT trajectory with modeled trajectories including ‘Wind-Only,” ‘Wind and Waves,” and ‘Wind, Waves, and Surfing” models (Mission 19, Trajectory Number 9). The background of the image shows the measured bathymetry of the site, and the arrows show the wind and wave directions. These arrows do not represent magnitude, but rather the wave direction measured at the 8-meter isobath and the wind measured at the end of the pier. The bathymetry is extrapolated as constant values for alongshore values less than 100 meters and greater than 1000 meters.

location. The ‘Wind, Waves, and Surfing’ model improves the average accuracy of the alongshore beaching location by approximately 50% compared to both the ‘Wind-Only’ model and the ‘Wind and Waves’ model. When these accuracy values are normalized by the alongshore distance traveled in the true trajectory ($|y_{obs,i} - y_{obs,f}|$, Figure3.9b), it is clear there is a statistically significant improvement in the accuracy of the alongshore beaching location when surfing is included in the modeling.

The temporal accuracy of the models is similarly analyzed using Δt as the difference between the modeled and true time-to-beaching (Figure 3.10). Again the full ‘Wind, Waves, and Surfing’ model has the smallest errors. The accuracy in time-to-beaching, Δt, of the ‘Wind, Waves, and Surfing’ model is improved by approximately 85% compared to the other two models (Figure 3.10). The two models that don’t include surfing severely overestimate the time-to-beaching. This is particularly clear when the difference in time-to-beaching is normalized by the duration of the true trajectory ($|t_{obs,i} - t_{obs,f}|$, Figure 3.10b).

The alongshore beaching location error, $|\Delta y|$, depends on the incident wave angle (Figure 3.11). In this analysis, only the ‘Wind and Waves” and ‘Wind, Waves, and Surfing” models are compared since the ‘Wind-Only” model does not depend on wave angle. For normally incident waves ($\theta < 15^o$), the dimensional errors in both models are small (Figure 3.11a). For oblique waves ($\theta > 15^o$), the dimensional errors in the ‘Wind and Waves” model are significantly greater than the ‘Wind, Waves, and Surfing” model. As the wave obliquity increases, the strength of the alongshore current also increases, and the Stokes drift is directed further alongshore in the wave direction, leading to more significant errors in the beaching location and the time-to-beach. When these accuracy values are normalized by the alongshore distance traveled in the true trajectory (Figure 3.11b), the errors ‘Wind and Waves’ model are much higher than when surfing is included. This is most likely due to the normalization factor being small since when the waves are normally incident, the drifters tend to go straight to the beach. While in the oblique waves case, there is an improvement in alongshore accuracy when surfing is included. For both normally and obliquely incident waves, the alongshore beach location accuracy is improved when surfing is included in the

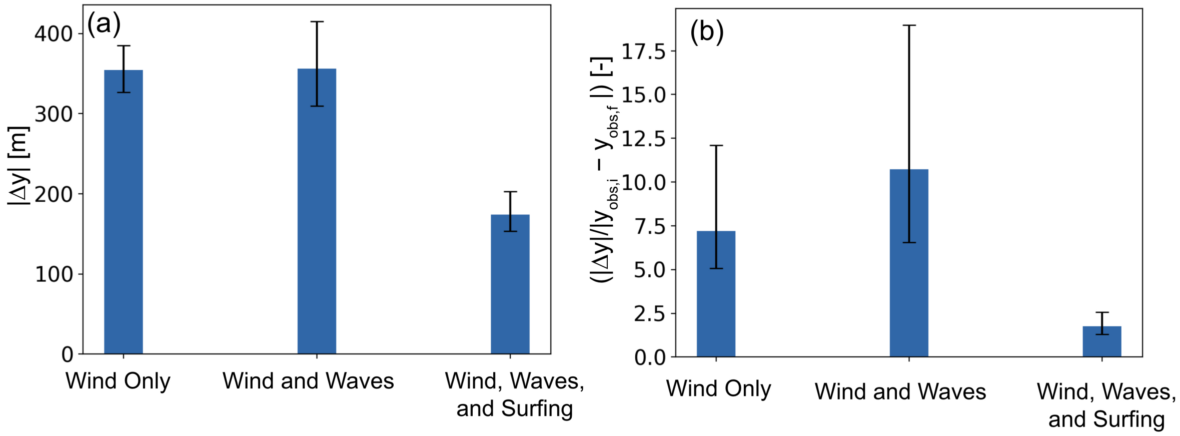

Figure 3.9: The average (a) absolute difference in terminal alongshore position, $|\Delta y|$, and the (b) normalized difference in terminal alongshore position, between the modeled trajectories and the true trajectories. Values are normalized by the total along-shore distance traveled by the true trajectory. The comparison is between the modeled trajectories that successfully reached the beach. Error bars show the 95% confidence interval of the average error computed through bootstrapping of the error population.

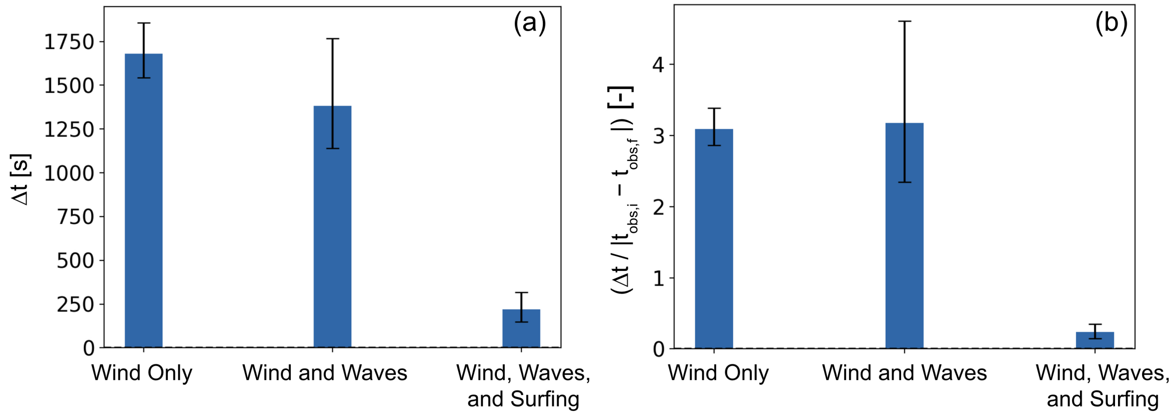

Figure 3.10: The average (a) difference in terminal time, $|\Delta t|$, and the (b) normalized difference in terminal time, between the modeled trajectories and the true trajectories. Values are normalized by the total duration of the true trajectory. The comparison is between the modeled trajectories that successfully reached the beach. Error bars show the 95% confidence interval of the average error computed through bootstrapping of the error population.

modeling.

3.4 Discussion

In this study, surfing transport was observed to push buoyant objects toward the shore near the waterline. The jumps observed have a median amplitude of 8.3 meters and a median duration of 2.5 seconds, and both the amplitude and duration have a large range. Our study did not investigate why a particular object surfs or does not surf, nor why a surfing object may stop surfing while a bore continues to propagate. Factors that may affect the likelihood and duration of object surfing include the random fluctuations in a turbulent bore that could push the object out of the bore and the object's location relative to where the wave starts breaking.

The larger observed jumps tended to occur in the inner surf zone. This is likely due to more sampling within the inner surf zone and more waves breaking in the inner surf zone.

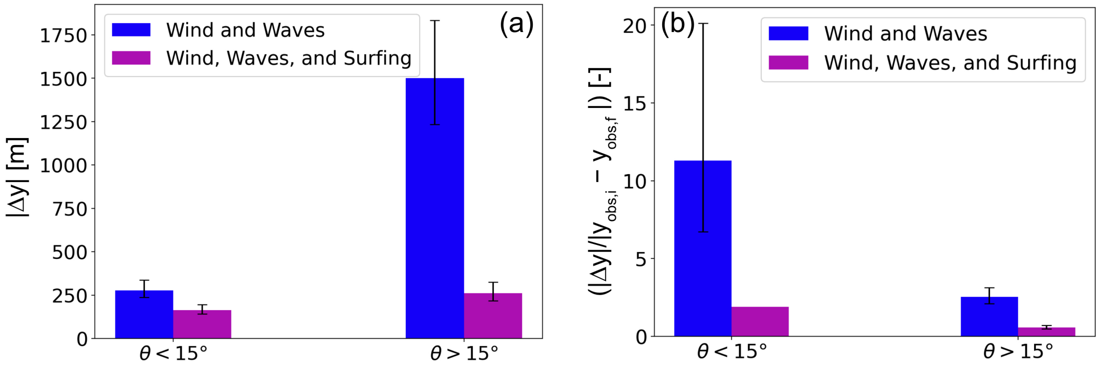

Figure 3.11: The (a) average absolute difference in terminal alongshore position, $|\Delta y|$, between the 'wind and waves' trajectory models and the 'wind, waves, and surfing' trajectory models and (b) the normalized difference in terminal alongshore position as a function of the offshore mean wave angle relative to shore normal. Error bars show the 95% confidence interval of the average error computed through bootstrapping of the error population.

This could also be because the waves have already broken and formed a roller, which may be more conducive to "push" horizontally on drifters, causing them to surf. In contrast, in the outer surf zone, initiation of wave breaking could plunge objects underneath the breaking wave, leading to smaller jumps. Further measurements and analysis are needed to explain the distribution of jump size and duration seen here. The jump sizes observed (Figure 3.3) show that the majority of jumps are O(1-10m), while a few jumps can exceed 50 meters. The distance traveled due to many accumulated small jumps is more important for total transport than the large, less common jumps. Since surfing is a probabilistic process, it must be implemented in deterministic tracking models using a stochastic framework. If this process is to be added to operational trajectory models, it would be best to run the models multiple times and compute an ensemble average to get a likelihood for the position of a drifter.

Buoyant objects that have washed ashore are found on coastlines worldwide. These buoyant objects include plastics, floating organisms (i.e., Sargassum spp.), and marine debris following storms. Beaches worldwide are contaminated with plastics and other debris transported down rivers from inland sources or deposited directly in the ocean. These objects are then transported to beaches where they cause direct harm to the environment as they break down [*Corcoran et al.*, 2009]. Floating organisms, including Sargassum spp., are washing ashore across the Caribbean, West Africa, and China at increased rates, causing direct impacts on the ecosystem (i.e., turtle nesting sites) and economic activity [*Van Tussenbroek et al.*, 2017; *Olguin-Maciel et al.*, 2022; *Smetacek and Zingone*, 2013]. These effects could be mitigated by accurately forecasting algae trajectories and removing the macroalgae further offshore before beaching. Beach cleanups improve the ecological and economic value and aesthetic quality of coastal areas. In the US alone, beaches generate an economic output of \$520 Billion annually, and by eliminating debris on all beaches, this value can be increased by an additional $\$5-84$ Billion per year [*Houston*, 2024]. A modeling study conducted along the east coast of Australia near the Great Barrier Reef (GBR) found that using a numerical model helped determine beaches with the most accumulation of debris so they could be prioritized in beach cleanups [*Critchell et al.*, 2015]. The transport model used in that work did not include surfing transport. Our results suggest that including surfing transport would further improve their predictions. Volunteers generally conduct beach cleanup efforts, and to keep the interest of the volunteers, a sense of accomplishment is needed to make long-term improvements to beach cleaning [*Critchell et al.*, 2015]. Therefore, improving guidance for which beaches to clean based on a data-driven approach could be essential to beach managers in the future.

Surfing transport acts to keep buoyant objects on the beach in the nearshore, in conjunction with swash zone processes not studied here. The process of surfing pushes objects toward shore and can lead to an increased likelihood that they become stranded on the beach; however, little is known of the processes that control beaching for buoyant objects [*Van Sebille et al.*, 2020]. Once objects are in the swash zone, the likelihood of them beaching depends on the wave run-up, backwash strength, and the interaction of those processes with incoming propagating bores and beach steepness [*Davidson et al.*, 2023; *Chardón-Maldonado* *et al.*, 2016].

Surfing transport acts as an impediment to the offshore-directed exchange of buoyant objects by mechanisms such as rip currents and river plumes. This is important to consider when examining the likelihood that land-borne objects (i.e., terrestrially sourced debris or ocean debris previously stranded on the beach) enter the ocean. For example, consider plastics transiting down a river toward the ocean. At the river mouth, if there is consistent breaking, then some buoyant objects will be pushed back to shore and become stranded rather than traveling offshore or along the coast with the river plume. Similar behavior was observed at the Quinault River in Washington State, which found that wave breaking at the river mouth traps drifters and river water in the surf zone rather than them escaping to sea [*Kastner et al.*, 2019]. The relationship between these opposing forces under different conditions will be important for accurate modeling and will most likely depend on the object type. A buoyant object, such as a plastic bottle, may be pushed back to the beach, while a person who is mostly submerged may be more influenced by an offshore-directed current and could be pulled to sea. This reasoning further agrees with field observations from [*Maclean et al.*, 2021], which found that increasing buoyancy led to increased rates of beaching near a river mouth and decreased dispersal distances from the river mouth for buoyant plastics. Similarly, this process may be important for fallen trees transiting down a river and could push them back against the beach, but the mechanisms for driftwood beaching are generally poorly understood [*Murphy et al.*, 2021].

This work describes how surfing transports microSWIFT (v1) drifters, but it does not generalize to how other buoyant objects with different properties will surf. The objects expected in the nearshore range from microplastics and macroplastics, macroalgae, and marine debris following storms to fallen trees, with many other objects within this range. We expect that objects with higher specific gravities are less likely to surf due to their high inertia. We also expect that objects with long characteristic length scales relative to a wavelength will be less likely to surf. Objects with a deeper extent in the water column have also been shown to reduce the effect of surfing [*Johnson and Pattiaratchi*, 2004]. Characterizing how different objects surf will be essential for including this mechanism in future operational models. Object-specific, phase-resolving models may be helpful for understanding which types of objects are likely to surf. As other types of objects are studied, we may be able to determine the probability of surfing, which can be a factor applied on top of the fraction of breaking waves to further modify the model for different objects.

Another application of surfing transport is deep-water wave breaking (i.e., whitecaps). Several studies that have investigated surfing transport in deep water [*Eeltink et al.*, 2023; *Pizzo et al.*, 2019; *Deike et al.*, 2017b]. Further studies are needed to characterize how sensitive buoyant objects are to surf different types of breakers (i.e., plunging, spilling, or surging) and describe how significant deep-water surfing is for different buoyant objects. Buoyant objects in deep water are subject to white-capping over much larger spatial and temporal scales than in the surf zone, and the cumulative effects of surfing in deep water could be significant. The physical process of surfing transport is expected to be similar for both white-capping and depth-limited wave breaking. Therefore, including surfing transport in deep-water for white capping could follow the same approach presented in this study. The fraction of breaking, jump speed, and jump duration would need to be updated to reflect surfing statistics in deep water.

3.5 Conclusions

Surfing events of buoyant objects were observed in the nearshore region using small, free-drifting buoys. Surfing events were identified by fitting a Gaussian function to peaks in the instantaneous cross-shore velocity of each drifter. The Gaussian fit characterizes the size of the surfing events; the jumps have a median jump amplitude of 8.3 meters (13% of a characteristic wavelength) and a median jump duration of 2.5 seconds (32% of a characteristic wave period). Surfing events are shown to have a maximum speed that is near the estimated linear phase speed but is slower, where the median jump speed across all jumps is 82% of the linear phase speed.

The drifters' trajectories are modeled, and a surfing parameterization is added based on the observed surfing event statistics. The modeled trajectories agree more closely with the true trajectories when the surfing parameterization is included. The modeled trajectories that include the surfing parameterization correctly beached in 93% of the cases and, amongst those cases, significantly improved the time-to-beach and beaching location accuracy. The combination of these results suggests that surfing transport is an important transport mechanism for buoyant objects in the surf zone and should be included in trajectory models to improve their accuracy in the future.

3.6 Appendix A: Alongshore Current, Stokes Drift, Refraction, and Shoaling Estimates for Trajectory Model

The Eulerian surface currents, $\vec{u}_E$, are assumed to be primarily alongshore currents driven by radiation stress gradients. Undertow is stronger, lower in the water column, and weak near the surface, and thus not likely to affect buoyant object transport [*Moulton et al.*, 2023b]. Other flows, such as cross-shore rip current jets and associated alongshore feeder currents, may be present where the bathymetry is strongly variable, particularly near the scour under the FRF pier. These will be considered in future work, simulating more complex flow fields. The speed of the alongshore current can be estimated analytically using a momentum balance between wave radiation stress gradients and quadratic bottom stress [*Bowen*, 1969; *Feddersen et al.*, 1998]. The specific analytical expression we will use is derived in *Moulton et al.* [2017] as follows, and is shown to be an effective expression for describing the alongshore currents at the same field site.

$$u_E = \frac{\sqrt{5}}{32} C_D^{-1/2} \alpha^{1/2} \gamma^{3/4} (g H_{br} sin(\theta_{br}))^{1/2}. \tag{3.5}$$

C_D is a bottom drag coefficient (estimated as $C_D = 0.0033$ following *Moulton et al.* [2017]), α is the beach slope at the location of breaking, γ is a breaker index assumed to be 0.35 based on *Raubenheimer et al.* [1996b], H_{br} is the wave height at breaking set by the breaker index γ, and θ_{br} is the wave angle at breaking relative to shore normal. Note that this model does not include any lateral mixing, and therefore, there is a sharp gradient where the current is activated in the model (at the breakpoint). For the purposes of this study, this provides a reasonable longshore current effect, and more accurately, simulating the longshore current profile, including lateral mixing, is left for future work.

The shoaling and refraction of the surface waves are modeled as 1-D processes using the wave measurements made offshore at the 8-meter isobath from an array of pressure sensors (fixed instrumentation maintained by the USACE-FRF), an alongshore averaged profile of the measured bathymetry (Figure 3.12, panel (a)), and measurements of the local water depth from a nearby NOAA tide gauge. A cross-shore profile of the significant wave height (Figure 3.12, panel (b)) is estimated using shoaling and refraction coefficients derived from the conservation of wave energy flux (Equation 3.6), and the cross-shore profile of wave angle relative to shore normal (θ) is estimated (Figure 3.12, panel (b)) using Snell's law (Equation 3.7) [*Svendsen*, 2005]. When the ratio of significant wave height to water depth reaches the breaker index γ, breaking is initiated, and the wave height decreases shoreward as a function of the local water depth only. The wave height at breaking (H_{br}), the wave angle at breaking (θ_{br}), the cross-shore location of breaking, and the beach slope at breaking (α) are estimated from these profiles. Each of these parameters is used to estimate the alongshore current profile that makes up the Eulerian currents in the trajectory model (Eq. 3.5).

$$H_s(x) = H_0 * K_s * K_r = H_0 * \sqrt{\frac{c_{g0}}{c_g(x)}} * \sqrt{\frac{cos(\theta_0)}{cos(\theta(x))}} \tag{3.6}$$

$$\theta(x) = sin^{-1}\left(\frac{c(x) * sin(\theta_0)}{c_0}\right) \tag{3.7}$$

The other component of the Lagrangian currents is the Stokes drift, u_S. This is estimated analytically (Equation 3.8, *Stokes* [1847]; *Kumar et al.* [2017]) and is assumed to be in the wave direction, θ.

$$u_S = \frac{1}{16} H_s^2 \omega k \frac{\cosh(2kh)}{\sinh^2(kh)} \tag{3.8}$$

Here, H_s is the significant wave height, ω is the angular frequency associated with the

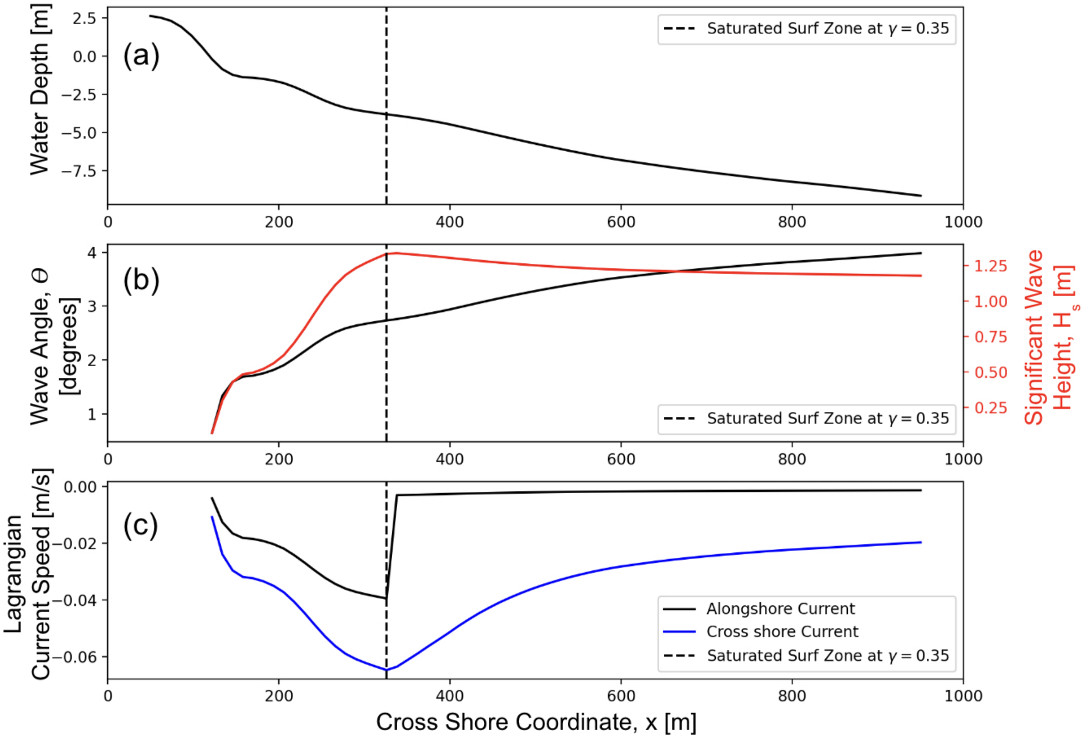

Figure 3.12: Example cross-shore profiles of along-shore averaged (a) bathymetry adjusted with the local water level to water depth, (b) wave angle relative to shore normal and significant wave height estimated from offshore measurements, and (c) profiles of the along and cross-shore current estimated from combined radiation stress driven currents and Stokes drift. Water depth is increasing with more negative values; positive values of wave angle imply waves coming from the north in the local coordinate system, and negative values of current speed imply south-heading current or shoreward-heading current for the alongshore and cross-shore currents, respectively.

mean wave period ($\omega = 2\pi/T_{m0}$), and k is the wavenumber related to the angular frequency through the linear dispersion relation ($\omega^2 = gk \tanh kh$) measured at the 8-meter pressure gauge array. The radiation stress gradient-driven current profile and the Stokes drift profile are combined to create Lagrangian alongshore and cross-shore current profiles (Figure 3.12, panel (c)). Both the Stokes drift and along shore current estimates are made using the significant wave height profile that is shoaled and refracted. As the waves enter the surf zone, the wave height decreases in proportion with γ once waves start breaking. This approach is to avoid double-counting the momentum carried by the waves that contribute to the Stokes drift and also lead to the radiation stress gradients.

Open Research Section

The microSWIFT data used in this study can be found at `https://doi.org/10.5061/dryad.hx3ffbgk0` and can be cited as *Rainville et al.* [2023b]. All code used for analysis is presented and archived in a Zenodo repository `10.5281/zenodo.14736659` and can be cited as *Rainville* [2025]. The contextual and supporting data used in this study was collected by the US Army Corps of Engineers - Field Research Facility and is archived on a THREDDS server and can be found at `https://chldata.erdc.dren.mil/thredds/catalog/frf/catalog.html`. All data and code are open source and freely available to the public.

The authors thank Alex de Klerk, Joe Talbert, and Emily Iseley for their help in designing, manufacturing, and deploying the microSWIFT drifters. We also thank the staff of the USACE-FRF for helping deploy and retrieve the microSWIFT drifters and maintaining the fixed instruments at the field site, which were crucial to this work. We also thank Jake Davis, Malcolm LeClair, and Gaute Hope for their thoughts and discussions on the material presented in this work. Support was provided by the United States Coastal Research Program (grant no. W912HZ-19-2-0045). The authors declare that they have no conflicts of interest regarding this manuscript.

Chapter 4

OPERATIONAL MODELING OF SURFING TRANSPORT FOR BUOYANT OBJECTS IN OPENDRIFT

4.1 Introduction

Marine debris, plastics, and other buoyant objects often wash up on beaches, causing a hazard to beachgoers and coastal ecosystems. It is crucial to understand how macroplastics, a source of microplastics as they break down in the surf zone, and other debris move near the coastlines to launch effective cleanup and mitigation efforts [*Van Sebille et al.*, 2020]. Buoyant objects in the nearshore region move with the wind, waves, and currents [*Wagner et al.*, 2022]. Similar to prior studies in deep water [*Deike et al.*, 2017b; *Eeltink et al.*, 2023; *Pizzo et al.*, 2019], observations from drifting buoys in the surf zone indicate that breaking waves cause enhanced dispersal of buoyant objects [*Rainville et al.*, 2023a]. This transport mechanism is known as surfing transport and has not previously been included in particle tracking models. As surfing is inherently a wave-resolved process, it must be included in wave-averaged operational models as a stochastic process. Surfing events manifest as "jumps" in the position of drifting objects, where an object moves very quickly for a short duration. Small, free-drifting buoys called microSWIFTs were deployed in the nearshore as part of the During Nearshore Events Experiment (DUNEX) in October 2021 in Duck, NC [*Rainville et al.*, 2023a]. Jumps in the position of the microSWIFTs are identified and characterized from the drift trajectories of the buoys, and a surfing parameterization is developed [*Rainville et al.*, 2025]. The parameterization is then implemented in the operational trajectory modeling framework, OpenDrift, which has been applied to model the drift of plastic, oil, biota, search and rescue targets, and other objects [*Dagestad et al.*, 2018].

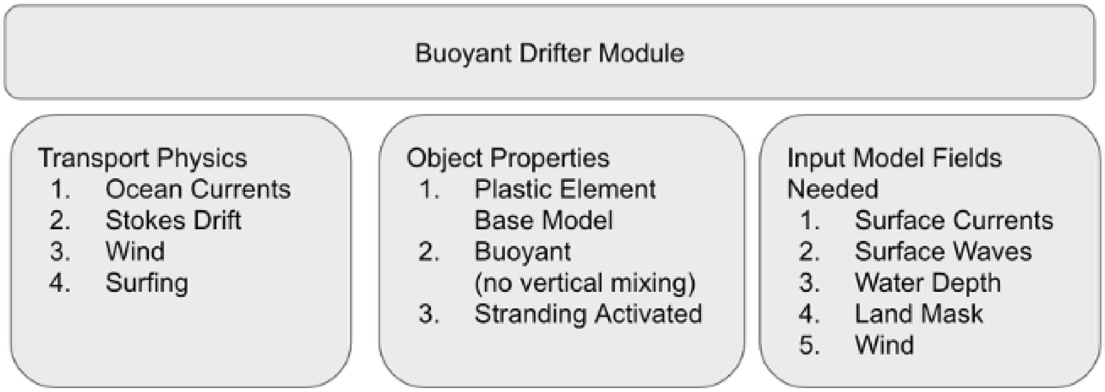

Figure 4.1: Description of the buoyant drifter module within the OpenDrift framework describing the associated transport physics, properties assigned to the drifters, and the input model details.

4.2 Surfing Algorithm Description and Implementation

The OpenDrift trajectory modeling framework is Python-based and is highly adaptable to use in many applications [*Dagestad et al.*, 2018]. The basic structure of the OpenDrift framework is that an object-oriented model reads in forcing data (using Reader functions), and then a drifter object (application-specific) is advected based on a set of methods depending on the object's properties. All drift modules inherit functionality from the BaseModel class that contains basic functions such as element seeding, managing and referencing Readers, and functions to update positions. The application-specific modules are then set apart from the base model by the sets of physics methods applied to the object. Examples of these physics methods include wind-driven transport, Stokes drift, and current-driven transport. The goal of this project is to add an additional physics method to simulate the process of surfing transport for buoyant objects.

A module is developed and described in Figure 4.1 to simulate buoyant drifters transport in the nearshore. The module has the characteristics of only surface-trapped buoyant objects (no vertical mixing), and the physics affecting the drifter are wind drift (with a 3% wind

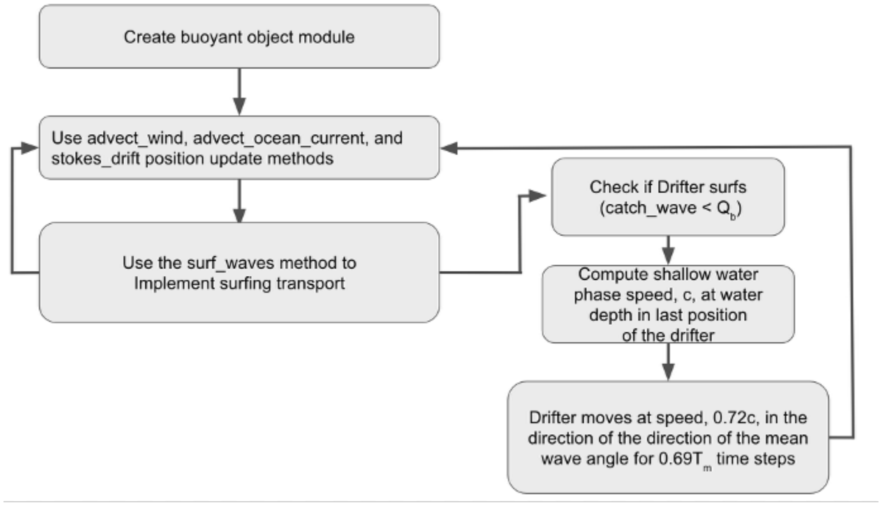

Figure 4.2: Flow chart describing the parameterization used to represent the surfing transport mechanism for the OpenDrift implementation. The parameterization is informed by the results for jump sizes from (Figure is modified from [*Rainville et al.*, 2025]).

sensitivity factor), drift from surface currents, Stokes drift, and surfing transport. The forcing conditions are output from a coupled Regional Ocean Modeling System (ROMS) and Simulating Waves Nearshore (SWAN) model at the field site. The ocean and wave models are two-way coupled through the COAWST modeling framework [*Warner et al.*, 2010].

The surfing parameterization that is added to this module is described in Figure 4.2. The surfing function acts in conjunction with the typical wind-, current-, and Stokes-drift-driven motion. As the object drifts, a boolean value “catch wave” is updated by using a random number generator and comparing that value to the fraction of breaking waves at the current location of the drifter. The fraction of breaking waves is estimated within the OpenDrift model and is a method associated with the BaseModel. If the random number generator produces a value less than the fraction of breaking, the boolean “catch wave” switch is activated, and the drifters jump in the dominant wave direction. The duration of the jump is set to 0.69Tm at a speed of 0.72c where Tm is the energy weight mean wave period, and c is the linear phase speed of the wave. Once the jump is complete, the drifter returns to drifting with the wind, currents, and Stokes drift for a full wave period in which the "catch wave" value is checked again.

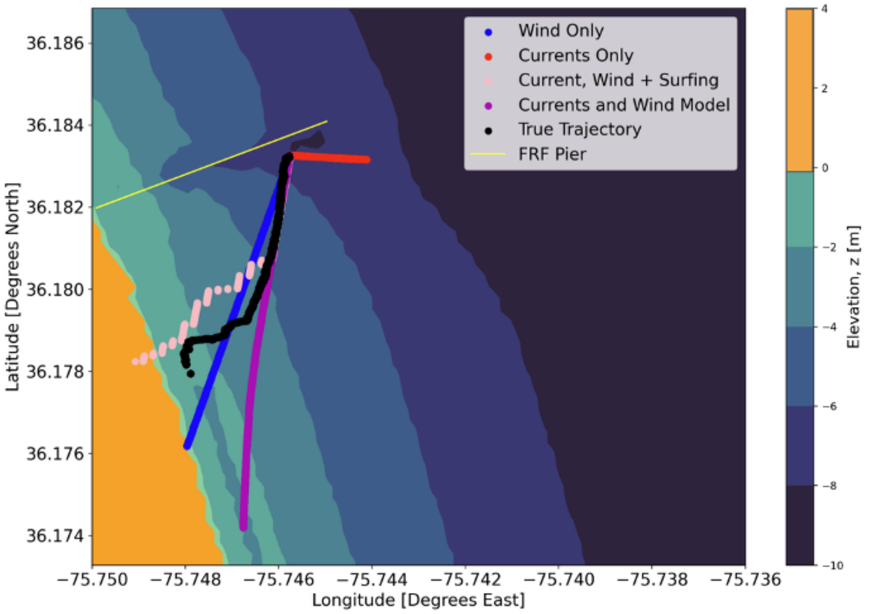

Figure 4.3: Example of a true trajectory of a microSWIFT drifter (black line) being deployed near the 6-meter isobath and drifting towards the beach compared to modeled trajectories from the OpenDrift framework with varying sets of physics applied. All trajectories are overlaid on the measured bathymetry for the field site.

4.3 Results and Discussion

The surfing function is implemented in the OpenDrift model and one of the deployed microSWIFT drifters is simulated using different sets of physics. The sets of physics tested are a wind-only case, currents only, wind and currents, and wind, currents, and surfing. The results of the simulated trajectory and the true observed trajectory of the microSWIFT are shown in Figure 4.3 overlaid on the observed bathymetry. This simulation shows that including surfing transport qualitatively improves the accuracy of the trajectory modeling compared to the other models. The results of *Rainville et al.* [2025] show that including surfing transport in nearshore trajectory models improves the accuracy of the trajectory model with regard to beaching location and time to beaching. This functionality is now added to the OpenDrift framework and can be used for any nearshore drifting applications.

Further work is needed to understand how different objects interact with surfing transport and how surfing transport affects objects in deep water. For now, this parameterization defaults to affect all buoyant objects the same as in shallow water and as if they were microSWIFT drifters. The default values can be updated in the future as the transport mechanism is better understood for different objects and conditions but the implementiation in OpenDrift is flexible for now.

4.4 Conclusions

This study has taken a parameterization for surfing transport developed for small free-drifting buoys and successfully implemented it in an operational trajectory model. Through this implementation, the physics of surfing transport are now available to aid in other applications for studying drift in the nearshore and determining where objects may be stranded. This parameterization is flexible and can be modified by the user. The surfing transport function has been validated for shallow water and nearshore surfing of buoyant objects, but can be expanded to deep-water surfing and other objects as the surfing transport mechanism is further studied.

Chapter 5

WAVE-DRIVEN SURFACE TRANSPORT IN THE MARGINAL ICE ZONE

5.1 Introduction

The sea ice at the poles is melting [*Arias et al.*, 2021; *Meier and Stroeve*, 2022]. In particular, the Beaufort Sea, off the north slope of Alaska, has been a hotspot for melting and change in the Arctic in the past decades [*Stroeve and Notz*, 2018]. Sea ice has been observed to melt earlier in the spring and refreeze later in the fall [*Stroeve and Notz*, 2018]. The large-scale feature of the Beaufort Sea is the Beaufort Gyre, an anticyclonic circulation pattern in the Beaufort Sea driven by the wind [*Timmermans and Toole*, 2023]. As the ice melts, the ocean's surface is opened to the atmosphere, allowing the wind to push directly on the surface. Due to more open water (fetch), surface waves have more space to grow and develop *Thomson and Rogers* [2014]. The impacts of waves on sea ice are that they can drive sea ice transport [*Thomson et al.*, 2021], compact the ice edge [*Sutherland and Dumont*, 2018], mechanically break down the ice [*Ardhuin et al.*, 2020], and break up large floes [*Kohout et al.*, 2014]. Each of these effects is expected to increase as more fetch is opened *Thomson* [2022]. Submesoscale features such as eddies and filaments form in the marginal ice zone, leading to more variability of surface transport [*Manucharyan and Thompson*, 2017]. The combination of these transport processes and the large range of relevant scales makes the marginal ice zone in the Beaufort Sea a highly complex place. The following work seeks to understand the importance of multiple transport mechanisms for driving drift near the ice edge over time scales on the order of hours to days.

5.2 Methods

5.2.1 Salinity and Stratification at the Sea Ice Edge (SASSIE)

The Salinity and Stratification at the Sea Ice Edge (SASSIE) experiment was a field campaign in the Beaufort Sea off Alaska's north slope during the Fall of 2022. The project's primary goal is to understand how ice melts during the Spring in the Western Arctic can lead to changes in the upper ocean structure and how this affects ice formation in the Fall [*Drushka et al.*, 2024]. The experiment included ship-based measurements, deployments of SWIFT drifters, satellite measurements, numerical modeling, and wave glider measurements [*Drushka et al.*, 2024]. The field campaign was organized into "plays," where specific measurements were targeted based on the deployment conditions. The field campaign consisted of five plays. Play One is the focus of this work and includes measurements in the marginal ice zone with deployments of SWIFT drifters [*Thomson*, 2012a] and wave gliders [*Hine et al.*, 2009]. The overview of Play One is shown in Figure 5.1, showing the extent of the ice on the first day and the locations of the SWIFT drifters and the wave gliders throughout the play. Play One lasted approximately two and a half days when all instruments were in the water. This paper aims to explain the motion of the SWIFT drifters and understand the importance of different transport mechanisms.

5.2.2 Temporal Changes during Play One

The wind and wave conditions throughout Play One were non-stationary (Figures 5.2 and 5.3). The winds were high at the start of Play One and decreased throughout the rest of the play (Figure 5.2a), with a maximum speed of 15.4 m/s. The waves were also large early on and decreased throughout the play (Figure 5.3a). Both wind and wave directions varied during the play, with wind coming from the northeast and waves from the southeast. The wind-wave misalignment suggests that the waves are generally swell from a previous storm event versus locally generated waves. The ice pack also changes in time during this play in response to changing conditions.

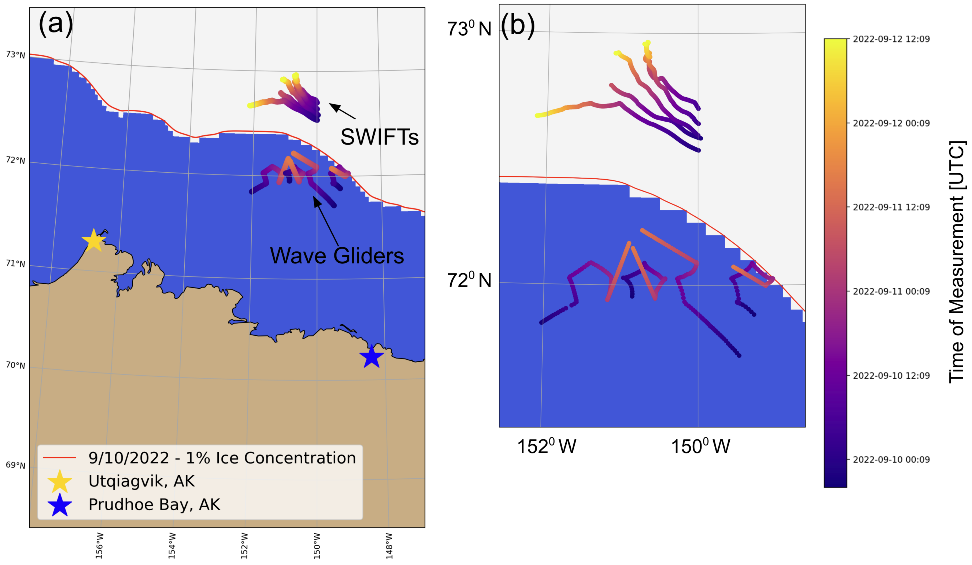

Figure 5.1: Location and time of the SWIFT drifter and wave glider measurements during Play One of the SASSIE field campaign with (a) context of global position near the Alaska North slope and (b) a zoomed-in version to show detail of the trajectories. The color of drift trajectories and wave glider paths represents time. Background colors show the presence of ice (at least 1% concentration) on September 10th, 2022, from gridded sea ice concentration satellite and in situ measurements from the National Weather Service Alaska Sea Ice Program [*Pacini et al.*, 2025].

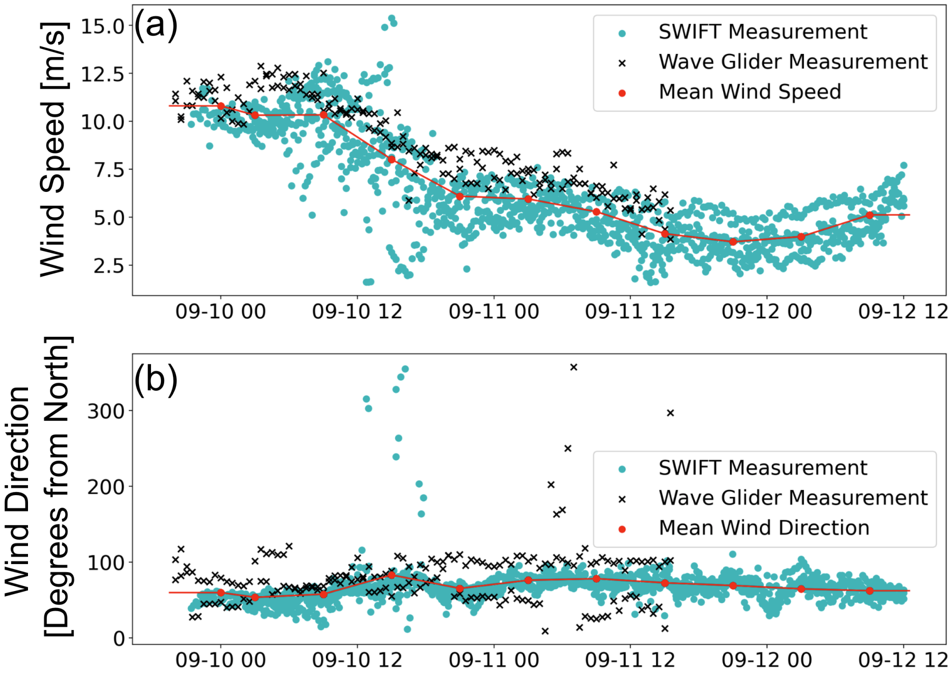

Figure 5.2: (a) Wind speed and (b) direction measured during Play One from both the SWIFT drifters and the wave gliders.

The presence of ice is a dominant feature of the region's dynamics. Therefore, defining an accurate coordinate system that describes whether a drifter is in or out of the ice is crucial. This method will assume that in or out of ice is a binary metric. In reality, ice exists in a spectrum of concentrations, and different ice concentrations should affect the dynamics, such as the attenuation rate [*Thomson*, 2022]. Although this is an effective simplifying assumption, it may lead to some measurement variability. The curvilinear coordinate system represents the ice edge as a single line.

5.3 Drift Dynamics in the Marginal Ice Zone

The SWIFTs are quasi-Lagrangian, driven by wind and ocean motion. The observed drift speeds of all the SWIFTs are shown in Figure 5.4. The dominant features of the observed

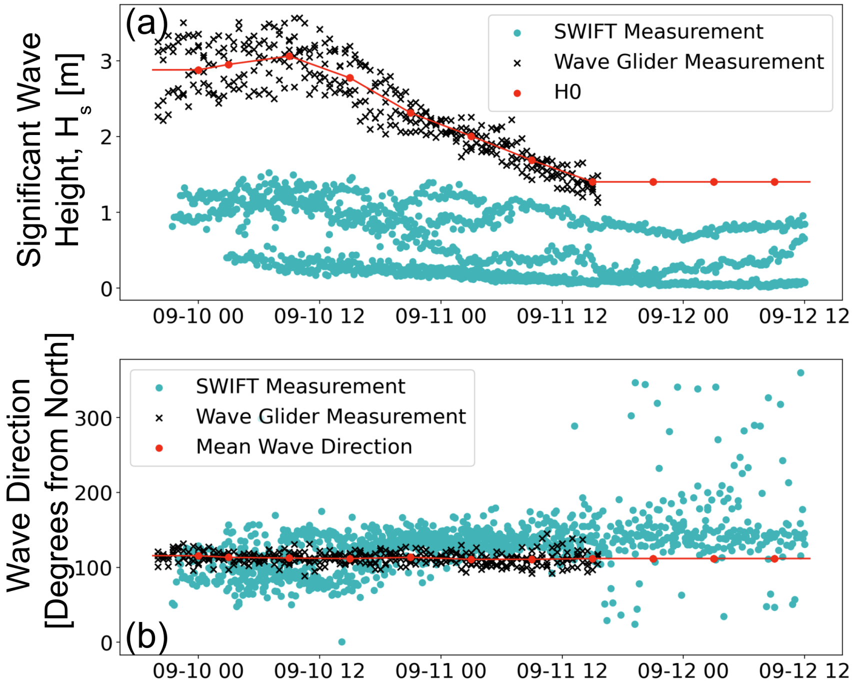

Figure 5.3: (a) Significant wave height and (b) wave direction measured during Play One from both the SWIFT drifters and the wave gliders.

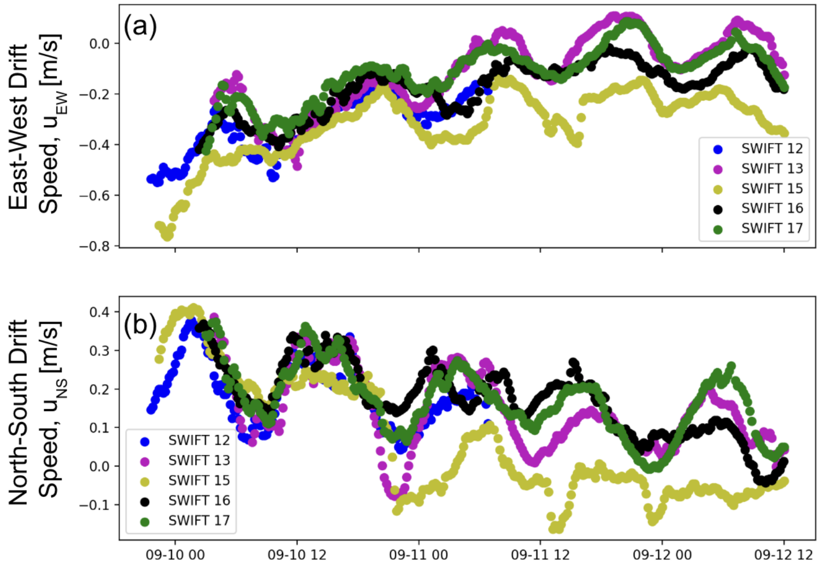

Figure 5.4: (a) East-West and (b) North-South drift speeds measured by the SWIFT drifters. Each point is a 12-minute average of GPS-measured velocity.

drift speeds are that the drifters are moving towards the north-west and have an oscillatory pattern, and the speed experienced between each SWIFT varies. The goal of the following analysis will be to describe the drift velocities observed.

The drift velocity of the SWIFTs is the summation of Lagrangian ocean velocity and the direct windage, where ϵ is a wind sensitivity (Equation 3.4 *Wagner et al.* [2022]). The wind drift factor used here will be $\epsilon = 0.01$ [*Thomson*, 2012b]. The Lagrangian ocean velocity is defined as $\vec{u}_{ocean} = \vec{u}_{Eulerian} + \vec{u}_{Stokes}$. In large-scale motion where the rotation of the Earth becomes important and where vertical mixing is weak, such as the Arctic, the Stokes drift is generally balanced by an Eulerian return current that is equal and opposite to the Stokes drift due to the Stokes-Coriolis force [*Hasselmann et al.*, 1973]. The drifters should then move with the Eulerian currents and the direct windage $\vec{u}_{ocean} = \vec{u}_{Eulerian}$.

$$\vec{v}_{SWIFT} = \epsilon\vec{U}_{10} + \vec{v}_{ocean} \tag{5.1}$$

Each SWIFT drifted $O(\approx\ 50km)$ over Play One (Figure 5.1). The drifters' average latitude is approximately $\phi = 72.75^0N$. Therefore, the Coriolis frequency, defined as, $f = 2\Omega sin(\phi)$, is $f = 1.389 * 10^{-4}Hz$ and the inertial period is $T_f = 12.5$ hours where $\Omega = 2\pi/(24\, hours)$. The average drift speed during the play was 0.28 m/s. These values give a Rossby number of $Ro = \frac{U}{Lf} = 0.04$, which is less than 1 and suggests that the Earth's rotation is important for this process.

The Eulerian currents, $\vec{u}_{ocean} = (u_{EW}, u_{NS})$, will be estimated from linearized momentum balances. The subscripts EW and NS represent East-West and North-South, respectively. The two mechanisms that will be explored in this analysis are wind-driven ($\vec{u}_{ekman}$) and wave-driven transport ($\vec{u}_{rad}$). The velocities due to each forcing mechanism are separate, and the total velocity will be the sum of the two ($\vec{u}_{ocean} = \vec{u}_{rad} + \vec{u}_{ekman} = (u_{rad,EW}\ , u_{rad,NS}) + (u_{ekman,EW}\ , u_{ekman,NS})$) following the methods of *Gill* [2016].

5.4 Wave-Driven Transport

As waves propagate from the open ocean into the ice, they are attenuated, and the momentum that they carry is released [*Thomson et al.*, 2021]. The flux of momentum from the waves is the radiation stress, and gradients in the radiation stress can drive currents [*Longuet-Higgins and STEWARTt*, 1964]. As waves propagate into ice, they attenuate, and a gradient of radiation stress is set up. This process is relevant to the location relative to the edge of the ice pack. Equations 5.2 and 5.3 describe the momentum balances for the wave-driven transport in the cross- and along-ice directions. The subscript n denotes the cross-ice direction, and the along-ice direction is denoted by the subscript ξ.

$$\frac{\partial S_{n\xi}}{\partial n} = \tau_{b,\xi} \tag{5.2}$$

$$\frac{\partial S_{nn}}{\partial n} = \tau_{b,n} \tag{5.3}$$

The left-hand side of these equations denotes the gradient in radiation stress (S), and this is balanced by the bottom drag along the ice on the right-hand side following the results of [*Thomson et al.*, 2021]. The bottom drag in the East-West direction is defined as $\tau_{b,EW} = \frac{1}{2}\rho_w C_{iw}(u_{ocean,EW} - u_{SWIFT,EW})^2$ for the East-West direction and the same for the North-South direction using the North-South wind speed. The speed is simplified to $(u_{ocean,EW} - u_{SWIFT,EW})^2 \approx u^2_{ocean,EW}$. The water density is assumed to be $\rho_w = 1000$ kg/m^3 and the ice-water drag coefficient is $C_{iw} = 0.0055$, which is a community standard value [*Ma et al.*, 2017].

Wave-driven transport is assumed to be steady when wave conditions are stationary. There are also no expected gradients in the along-ice direction ($\frac{\partial}{\partial \xi} = 0$). The solution to this momentum balance (Equation 5.4) comes from [*Thomson et al.*, 2021] and has been shown to accurately describe the along-ice transport of drifting objects in a compact marginal ice zone. Following the same method for the cross-ice direction, the solution is shown in Equation 5.5. The momentum equations and solutions require an ice-edge coordinate system, which will be developed in the following section.

$$u_{\xi,rad} = H_0 e^{-\alpha x}\sqrt{\frac{\alpha g cos(\theta) sin(\theta)}{8C_{iw}}} \tag{5.4}$$

$$u_{n,rad} = \sqrt{\left(\frac{2}{C_{iw}}\frac{1}{16} g H_0^2 \alpha e^{-2\alpha\Delta x} cos^2(\theta)\right)} \tag{5.5}$$

The components of these solutions are the open ocean significant wave height (H_0), the attenuation rate (α), the incident wave angle (θ), gravitational acceleration (g), distance from the ice edge (Δx), and an ice-water drag coefficient (C_{iw}). The remaining parameters are measured and estimated in the following section.

5.4.1 Development of Effective Sea Ice Edge and Ice Edge Coordinate System

The marginal ice zone (MIZ) is generally considered the region between 15% and 80% sea ice concentration [*Dumont*, 2022]. The definition of the ice edge varies among many studies and can be challenging to define, especially since a single ice edge is rare; instead, there is typically a smooth increase in ice concentration the further into the ice pack. In this case, the data is used to define the effective ice edge rather than relying on an arbitrary choice of contour. Existing knowledge of wave attenuation in ice is leveraged to identify the location of the effective ice edge. Waves attenuate as they propagate into sea ice from the open ocean following an exponential decay (Equation 5.6, *Squire et al.* [1995]; *Voermans et al.* [2019]). The attenuation rate depends on frequency [*Wadhams et al.*, 1988], but for simplicity in the following analysis, we use a bulk attenuation rate following the methods of [*Thomson et al.*, 2021].

$$H(x) = H_0 e^{-\alpha(\Delta x)} \tag{5.6}$$

The parameters in this equation are the open ocean significant wave height (H_0, shown in Figure 5.3a), the bulk attenuation rate (α), and the distance from the ice edge (Δx). The distance from the ice edge is defined as $\Delta x = x - x_0$ where x_0 is the location of the effective ice edge and x is the distance of the measurement from the 1% ice concentration contour during the first day of Play One (Shown in Figure 5.1). Since the wave conditions change in time (Figure 5.3), the data is split into stationary time windows. The wave gliders are in the open ocean, and based on the data in Figures 5.2 and 5.3, the stationary time scale is assumed to be six hours. The remaining analysis uses the same six-hour time windows.

The location of each measurement is first transformed into an initial "cross ice" coordinate system where the 1% ice concentration contour from the first day of the play is used (Figure 5.1). The perpendicular distance from the 1% ice concentration contour to each SWIFT location (x) is computed during each six-hour time window. The open ocean significant wave height (H_0) is the average significant wave height measured by the wave gliders during the time window. The open ocean wave height and wave direction are assumed to be constant from the last time window until the end of Play One, since the wave gliders were recovered before the SWIFTs. The wave attenuation model is then fit to each window using a least-squares optimization to find the optimal attenuation rate (α) and ice edge (x_0) (Example in Figure 5.5a).

Solving for the optimal ice edge assumes that the ice edge has the same spatial structure

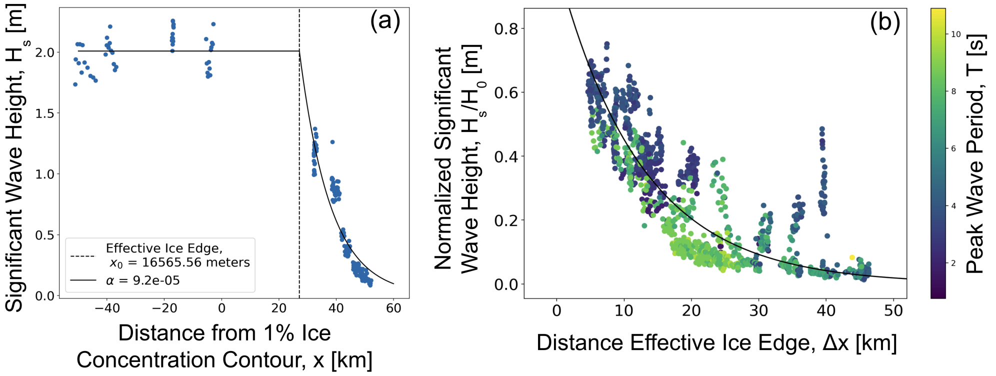

Figure 5.5: (a) Example exponential decay curve fit in a time window between 2022-09-11 00:00:00 - 2022-09-11 06:00:00. Vertical dashed line shows the optimal effective ice edge for this time window. (b) The normalized wave heights from all windows as a function of the distance from the effective ice edge in each time window. Data is colored by the measured peak wave period, showing time when the wave height is larger than the average decay, likely due to locally generated wind waves.

as the 1% ice concentration contour line (Example in Figure 5.5a). This assumption may introduce some variability into the relative ice edge distance (Δx) estimates, but overall, it allows the measurements to be compared. The normalized wave height data then collapse onto an exponential decay curve when the cross ice distance is adjusted for each time window (Figure 5.5b). The average attenuation rate across all time windows is $7.9 * 10^{-5} 1/m$ and is plotted with the normalized wave height measurements. The attenuation rates are well within the range observed in the previous literature [*Wadhams et al.*, 1988].

The average wave attenuation rate model has a coefficient of determination (R^2) of 0.74 and is generally a good model fit, but some variability is not accounted for. The wave height measurements are colored by the peak wave period. Generally, when the normalized wave height exceeds the expected value, the peak period is small, particularly deeper in the ice pack. This is likely due to locally generated waves in open fetch areas within the ice pack that make the significant wave height larger and can explain the variability of the measurements

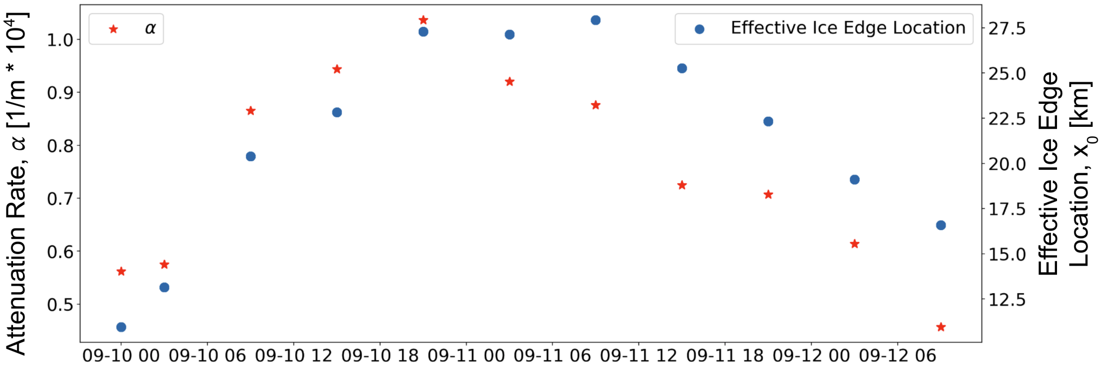

Figure 5.6: Wave height attenuation rate and effective ice edge location in each six-hour time window during Play One.

around the decay model [*Masson and LeBlond*, 1989].

Figure 5.6 shows the attenuation rates and optimal ice edge location from each time window. The ice edge compacted and expanded throughout Play One. The attenuation rate also increased and decreased following the same temporal trend. The attenuation rate should increase as the ice compacts since the waves are moving from open ocean ($H_s = H_0$) to the deeper ice pack ($H_s \to 0$) over a shorter distance.

Identifying the effective ice edge within each time window defines the corresponding ice-edge-aligned coordinate system. The effective ice edge assumes the same spatial structure as the 1% ice concentration contour from the first day (Figure 5.1) and shifts it according to the effective ice edge found in the wave height analysis. The cross-ice direction (n) is normal to the ice edge, with positive being deeper into the ice pack and the along-ice direction (ξ) is tangent to the ice edge everywhere, with positive being towards the northwest.

5.4.2 Estimated Wave-Driven Transport

Once the ice-edge coordinate system is formed, the wave-driven transport can be estimated using the solutions in Equations 5.4 and 5.5 with the measured parameters as a function of

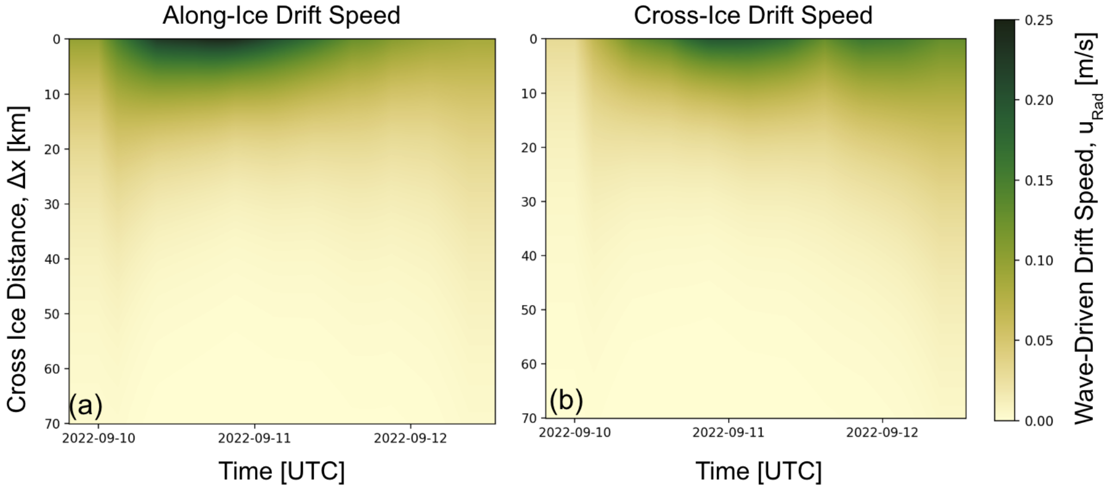

Figure 5.7: (a) Estimated along-ice and (b) cross-ice wave-driven transport speed as a function of cross-ice distance and time based on measured open ocean significant wave height, attenuation rate, and maximum incident wave angle.

cross-ice distance and time (Figure 5.7). The maximum incident wave angle along the ice edge during a time window is assumed to set the along-ice drift speed and is used for the remaining calculations. The wave-driven transport speed for each SWIFT at each time point is calculated by linearly interpolating from the SWIFTs' cross-ice positions and time (Figure 5.8). The estimates for each SWIFT are transformed from the ice-edge coordinate system back to geographic coordinates (East-West and North-South). The SWIFTs that are closest to the ice edge are expected to drift the fastest where the gradients in wave momentum are the strongest.

5.5 Wind-Driven Transport

The momentum balances for wind-driven transport are described in Equations 5.7 and 5.8, and the corresponding Ekman transport solution in Equation 5.9 [*Gill*, 2016]. The solution uses complex notation to combine the coupled equations where i is the imaginary number.

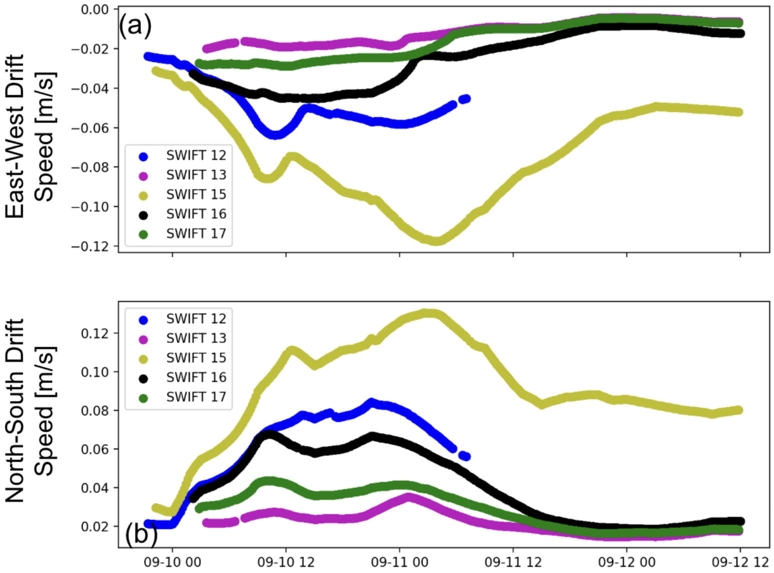

Figure 5.8: (a) East-West and (b) North-South wave-driven transport speeds estimated for each SWIFT given its cross-ice position and time.

The Ekman transport solution includes initial velocity components ($u_{EW,0}$ and $u_{NS,0}$) and an initial time offset (t_0) to account for pre-existing transport. The solution has a steady and time-varying component and depends on the inertial frequency (f), wind stress components ($\vec{\tau_s} = (\tau_{s,EW}, \tau_{s,NS})$), mixed layer depth ($h$), and water density ($\rho$). The wind stress is defined as $\tau_{s,EW} = \frac{1}{2}\rho_a C_{ai}(U_{10,EW} - u_{EW})^2$ for the East-West direction and the same for the North-South direction using the North-South wind speed. The wind speed is assumed to be much greater than the speed of the SWIFT, and this simplifies $(U_{10,EW} - u_{EW})^2 \approx U_{10,EW}^2$. The air density is assumed to be $\rho_a = 1.25\ kg/m^3$ and the air-ice drag coefficient is $C_{ai} = 0.00125$ [*Thomson et al.*, 2021]. The solution is then fit to the data using a nonlinear least squares regression to solve for the optimal initial velocity components, time offset, and the mixed layer depth.

$$\rho_w h(\frac{\partial u_{EW}}{\partial t} - f u_{NS}) = \tau_{s,EW} \tag{5.7}$$

$$\rho_w h(\frac{\partial u_{NS}}{\partial t} + f u_{EW}) = \tau_{s,NS} \tag{5.8}$$

$$u_{EW,Ekman} + i u_{NS,Ekman} = \frac{-i(\tau_{s,EW} + i\tau_{s,NS})}{\rho f h} + (u_{EW,0} + i u_{NS,0} + \frac{i(\tau_{s,EW} + i\tau_{s,NS})}{\rho f h}) e^{-if(t-t_0)} \tag{5.9}$$

The curve fit is applied to the East-West drift speed residual when the estimated radiation stress gradient-driven currents and the direct windage are subtracted ($u_{ekman} = u_{SWIFT} - u_{windage} - u_{rad}$). The optimal parameters solved for in this curve fitting are the initial velocity components $u_{EW,0} = 0.0017$ m/s and $u_{NS,0} = 0.17$ m/s, the initial time offset $t_0 = -5553$ seconds, and the mixed layer depth of $h = 1.9$ meters. The mixed layer depth solved for here is very shallow and may not be completely representative of the true mixed layer depth. However, the mixed layer depth in the marginal ice zone is generally shallow [*Jackson et al.*, 2012] with an average summer depth of 16 meters and 24 meters in winter [*Toole et al.*, 2010]. This shallow mixed layer depth is generally due to cold fresh water from ice melt sitting on the surface above the warmer salty water trapped below. Figure 5.9) shows the Ekman transport model for these data.

5.6 Results

The drift speeds observed by the SWIFTs are well accounted for by the wave-driven and wind-driven transport mechanisms in both the East-West and North-South directions (Figure 5.10). The residuals between the observed drift speed and the model are computed for each measurement in both the East-West and North-South directions (Figure 5.11). A perfect fit for the models would suggest residuals of zero. The average East-West drift speed residual is -0.066 m/s, and the average North-South drift speed residual is -0.079 m/s, both near zero. The distribution's residuals are near normal, but are both skewed negative (EW Skewness =

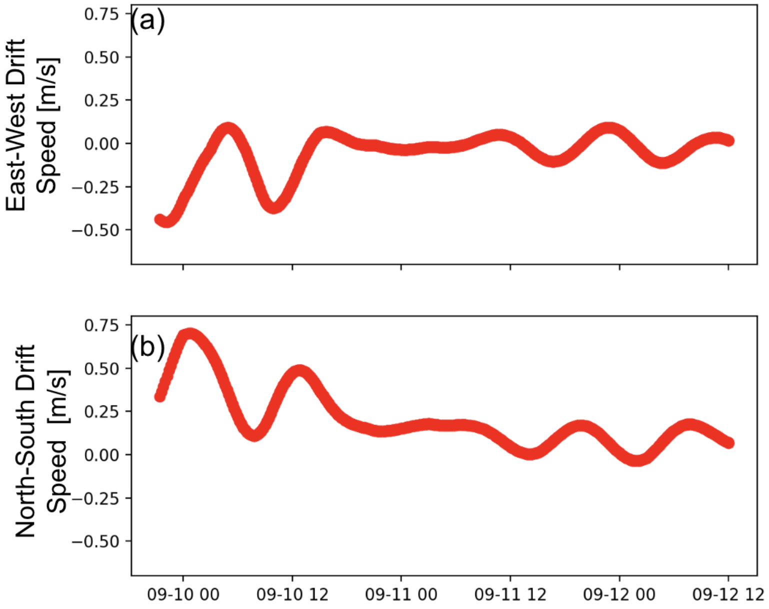

Figure 5.9: (a) East-West and (b) North-South Ekman transport solution fit to the data.

-0.103 and NS Skewness = -0.177), suggesting that the model is predicting more south-west drift than was actually observed. Each observed drift speed is an average of GPS-measured velocities over a 12-minute period. The standard deviation of these measurements in a 12-minute period is also computed. This metric represents the uncertainty in the drift speed observations. The average drift speed standard deviation is 0.15 m/s across all measurements. which may further suggest that the residuals computed here fall within the uncertainty of the observations and the model describes these data well.

Early in the play, the drift speed is the highest when the waves are large and the wind is strong. In this case, the windage, radiation stress, and Ekman transport are of similar magnitudes, and as the play progresses, the radiation stress and windage become dominant terms compared to the Ekman transport. As the SWIFTs drift deeper into the ice pack, the radiation stress gradient-driven currents diminish, and the open ocean wave height decreases later in the play; therefore, this mechanism is expected to become smaller.

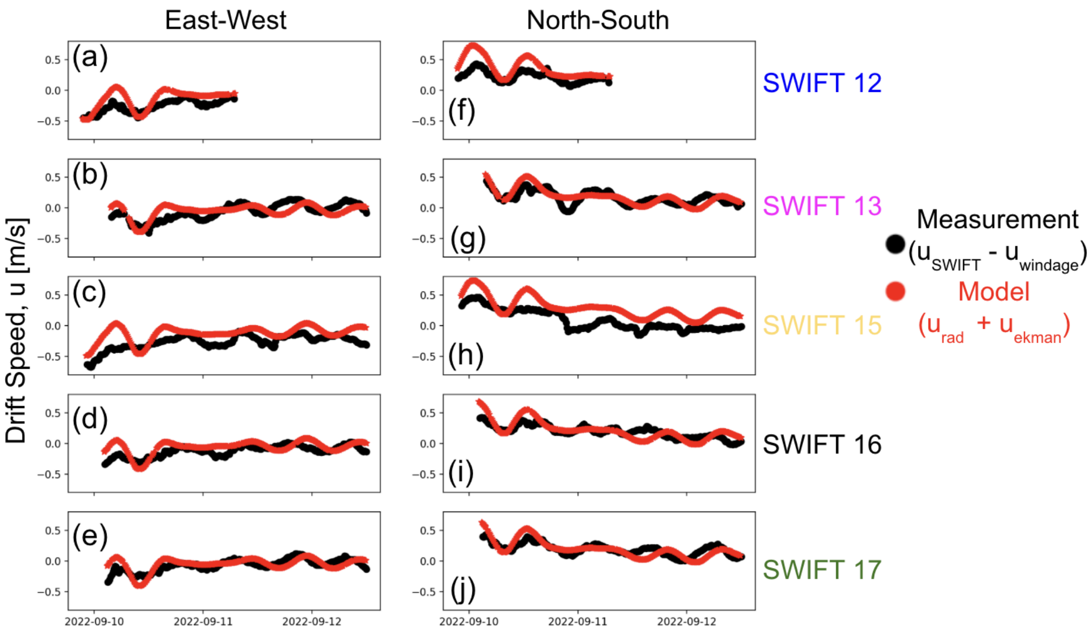

Figure 5.10: Time series of the observed (a-e) East-West and (f-j) North-South drift speed ($u_{SWIFT} - u_{windage}$) and model ($u_{rad} + u_{ekman}$) for each SWIFT.

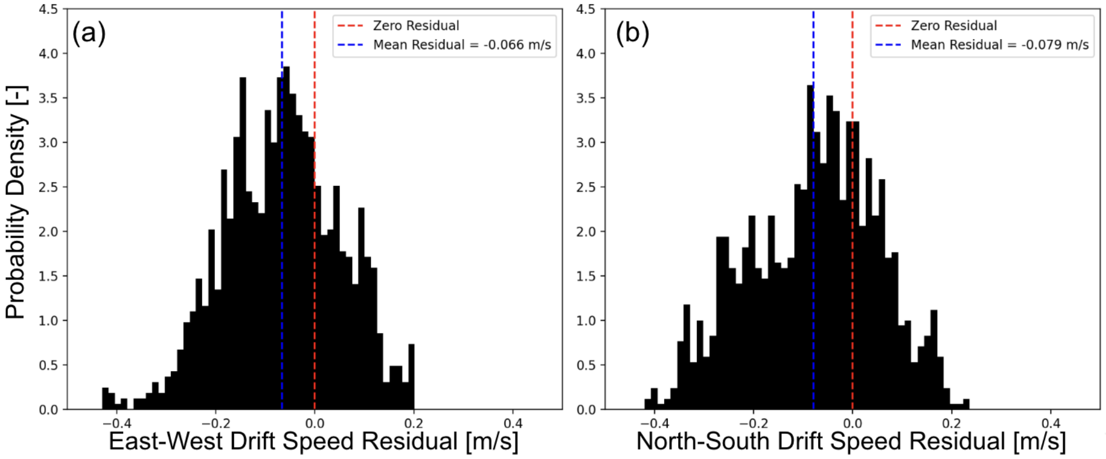

Figure 5.11: Normalized histograms of the (a) East-West and (b) North-South drift speed residuals ($u_{SWIFT} - u_{rad} - u_{windage} - u_{ekman}$).

5.7 Discussion

The marginal ice zone is a highly dynamic region, and the importance of the combination of driving mechanisms makes the area challenging to predict in the short term [*Dumont*, 2022]. The summation of transport mechanisms accurately describes the drift speeds observed by the SWIFTs. A combination of measurement uncertainty and the exclusion of additional transport mechanisms likely accounts for the remaining residuals in the drift speeds. The model did not include the effects of submesoscale eddies, which are essential for transport near the ice edge [*Manucharyan and Thompson*, 2017], nor does it include the impact of ice concentration, type, or age, which could modify the hydrodynamics [*Dumont*, 2022]. These transport mechanisms have implications for the compaction of the ice edge and the mixing of water masses in the marginal ice zone. The near-surface water in the marginal ice zone, particularly in summer and fall, is fresh and cold with a layer of warm, salty water subducted underneath [*MacKinnon et al.*, 2021]. If the deeper, warmer water is mixed up to the surface, more energy will be required to be removed to refreeze the surface water and form ice. This could further lead to a reduction in sea ice as the air temperatures are not low enough to remove even more heat from the ocean. The wave-driven transport can act to drive currents into the ice, as we saw, which could help to deepen the cold, fresh layer under the ice and further reduce the upward mixing. If the ice melts completely and this mechanism is removed, there could be a further positive feedback that reduces the formation of sea ice. This mechanism is speculative and will require further investigation in future work.

5.8 Conclusions

The drift speeds of SWIFT drifters deployed in the Beaufort Sea marginal ice zone are estimated using a summation of wind and wave-driven transport mechanism models. Transport mechanisms are estimated from wind and wave measurements collected during the experiment. The combined model effectively explains the observed drift speeds accurately. The residuals between the observations and the model estimates of East-West and North-South drift speed are centered near zero with a near-normal distribution, suggesting the model explains the data well. The transport mechanisms considered are direct windage, Ekman transport with inertial oscillations, and transport due to radiation stress gradients. The wave-driven transport is a dominant term closest to the ice edge, where the gradients in radiation stress are the strongest.

Chapter 6

CONCLUSIONS

6.1 Summary

This dissertation presents advancements in technology and science that aim to improve our understanding of wave-driven transport of buoyant objects in the ocean.

Chapter 2 focuses on developing the microSWIFT drifter and its utility in measuring the surf zone as part of the During Nearshore Events Experiment (DUNEX). The microSWIFT has since gone through many reiterations and been used in many other projects [*Thomson et al.*, 2024; *Cavaleri et al.*, 2024]. The main result of this work was the production of a surf zone surface kinematics dataset using coherent arrays. The microSWIFTs measured their global position, drift speed, acceleration, rotation rate, and magnetic heading. They were durable and were effectively deployed and retrieved in the surf zone. This dataset is public and can be used in the future to study surf zone kinematics and transport.

Chapters 3 and 4 focus on understanding surfing transport. Surfing transport is a wave-driven transport mechanism that enhances object velocities significantly for a short time. This was defined as a “jump” in the position of a drifter. In Chapter 3, surfing jump characteristics are extracted from trajectories of deployed microSWIFT drifters using the dataset collected in Chapter 2. A probability of surfing is computed based on the locations of surfing events in the cross-shore. A stochastic model is then developed to implement surfing transport into a simple trajectory model. Implementing the surfing model significantly improves the accuracy of beaching locations and time-to-beaching over models that do not include surfing. Following these methods, a stochastic surfing model is implemented as a function in the operational trajectory model OpenDrift.

Chapter 5 then moves from the small microSWIFTs and small-scale transport in the surf zone to larger-scale transport in the Arctic. This chapter focused on characterizing the drift of SWIFT buoys in the Beaufort Sea marginal ice zone. Surface waves generated in the open ocean propagate towards the ice carrying energy and momentum. These waves are attenuated in the ice, which sets up a momentum flux gradient, further known as a radiation stress gradient, into the ice. The radiation stress gradient drives an Eulerian current along the ice's edge and can lead to the compaction of the ice. The radiation stress gradient-driven currents are found to be a dominant transport term at the ice edge. Ekman transport, Stokes drift, and direct windage also contribute to the total drift. The effect of each of these mechanisms is estimated from measured forcing conditions and is found to explain the drift speeds accurately.

6.2 Broader Impacts

There is a lot of plastic in the oceans [*Van Sebille et al.*, 2020], and the sea ice in the Arctic is melting [*Arias et al.*, 2021]. These are problems caused by humans [*Arias et al.*, 2021], and we should work to fix these problems. Part of fixing these problems is understanding where these objects will go as they drift on the ocean's surface. I hope this work will contribute to the conversation and improve our understanding of how drifting objects move and the importance of considering the effects of surface waves. An improved understanding of drifting object trajectories can help to inform the cleanup and reduction of plastics in the ocean [*Van Sebille et al.*, 2020]. Knowing how ice will move is important for understanding how ecosystems will be affected [*Post et al.*, 2013] and how the polar regions are expected to change in the future [*Stroeve and Notz*, 2018]. To predict where plastics and sea ice will move, the trajectories of the drifting objects must be modeled and forecasted. The models must be validated against observations to understand their accuracy.

From NOAA's *2016 Report on Modeling Oceanic Transport of Floating Marine Debris*, one of the recommendations made to researchers is to “ investigate nearshore and surf-zone dynamics of debris movement, deposition, and refloating [which] also could help to inform marine debris models [*NOAA*, 2016].” Yet little is known about the processes that move plastics and buoyant objects towards the beach and cause them to become stranded [*Van Sebille et al.*, 2020]. Also, many plastics discarded and assumed in the ocean are not accounted for [*Sutherland et al.*, 2023]. Surfing transport is a mechanism that very little is known about and is generally not included within particle trajectory models. The work presented in this thesis could be a step toward improving the operational marine debris forecasts, especially around how marine debris is forced toward beaches and can be stranded there, limiting transport offshore.

Sea ice in the Arctic is melting earlier in the season and refreezing later [*Squire*, 2018]. This opens up additional fetch for waves to develop and grow, leading to wave-driven transport becoming a more important mechanism in the future. Similarly, as sea ice melts, more ice may be in free drift and act as a quasi-Lagrangian drifter following the combination of winds, currents, and waves. High-resolution field observations combined with trajectory modeling are needed to understand better drift in the marginal ice zone and correctly implement it in models.

6.3 Open Questions

Mini buoys, like the microSWIFT, have become ubiquitous [*Cavaleri et al.*, 2024]. With electronics becoming cheaper, smaller, and easier to implement than ever, many groups have developed different versions of drifters with suites of sensors. There is still no singular best method for measuring waves, and it is still an open question to find the exact error of these algorithms. Another open question is to develop a physics-informed sensor fusion algorithm for wave measurements from a buoy. Many buoys measure their global position, horizontal velocities, accelerations, rotation rates, and magnetic heading. Still, they do not measure vertical motion directly, which is needed for a wave measurement. With all of this data, an accurate way to reconstruct the sea surface elevation should exist, particularly if this could be done so that low-frequency waves, including infragravity waves, could be observed.

The surfing transport work presented in Chapters 3 and 4 is not a complete picture of surfing transport and is only a first look at field observations in the nearshore. The most crucial follow-up question to this work is understanding the surfing characteristics of other objects. We speculate that an object's specific gravity and volume will be the dominant traits that affect surfing, but this has not been tested. Secondly, it will be essential to understand the wave conditions that affect surfing. Do larger waves lead to larger surfing jumps, or does the size of the wave not particularly matter compared to when the object interacts with the breaking wave? It is suspected that if an object interacts with a breaking wave early on, it may likely be plunged under and therefore not surf, while interacting with a fully developed bore could lead to larger surfing events.

Another significant unknown from this work is why objects stop surfing. Is this because the wave they are on stops breaking, they bounce out of the bore from random turbulent motions, or some other phenomenon, and can this be estimated? What conditions are required for an object on the beach to reach the open ocean? An example of an application of surfing transport includes developing a bathymetry inversion function. The jump speeds are a function of the depth, and therefore, with enough surfing events, an estimate of the bathymetry could be reconstructed from these measurements. This could be particularly relevant for constructing bathymetry maps of highly dynamic areas where jet skis or other bathymetry measurement tools are not well suited. Further improvements to the surfing trajectory models also include using a fully probabilistic model where a random walk is added to the model to simulate the random fluctuations in the ocean. Through adding this random noise, the outcome of the trajectory model would be probability maps rather than a specific end location. This is a significant change to add to the model if it were ever to be used operationally. Surfing transport may be an essential mechanism for limiting cross-shore transport, object beaching, and enhanced transport speeds, and there is still much to learn about it.

The work on marginal ice zone transport presented here helped to show the current importance of wind—and wave-driven transport in the marginal ice zone. Future work will need to explore the relative effects over longer periods and during different seasons. It is additionally vital to understand how radiation stress gradients are affected by varying ice concentrations, ice types, wave directional spread, and more complex ice edge geometry.

6.4 Final Thoughts

As our understanding of ocean transport improves, the small-scale processes, such as wave-driven transport mechanisms, become more important for understanding motion. This dissertation has addressed the central question: What is the importance of wave-driven mechanisms for driving the transport of buoyant objects? The results presented here show that wave-driven mechanisms are essential in regions where wave transformation is a dominating feature, such as the surf and marginal ice zones. Going forward, as we examine other smaller-scale areas, we may find other mechanisms that are crucial to specific regions. Investigating these mechanisms and the noise in the signal is likely to be how we can further improve our understanding of transport in the future.

BIBLIOGRAPHY

Ardhuin, F., M. Otero, S. Merrifield, A. Grouazel, and E. Terrill, Ice Breakup Controls Dissipation of Wind Waves Across Southern Ocean Sea Ice, *Geophysical Research Letters*, *47*(13), doi:10.1029/2020gl087699, publisher: American Geophysical Union (AGU), 2020.

Arias, P. A., et al., Technical Summary. In Climate Change 2021: The Physical Science Basis. Contribution of Working Group I to the Sixth Assessment Report of the Intergovernmental Panel on Climate Change, doi:10.1017/9781009157896.002., 2021.

Arthur, A., A life worth dying from, `https://www.agelesspossibilities.org/blog-1/a-life-worth-dying-from`, blog post, 2023.

Battjes, J. A., Surf-Zone Dynamics, *Annual Review of Fluid Mechanics*, *20*(1), 257–291, doi:10.1146/annurev.fl.20.010188.001353, _eprint: https://doi.org/10.1146/annurev.fl.20.010188.001353, 1988.

Benetazzo, A., Measurements of short water waves using stereo matched image sequences, *Coastal engineering*, *53*(12), 1013–1032, 2006.

Bertin, X., Storm surges and coastal flooding: status and challenges, *La Houille Blanche*, *102*(2), 64–70, doi:10.1051/lhb/2016020, 2016.

Birch, R., D. B. Fissel, K. Borg, V. Lee, and D. English, The capabilities of doppler current profilers for directional wave measurements in coastal and nearshore waters, in *Oceans' 04 MTS/IEEE Techno-Ocean'04 (IEEE Cat. No. 04CH37600)*, vol. 3, pp. 1418–1427, IEEE, 2004.

Boehm, A. B., N. S. Ismail, L. M. Sassoubre, and E. A. Andruszkiewicz, Oceans in Peril: Grand Challenges in Applied Water Quality Research for the 21st Century, *Environmen-*

tal Engineering Science, *34*(1), 3–15, doi:10.1089/ees.2015.0252, publisher: Mary Ann Liebert, Inc., publishers, 2017.

Booij, N., L. H. Holthuijsen, and R. C. Ris, THE "SWAN" WAVE MODEL FOR SHALLOW WATER, *Coastal Engineering Proceedings*, (25), doi:10.9753/icce.v25, number: 25, 1996.

Bowen, A. J., The Generation of Longshore Currents on a Plane Beach, 1969.

Breivik, O., and A. A. Allen, An operational search and rescue model for the Norwegian Sea and the North Sea, *Journal of Marine Systems*, *69*(1-2), 99–113, doi:10.1016/j.jmarsys.2007.02.010, 2008.

Breivik, , A. A. Allen, C. Maisondieu, and J. C. Roth, Wind-induced drift of objects at sea: The leeway field method, *Applied Ocean Research*, *33*(2), 100–109, doi:10.1016/j.apor.2011.01.005, 2011.

Breivik, , A. A. Allen, C. Maisondieu, and M. Olagnon, Advances in Search and Rescue at Sea, *Ocean Dynamics*, *63*(1), 83–88, doi:10.1007/s10236-012-0581-1, arXiv:1211.0805 [physics], 2013.

Brenner, S., L. Rainville, J. Thomson, S. Cole, and C. Lee, Comparing Observations and Parameterizations of Ice-Ocean Drag Through an Annual Cycle Across the Beaufort Sea, *Journal of Geophysical Research: Oceans*, *126*(4), e2020JC016,977, doi:10.1029/2020JC016977, 2021.

Brown, A., J. Thomson, A. Ellenson, F. T. Rollano, H. T. Özkan Haller, and M. C. Haller, Kinematics and Statistics of Breaking Waves Observed Using SWIFT Buoys, *IEEE Journal of Oceanic Engineering*, *44*(4), 1011–1023, doi:10.1109/JOE.2018.2868335, conference Name: IEEE Journal of Oceanic Engineering, 2019.

Calvert, R., M. L. McAllister, C. Whittaker, A. Raby, A. G. L. Borthwick, and T. S. v. d. Bremer, The increased wave-induced drift of floating marine litter: A mechanism for the increased wave-induced drift of floating marine litter, arXiv:2102.09836 [physics], 2021.

Carini, R. J., C. C. Chickadel, A. T. Jessup, and J. Thomson, Estimating wave energy dissipation in the surf zone using thermal infrared imagery, *Journal of Geophysical Research: Oceans*, *120*(6), 3937–3957, 2015.

Cavaleri, L., et al., More room at the top: how small buoys aim at the detailed dynamics of the air-sea interface, *arXiv preprint arXiv:2410.07813*, 2024.

Chardón-Maldonado, P., J. C. Pintado-Patiño, and J. A. Puleo, Advances in swash-zone research: Small-scale hydrodynamic and sediment transport processes, *Coastal Engineering*, *115*, 8–25, doi:10.1016/j.coastaleng.2015.10.008, 2016.

Christensen, K., O. Breivik, K.-F. Dagestad, J. Röhrs, and B. Ward, Short-Term Predictions of Oceanic Drift, *Oceanography*, *31*(3), 59–67, doi:10.5670/oceanog.2018.310, 2018.

Christou, M., D. Rijnsdorp, and K. Ewans, Analysis of shallow water wave measurements recorded at the field research facility, in *Proceedings of 12t h International Workshop on Wave Hindcasting & Forecasting & 3rd Coastal Hazard s Symposium, 12pp*, 2011.

Cialone, M., et al., A large-scale community storm processes field experiment : the During Nearshore Event Experiment (DUNEX) overview reference report, *Tech. rep.*, Engineer Research and Development Center (U.S.), doi:10.21079/11681/46548, 2023.

Corcoran, P. L., M. C. Biesinger, and M. Grifi, Plastics and beaches: A degrading relationship, *Marine Pollution Bulletin*, *58*(1), 80–84, doi:10.1016/j.marpolbul.2008.08.022, 2009.

Critchell, K., A. Grech, J. Schlaefer, F. Andutta, J. Lambrechts, E. Wolanski, and M. Hamann, Modelling the fate of marine debris along a complex shoreline: Lessons from the Great Barrier Reef, *Estuarine, Coastal and Shelf Science*, *167*, 414–426, doi:10.1016/j.ecss.2015.10.018, 2015.

Dagestad, K.-F., J. Röhrs, Breivik, and B. Ådlandsvik, OpenDrift v1.0: a generic framework for trajectory modelling, *Geoscientific Model Development*, *11*(4), 1405–1420, doi:10.5194/gmd-11-1405-2018, 2018.

Davidson, B., J. Brenner, and N. Pujara, Beaching model for buoyant marine debris in bore-driven swash, *Flow*, *3*, E35, 2023.

Dean, R. G., and R. A. Dalrymple, *Water wave mechanics for engineers and scientists*, vol. 2, world scientific publishing company, 1991.

Deike, L., N. Pizzo, and W. K. Melville, Lagrangian transport by breaking surface waves, *Journal of Fluid Mechanics*, *829*, 364–391, 2017a.

Deike, L., N. Pizzo, and W. K. Melville, Lagrangian transport by breaking surface waves, *Journal of Fluid Mechanics*, *829*, 364–391, doi:10.1017/jfm.2017.548, 2017b.

Derakhti, M., J. T. Kirby, F. Shi, and G. Ma, Wave breaking in the surf zone and deep-water in a non-hydrostatic RANS model. Part 2: Turbulence and mean circulation, *Ocean Modelling*, *107*, 139–150, doi:10.1016/j.ocemod.2016.09.011, 2016.

Derakhti, M., J. T. Kirby, M. L. Banner, S. T. Grilli, and J. Thomson, A Unified Breaking Onset Criterion for Surface Gravity Water Waves in Arbitrary Depth, *Journal of Geophysical Research: Oceans*, *125*(7), e2019JC015,886, doi:10.1029/2019JC015886, _eprint: https://onlinelibrary.wiley.com/doi/pdf/10.1029/2019JC015886, 2020.

DiBenedetto, M. H., L. K. Clark, and N. Pujara, Enhanced settling and dispersion of inertial particles in surface waves, *Journal of Fluid Mechanics*, *936*, A38, doi:10.1017/jfm.2022.95, 2022.

Drushka, K., et al., Salinity and Stratification at the Sea Ice Edge (SASSIE): An oceanographic field campaign in the Beaufort Sea, doi:10.5194/essd-2023-406, 2024.

Dumont, D., Marginal ice zone dynamics: history, definitions and research perspectives, *Philosophical Transactions of the Royal Society A: Mathematical, Physical and Engineering Sciences*, *380*(2235), 20210,253, doi:10.1098/rsta.2021.0253, 2022.

Earle, M. D., K. Steele, and D. W. Wang, Use of advanced directional wave spectra analysis methods, *Ocean Engineering*, *26*, 1421–1434, 1999.

Eeltink, D., R. Calvert, J. Swagemakers, Q. Xiao, and T. Van Den Bremer, Stochastic particle transport by deep-water irregular breaking waves, *Journal of Fluid Mechanics*, *971*, A38, doi:10.1017/jfm.2023.671, 2023.

Elgar, S., R. T. Guza, B. Raubenheimer, T. H. C. Herbers, and E. L. Gallagher, Spectral evolution of shoaling and breaking waves on a barred beach, *Journal of Geophysical Research: Oceans*, *102*(C7), 15,797–15,805, doi:10.1029/97JC01010, _eprint: https://onlinelibrary.wiley.com/doi/pdf/10.1029/97JC01010, 1997.

Elgar, S., R. Guza, W. O'Reilly, B. Raubenheimer, and T. Herbers, Wave energy and direction observed near a pier, *Journal of waterway, port, coastal, and ocean engineering*, *127*(1), 2–6, 2001.

Feddersen, F., R. T. Guza, S. Elgar, and T. H. C. Herbers, Alongshore momentum balances in the nearshore, *Journal of Geophysical Research: Oceans*, *103*(C8), 15,667–15,676, doi:10.1029/98JC01270, _eprint: https://onlinelibrary.wiley.com/doi/pdf/10.1029/98JC01270, 1998.

Feddersen, F., A. Amador, K. Pick, A. Vizuet, K. Quinn, E. Wolfinger, J. MacMahan, and A. Fincham, The wavedrifter: a low-cost imu-based lagrangian drifter to observe steepening and overturning of surface gravity waves and the transition to turbulence, *Coastal Engineering Journal*, pp. 1–14, 2023.

Forristall, G. Z., Wave crest distributions: Observations and second-order theory, *Journal of physical oceanography*, *30*(8), 1931–1943, 2000.

Gallagher, E. L., S. Elgar, and R. T. Guza, Observations of sand bar evolution on a natural beach, *Journal of Geophysical Research: Oceans*, *103*(C2), 3203–3215, doi:10.1029/97JC02765, _eprint: https://onlinelibrary.wiley.com/doi/pdf/10.1029/97JC02765, 1998.

Gill, A. E., *Atmosphere—ocean dynamics*, Elsevier, 2016.

Gomes, E. R., R. P. Mulligan, K. L. Brodie, and J. E. McNinch, Bathymetric control on the spatial distribution of wave breaking in the surf zone of a natural beach, *Coastal Engineering*, *116*, 180–194, doi:10.1016/j.coastaleng.2016.06.012, 2016.

Guérin, T., X. Bertin, T. Coulombier, and A. de Bakker, Impacts of wave-induced circulation in the surf zone on wave setup, *Ocean Modelling*, *123*, 86–97, 2018.

Hasselmann, K., et al., Measurements of wind-wave growth and swell decay during the joint north sea wave project (jonswap)., *Ergaenzungsheft zur Deutschen Hydrographischen Zeitschrift, Reihe A*, 1973.

Herbers, T. H. C., P. F. Jessen, T. T. Janssen, D. B. Colbert, and J. H. MacMahan, Observing Ocean Surface Waves with GPS-Tracked Buoys, *Journal of Atmospheric and Oceanic Technology*, *29*(7), 944–959, doi:10.1175/JTECH-D-11-00128.1, publisher: American Meteorological Society Section: Journal of Atmospheric and Oceanic Technology, 2012.

Herman, A., Wave-induced surge motion and collisions of sea ice floes: Finite-floe-size effects, *Journal of Geophysical Research: Oceans*, *123*(10), 7472–7494, 2018.

Hine, R., S. Willcox, G. Hine, and T. Richardson, The wave glider: A wave-powered autonomous marine vehicle, in *OCEANS 2009*, pp. 1–6, IEEE, 2009.

Ho, J., The implications of arctic sea ice decline on shipping, *Marine Policy*, *34*(3), 713–715, 2010.

Houghton, I. A., P. B. Smit, D. Clark, C. Dunning, A. Fisher, N. J. Nidzieko, P. Chamberlain, and T. T. Janssen, Performance Statistics of a Real-Time Pacific Ocean Weather Sensor

Network, *Journal of Atmospheric and Oceanic Technology*, *38*(5), 1047–1058, doi:10.1175/JTECH-D-20-0187.1, 2021.

Houston, J. R., The economic value of America's beaches, *Shore & Beach*, pp. 33–43, doi:10.34237/1009225, 2024.

Intergovernmental Panel on Climate Change, *Climate Change 2021 - The Physical Science Basis - Summary for Policymakers*, 31 pp., 2021.

Iyer, S., J. Thomson, E. Thompson, and K. Drushka, Variations in Wave Slope and Momentum Flux From Wave-Current Interactions in the Tropical Trade Winds, *Journal of Geophysical Research: Oceans*, *127*(3), e2021JC018,003, doi:10.1029/2021JC018003, 2022.

Jackson, J. M., W. J. Williams, and E. C. Carmack, Winter sea-ice melt in the Canada Basin, Arctic Ocean, *Geophysical Research Letters*, *39*(3), doi:10.1029/2011gl050219, publisher: American Geophysical Union (AGU), 2012.

Johnson, D., and C. Pattiaratchi, Application, modelling and validation of surfzone drifters, *Coastal Engineering*, *51*(5-6), 455–471, doi:10.1016/j.coastaleng.2004.05.005, 2004.

Karim, S. A. A., M. A. M. Rosli, and M. I. M. Mustafa, Cubic spline interpolation for petroleum engineering data, *Applied Mathematical Sciences*, *8*, 5083–5098, doi:10.12988/ams.2014.44284, 2014.

Kastner, S. E., A. R. Horner-Devine, and J. M. Thomson, A Conceptual Model of a River Plume in the Surf Zone, *Journal of Geophysical Research: Oceans*, *124*(11), 8060–8078, doi:10.1029/2019JC015510, 2019.

Kirby, J. T., G. Wei, Q. Chen, A. B. Kennedy, and R. A. Dalrymple, Funwave 1.0: Fully Nonlinear Boussinesq Wave Model - Documentation and User's Manual, *research report NO. CACR-98-06*, publisher: University of Delaware, 1998.

Kohout, A. L., M. J. M. Williams, S. M. Dean, and M. H. Meylan, Storm-induced sea-ice breakup and the implications for ice extent, *Nature*, *509*(7502), 604–607, doi:10.1038/nature13262, publisher: Springer Science and Business Media LLC, 2014.

Kuik, A. J., G. P. v. Vledder, and L. H. Holthuijsen, A Method for the Routine Analysis of Pitch-and-Roll Buoy Wave Data, *Journal of Physical Oceanography*, *18*(7), 1020–1034, doi:10.1175/1520-0485(1988)018⟨1020:AMFTRA⟩2.0.CO;2, publisher: American Meteorological Society Section: Journal of Physical Oceanography, 1988.

Kumar, N., D. L. Cahl, S. C. Crosby, and G. Voulgaris, Bulk versus spectral wave parameters: Implications on stokes drift estimates, regional wave modeling, and hf radars applications, *Journal of Physical Oceanography*, *47*(6), 1413–1431, 2017.

Lavaud, L., X. Bertin, K. Martins, M. Pezerat, T. Coulombier, and D. Dausse, Wave dissipation and mean circulation on a shore platform under storm wave conditions, *Journal of Geophysical Research: Earth Surface*, *127*(3), e2021JF006,466, 2022.

Laxague, N. J. M., et al., Observations of Near-Surface Current Shear Help Describe Oceanic Oil and Plastic Transport, *Geophysical Research Letters*, *45*(1), 245–249, doi:10.1002/2017GL075891, 2018.

Lenain, L., N. Pizzo, and W. K. Melville, Laboratory studies of Lagrangian transport by breaking surface waves, *Journal of Fluid Mechanics*, *876*, R1, doi:10.1017/jfm.2019.544, 2019.

Lentz, S. J., and M. R. Fewings, The Wind- and Wave-Driven Inner-Shelf Circulation, *Annual Review of Marine Science*, *4*(1), 317–343, doi:10.1146/annurev-marine-120709-142745, 2012.

Longuet-Higgins, M. S., and R. W. STEWARTt, Radiation stresses in ˜vater waves; a physical discussion, with applications, 1964.

Lund, B., H. C. Graber, P. O. G. Persson, M. Smith, M. Doble, J. Thomson, and P. Wadhams, Arctic Sea Ice Drift Measured by Shipboard Marine Radar, *Journal of Geophysical Research: Oceans*, *123*(6), 4298–4321, doi:10.1029/2018JC013769, 2018.

Ma, B., M. Steele, and C. M. Lee, Ekman circulation in the A rctic O cean: Beyond the B eaufort G yre, *Journal of Geophysical Research: Oceans*, *122*(4), 3358–3374, doi:10.1002/2016JC012624, 2017.

Ma, G., F. Shi, and J. T. Kirby, Shock-capturing non-hydrostatic model for fully dispersive surface wave processes, *Ocean Modelling*, *43-44*, 22–35, doi:10.1016/j.ocemod.2011.12.002, 2012.

MacKinnon, J. A., et al., A warm jet in a cold ocean, *Nature Communications*, *12*(1), 2418, doi:10.1038/s41467-021-22505-5, 2021.

Maclean, K., E. A. Weideman, V. Perold, and P. G. Ryan, Buoyancy affects stranding rate and dispersal distance of floating litter entering the sea from river mouths, *Marine Pollution Bulletin*, *173*, 113,028, doi:10.1016/j.marpolbul.2021.113028, 2021.

Magnusson, A., M. Donelan, and W. Drennan, On estimating extremes in an evolving wave field, *Coastal Engineering*, *36*(2), 147–163, 1999.

Manucharyan, G. E., and A. F. Thompson, Submesoscale Sea Ice-Ocean Interactions in Marginal Ice Zones, *Journal of Geophysical Research: Oceans*, *122*(12), 9455–9475, doi:10.1002/2017JC012895, 2017.

Martínez, M. L., A. Intralawan, G. Vázquez, O. Pérez-Maqueo, P. Sutton, and R. Landgrave, The coasts of our world: Ecological, economic and social importance, *Ecological Economics*, *63*(2), 254–272, doi:10.1016/j.ecolecon.2006.10.022, 2007.

Masson, D., and P. LeBlond, Spectral evolution of wind-generated surface gravity waves in a dispersed ice field, *Journal of Fluid Mechanics*, *202*, 43–81, 1989.

Meier, W., and J. Stroeve, An Updated Assessment of the Changing Arctic Sea Ice Cover, *Oceanography*, doi:10.5670/oceanog.2022.114, publisher: The Oceanography Society, 2022.

Moulton, M., S. Elgar, B. Raubenheimer, J. C. Warner, and N. Kumar, Rip currents and alongshore flows in single channels dredged in the surf zone, *Journal of Geophysical Research: Oceans*, *122*(5), 3799–3816, doi:10.1002/2016JC012222, _eprint: https://agupubs.onlinelibrary.wiley.com/doi/pdf/10.1002/2016JC012222, 2017.

Moulton, M., S. H. Suanda, J. C. Garwood, N. Kumar, M. R. Fewings, and J. M. Pringle, Exchange of plankton, pollutants, and particles across the nearshore region, *Annual Review of Marine Science*, *15*, 167–202, 2023a.

Moulton, M., S. H. Suanda, J. C. Garwood, N. Kumar, M. R. Fewings, and J. M. Pringle, Exchange of Plankton, Pollutants, and Particles Across the Nearshore Region, *Annual Review of Marine Science*, *15*(1), 167–202, doi:10.1146/annurev-marine-032122-115057, 2023b.

Murphy, E., I. Nistor, A. Cornett, J. Wilson, and A. Pilechi, Fate and transport of coastal driftwood: A critical review, *Marine Pollution Bulletin*, *170*, 112,649, 2021.

Neumann, J. E., K. Emanuel, S. Ravela, L. Ludwig, P. Kirshen, K. Bosma, and J. Martinich, Joint effects of storm surge and sea-level rise on US Coasts: new economic estimates of impacts, adaptation, and benefits of mitigation policy, *Climatic Change*, *129*(1-2), 337–349, doi:10.1007/s10584-014-1304-z, 2015.

NOAA, N. O. a. A. A. M. D. P., 2016 Report on Modeling Oceanic Transport of Floating Marine Debris, p. 21, 2016.

Nuttall, A., and G. Carter, A generalized framework for power spectral estimation, *IEEE Transactions on Acoustics, Speech, and Signal Processing*, *28*(3), 334–335, 1980.

Olguin-Maciel, E., R. M. Leal-Bautista, L. Alzate-Gaviria, J. Domínguez-Maldonado, and R. Tapia-Tussell, Environmental impact of Sargassum spp. landings: an evaluation of leachate released from natural decomposition at Mexican Caribbean coast, *Environmental Science and Pollution Research*, *29*(60), 91,071–91,080, doi:10.1007/s11356-022-22123-8, 2022.

Overland, J. E., H. O. Mofjeld, and C. H. Pease, Wind-driven ice drift in a shallow sea, *Journal of Geophysical Research: Oceans*, *89*(C4), 6525–6531, doi:10.1029/JC089iC04p06525, 1984.

Pacini, A., M. Steele, and M.-B. Schreck, National Weather Service Alaska Sea Ice Program: gridded ice concentration maps for the Alaskan Arctic, *The Cryosphere*, *19*(3), 1391–1411, doi:10.5194/tc-19-1391-2025, 2025.

Pedersen, T., E. Siegel, and J. Wood, Directional Wave Measurements from a Subsurface Buoy with an Acoustic Wave and Current Profiler (AWAC), in *OCEANS 2007*, pp. 1–10, doi:10.1109/OCEANS.2007.4449153, iSSN: 0197-7385, 2007.

Perrie, W., and Y. Hu, Air–Ice–Ocean Momentum Exchange. Part II: Ice Drift, *Journal of Physical Oceanography*, *27*(9), 1976–1996, doi:10.1175/1520-0485(1997)027⟨1976:AIOMEP⟩2.0.CO;2, 1997.

Pezerat, M., X. Bertin, K. Martins, and L. Lavaud, Cross-shore distribution of the wave-induced circulation over a dissipative beach under storm wave conditions, *Journal of Geophysical Research: Oceans*, *127*(3), e2021JC018,108, 2022.

Pizzo, N., Surfing surface gravity waves, *Journal of Fluid Mechanics*, *823*, 316–328, doi:10.1017/jfm.2017.314, 2017a.

Pizzo, N., W. K. Melville, and L. Deike, Lagrangian Transport by Nonbreaking and Breaking Deep-Water Waves at the Ocean Surface, *Journal of Physical Oceanography*, *49*(4), 983–992, doi:10.1175/JPO-D-18-0227.1, 2019.

Pizzo, N. E., Surfing surface gravity waves, *Journal of Fluid Mechanics*, *823*, 316–328, 2017b.

Post, E., et al., Ecological consequences of sea-ice decline, *science*, *341*(6145), 519–524, 2013.

Raghukumar, K., G. Chang, F. Spada, C. Jones, T. Janssen, and A. Gans, Performance Characteristics of “Spotter,” a Newly Developed Real-Time Wave Measurement Buoy, *Journal of Atmospheric and Oceanic Technology*, *36*(6), 1127–1141, doi: 10.1175/JTECH-D-18-0151.1, publisher: American Meteorological Society Section: Journal of Atmospheric and Oceanic Technology, 2019.

Rainville, J. Thomson, M. Moulton, and M. Derakhti, Measurements of nearshore ocean-surface kinematics through coherent arrays of free-drifting buoys, *Earth System Science Data*, *15*(11), 5135–5151, doi:10.5194/essd-15-5135-2023, 2023a.

Rainville, E. J., Measurements of nearshore waves through coherent arrays of small-scale, free-drifting wave buoys, Master’s thesis, University of Washington, 2022.

Rainville, E. J., Surfing transport analysis github repository, doi:10.5281/zenodo.14736659, 2025.

Rainville, E. J., J. Thomson, M. Moulton, and M. Derakhti, Measurements of nearshore waves through coherent arrays of free-drifting wave buoys (uw_drifters), doi:doi:10.5061/dryad.hx3ffbgk0, 2023b.

Rainville, E. J., J. Thomson, M. Moulton, and M. Derakhti, Surfing transport of buoyant objects observed in the nearshore, *Authorea Preprints*, 2025.

Raubenheimer, B., R. Guza, and S. Elgar, Wave transformation across the inner surf zone, *Journal of Geophysical Research: Oceans*, *101*(C11), 25,589–25,597, 1996a.

Raubenheimer, B., R. T. Guza, and S. Elgar, Wave transformation across the inner surf zone, *Journal of Geophysical Research: Oceans*, *101*(C11), 25,589–25,597, doi:10.1029/96JC02433, _eprint: https://onlinelibrary.wiley.com/doi/pdf/10.1029/96JC02433, 1996b.

Ruessink, B. G., J. R. Miles, F. Feddersen, R. T. Guza, and S. Elgar, Modeling the alongshore current on barred beaches, *Journal of Geophysical Research: Oceans*, *106*(C10), 22,451–22,463, doi:10.1029/2000JC000766, 2001.

Sallenger Jr, A. H., and R. A. Holman, Wave energy saturation on a natural beach of variable slope, *Journal of Geophysical Research: Oceans*, *90*(C6), 11,939–11,944, 1985.

Schäffer, H. A., P. A. Madsen, and R. Deigaard, A boussinesq model for waves breaking in shallow water, *Coastal engineering*, *20*(3-4), 185–202, 1993.

Schiller, A., B. Mourre, Y. Drillet, and G. Brassington, An Overview of Operational Oceanography, in *New Frontiers in Operational Oceanography*, edited by E. P. Chassignet, A. Pascual, J. Tintoré, and J. Verron, GODAE OceanView, doi:10.17125/gov2018.ch01, 2018.

Schmidt, W. E., B. T. Woodward, K. S. Millikan, R. T. Guza, B. Raubenheimer, and S. Elgar, A GPS-Tracked Surf Zone Drifter, *Journal of Atmospheric and Oceanic Technology*, *20*(7), 1069–1075, doi:10.1175/1460.1, publisher: American Meteorological Society Section: Journal of Atmospheric and Oceanic Technology, 2003.

Schmidt, W. E., R. T. Guza, and D. N. Slinn, Surf zone currents over irregular bathymetry: Drifter observations and numerical simulations, *Journal of Geophysical Research*, *110*(C12), C12,015, doi:10.1029/2004JC002421, 2005.

Shi, F., J. T. Kirby, J. C. Harris, J. D. Geiman, and S. T. Grilli, A high-order adaptive time-stepping tvd solver for boussinesq modeling of breaking waves and coastal inundation, *Ocean Modelling*, *43*, 36–51, 2012.

Sinclair, A., Flowrider: A lagrangian float to measure 3-d dynamics of plunging breakers in the surf zone, *Journal of Coastal Research*, *30*(1), 205–209, 2014.

Smetacek, V., and A. Zingone, Green and golden seaweed tides on the rise, *Nature*, *504*(7478), 84–88, 2013.

Spydell, M., F. Feddersen, R. T. Guza, and W. E. Schmidt, Observing Surf-Zone Dispersion with Drifters, *Journal of Physical Oceanography*, *37*(12), 2920–2939, doi:10.1175/2007JPO3580.1, 2007.

Squire, V. A., A fresh look at how ocean waves and sea ice interact, *Philosophical Transactions of the Royal Society A: Mathematical, Physical and Engineering Sciences*, *376*(2129), 20170,342, 2018.

Squire, V. A., J. P. Dugan, P. Wadhams, P. J. Rottier, and A. K. Liu, Of ocean waves and sea ice, *Annual Review of Fluid Mechanics*, *27*(1), 115–168, 1995.

Steele, M., J. H. Morison, and N. Untersteiner, The partition of air-ice-ocean momentum exchange as a function of ice concentration, floe size, and draft, *Journal of Geophysical Research: Oceans*, *94*(C9), 12,739–12,750, doi:10.1029/JC094iC09p12739, 1989.

Stokes, G. G., On the theory of oscillatory waves, *Trans. Cam. Philos. Soc.*, *8*, 441–455, 1847.

Stroeve, J., and D. Notz, Changing state of arctic sea ice across all seasons, *Environmental Research Letters*, *13*(10), 103,001, 2018.

Sutherland, B. R., M. DiBenedetto, A. Kaminski, and T. Van Den Bremer, Fluid dynamics challenges in predicting plastic pollution transport in the ocean: A perspective, *Physical Review Fluids*, *8*(7), 070,701, doi:10.1103/PhysRevFluids.8.070701, 2023.

Sutherland, P., and D. Dumont, Marginal Ice Zone Thickness and Extent due to Wave Radiation Stress, *Journal of Physical Oceanography*, *48*(8), 1885–1901, doi:10.1175/JPO-D-17-0167.1, 2018.

Svendsen, I. A., *Introduction To Nearshore Hydrodynamics*, World Scientific Publishing Company, 2005.

Thomson, J., Wave breaking dissipation observed with “swift” drifters, *Journal of Atmospheric and Oceanic Technology*, *29*(12), 1866–1882, 2012a.

Thomson, J., Wave Breaking Dissipation Observed with “SWIFT” Drifters, *Journal of Atmospheric and Oceanic Technology*, *29*(12), 1866–1882, doi:10.1175/JTECH-D-12-00018.1, publisher: American Meteorological Society Section: Journal of Atmospheric and Oceanic Technology, 2012b.

Thomson, J., Wave propagation in the marginal ice zone: connections and feedback mechanisms within the air–ice–ocean system, *Philosophical Transactions of the Royal Society A: Mathematical, Physical and Engineering Sciences*, *380*(2235), 20210,251, doi:10.1098/rsta.2021.0251, 2022.

Thomson, J., and W. E. Rogers, Swell and sea in the emerging arctic ocean, *Geophysical Research Letters*, *41*(9), 3136–3140, 2014.

Thomson, J., M. S. Schwendeman, S. F. Zippel, S. Moghimi, J. Gemmrich, and W. E. Rogers, Wave-Breaking Turbulence in the Ocean Surface Layer, *Journal of Physical Oceanography*, *46*(6), 1857–1870, doi:10.1175/JPO-D-15-0130.1, publisher: American Meteorological Society Section: Journal of Physical Oceanography, 2016.

Thomson, J., J. B. Girton, R. Jha, and A. Trapani, Measurements of Directional Wave Spectra and Wind Stress from a Wave Glider Autonomous Surface Vehicle, *Journal of Atmospheric and Oceanic Technology*, *35*(2), 347–363, doi:10.1175/JTECH-D-17-0091.1, 2018.

Thomson, J., B. Lund, J. Hargrove, M. M. Smith, J. Horstmann, and J. A. MacKinnon, Wave-Driven Flow Along a Compact Marginal Ice Zone, *Geophysical Research Letters*, *48*(3), e2020GL090,735, doi:10.1029/2020GL090735, 2021.

Thomson, J., et al., Development and testing of microSWIFT expendable wave buoys, *Coastal Engineering Journal*, pp. 1–13, doi:10.1080/21664250.2023.2283325, 2023.

Thomson, J., et al., Development and testing of microswift expendable wave buoys, *Coastal Engineering Journal*, *66*(1), 168–180, 2024.

Thomson, R. E., and W. J. Emery, *Data analysis methods in physical oceanography*, Newnes, 2014.

Thornton, E. B., and R. Guza, Surf zone longshore currents and random waves: Field data and models, *Journal of Physical Oceanography*, *16*(7), 1165–1178, 1986.

Thornton, E. B., and R. T. Guza, Transformation of wave height distribution, *Journal of Geophysical Research*, *88*(C10), 5925, doi:10.1029/JC088iC10p05925, 1983.

Timmermans, M.-L., and J. M. Toole, The Arctic Ocean's Beaufort Gyre, *Annual Review of Marine Science*, *15*(1), 223–248, doi:10.1146/annurev-marine-032122-012034, 2023.

Tissier, M., P. Bonneton, R. Almar, B. Castelle, N. Bonneton, and A. Nahon, Field measurements and non-linear prediction of wave celerity in the surf zone, *European Journal of Mechanics-B/Fluids*, *30*(6), 635–641, 2011.

Tolman, H. L., User manual and system documentation of WAVEWATCH III TM version 3.14, 1999.

Toole, J. M., M. Timmermans, D. K. Perovich, R. A. Krishfield, A. Proshutinsky, and J. A. Richter-Menge, Influences of the ocean surface mixed layer and thermohaline stratification on Arctic Sea ice in the central Canada Basin, *Journal of Geophysical Research: Oceans*, *115*(C10), doi:10.1029/2009jc005660, publisher: American Geophysical Union (AGU), 2010.

Van Den Bremer, T. S., and Breivik, Stokes drift, *Philosophical Transactions of the Royal Society A: Mathematical, Physical and Engineering Sciences*, *376*(2111), 20170,104, doi:10.1098/rsta.2017.0104, 2018.

Van Sebille, E., et al., The physical oceanography of the transport of floating marine debris, *Environmental Research Letters*, *15*(2), 023,003, doi:10.1088/1748-9326/ab6d7d, 2020.

Van Tussenbroek, B. I., H. A. H. Arana, R. E. Rodríguez-Martínez, J. Espinoza-Avalos, H. M. Canizales-Flores, C. E. González-Godoy, M. G. Barba-Santos, A. Vega-Zepeda, and L. Collado-Vides, Severe impacts of brown tides caused by sargassum spp. on near-shore caribbean seagrass communities, *Marine pollution bulletin*, *122*(1-2), 272–281, 2017.

Voermans, J. J., A. V. Babanin, J. Thomson, M. M. Smith, and H. H. Shen, Wave Attenuation by Sea Ice Turbulence, *Geophysical Research Letters*, *46*(12), 6796–6803, doi:10.1029/2019GL082945, 2019.

Wadhams, P., V. A. Squire, D. J. Goodman, A. M. Cowan, and S. C. Moore, The attenuation rates of ocean waves in the marginal ice zone, *Journal of Geophysical Research: Oceans*, *93*(C6), 6799–6818, doi:10.1029/JC093iC06p06799, 1988.

Wagner, T. J. W., I. Eisenman, A. M. Ceroli, and N. C. Constantinou, How Winds and Ocean Currents Influence the Drift of Floating Objects, *Journal of Physical Oceanography*, *52*(5), 907–916, doi:10.1175/JPO-D-20-0275.1, 2022.

Warner, J. C., B. Armstrong, R. He, and J. B. Zambon, Development of a coupled ocean–atmosphere–wave–sediment transport (coawst) modeling system, *Ocean modelling*, *35*(3), 230–244, 2010.

Webster, R. K., and T. Linton, Development and implementation of sargassum early advisory system (seas), *Shore & Beach*, *81*(3), 1, 2013.

Zippel, S., and J. Thomson, Surface wave breaking over sheared currents: Observations from the Mouth of the Columbia River, *Journal of Geophysical Research: Oceans*, *122*(4), 3311–3328, doi:10.1002/2016JC012498, _eprint: https://agupubs.onlinelibrary.wiley.com/doi/pdf/10.1002/2016JC012498, 2017.